

**DROPLET GENERATORS FOR ENCAPSULATION OF NEONATAL PORCINE
ISLETS IN ALGINATE**

by

René G. Pedroza

B.Sc., Tec de Monterrey, 2008

A THESIS SUBMITTED IN PARTIAL FULFILLMENT OF
THE REQUIREMENTS FOR THE DEGREE OF

MASTER OF SCIENCE

in

THE FACULTY OF GRADUATE AND POSTDOCTORAL STUDIES
(Pharmaceutical Sciences)

THE UNIVERSITY OF BRITISH COLUMBIA

(Vancouver)

April 2015

© René G. Pedroza, 2015

Abstract

For the treatment of type 1 diabetes, islet transplantation has the potential to control blood glucose levels more effectively than daily insulin injections. However, its widespread application is hindered by the limited supply of transplantable human islets and the side effects of life-long immunosuppression. Microencapsulation of islets in alginate can contribute to overcoming these barriers by facilitating the use of alternative sources of islets, such as neonatal porcine islets (NPI), and by reducing the need for immunosuppressive therapy. This work describes a process for immobilization of NPI in 5% alginate capsules by an emulsification and internal gelation approach utilizing droplet generators fabricated via soft lithography or stereolithography. Alginate capsules produced with microfluidic devices fabricated in PDMS had mean diameters between 300 and 600 μm . Capsules generated with 3D-printed droplet generators fabricated via stereolithography were capable of producing more than 30-times the number of capsules per minute than a microfluidic devices, but with approximately 2-fold greater mean bead diameters. These results suggest that 3D-printed droplet generators are better suited for encapsulating NPI for transplantation applications (*e.g.*, future *in vivo* studies). Furthermore, encapsulation in 3D-printed droplet generators did not alter cell viability after processing unlike the microfluidic devices where the viability decreased 20%. After encapsulation, three different imaging techniques were explored to aid in the quantification of partially encapsulated islets. Overall, the results of this study should be useful for the improvement of immunoisolation approaches employing alginate immobilization.

Preface

An excerpt of the results presented in Chapter 3 and Chapter 4 will be submitted for publication in a peer-reviewed journal. I was a major contributor along with Dr. James Piret and Dr. Urs Hafeli in deciding the general direction of all the projects. I contributed most of the experimental designs, except for Section 3.1, to which Jake Yeung contributed the cell encapsulation work as part of a rotation in his M.Sc. program. NPI handling and counts after arrival were performed by Dr. Blanche Lo (Piret Laboratory, UBC). The mask and master used for PDMS devices were fabricated by Dr. Linfen Yu (Dr. Karen Cheung Laboratory, UBC). CT scans were performed and reconstructed by John Schipilow (Centre for High-Throughput Phenogenomics, UBC).

Table of Contents

Abstract.....	ii
Preface.....	iii
Table of Contents	iv
List of Tables	ix
List of Figures.....	xi
List of Abbreviations	xiv
List of Symbols	xvi
Acknowledgements	xvii
Dedication	xviii
Chapter 1: Introduction	1
1.1 Islet transplantation.....	3
1.2 Neonatal porcine islets.....	5
1.3 Islet encapsulation.....	7
1.3.1 Microencapsulation in alginate.....	8
1.4 Fabrication of microfluidic droplet generators	10
1.5 Research goals	14
Chapter 2: Materials and methods.....	16
2.1 Pancreatic cells.....	16
2.1.1 Neonatal porcine islets.....	16
2.1.2 MIN6 cell line.....	16
2.2 Reagents.....	17

2.2.1	Cross-linker suspension	17
2.2.2	Mineral oil and acidified oil.....	17
2.2.3	Alginate.....	17
2.3	Microfluidic droplet generators	18
2.3.1	Design and fabrication	18
2.3.2	Operation.....	20
2.4	3D-printed droplet generators	21
2.4.1	Design	21
2.4.2	Fabrication	24
2.4.2.1	Assessment of needle alignment.....	26
2.4.3	Operation.....	27
2.4.3.1	Setup	27
2.4.3.2	Generation of alginate beads and capsules	28
2.5	Emulsification-internal gelation.....	29
2.6	Alginate bead size distribution analysis.....	30
2.7	Cell viability assay.....	31
Chapter 3: Performance of microfluidic and 3D-printed droplet generators.....		32
3.1	Microfluidic droplet generators	32
3.1.1	Analysis of dimensionless numbers.....	32
3.1.2	Particle size distribution.....	34
3.1.3	Cell viability during processing	37
3.2	3D-printed droplet generators	40
3.2.1	Assessment of needle alignment.....	40

3.2.1.1	Precision of needle alignment measurements	40
3.2.1.2	Alignment errors in 3D-printed droplet generators	41
3.2.1.3	Effects of alignment errors on device performance	44
3.2.2	Design geometry, outer flow rate and particle size distribution	48
3.2.2.1	Dimensionless numbers	53
3.2.3	Effects of surfactant addition on particle size distribution	57
3.2.4	NPI encapsulation using 3D-printed droplet generators	61
Chapter 4: Exploration of imaging methods for assessment of partial encapsulation.....		66
4.1	Rationale	66
4.1.1	X-ray computerized tomography	67
4.1.2	Optical projection tomography	68
4.1.3	Confocal microscopy	69
4.2	Materials and methods	71
4.2.1	Sample fixation	71
4.2.2	Imaging with OPT	71
4.2.3	Imaging with CT	73
4.2.4	Imaging with LSCM	73
4.3	Results and discussion	74
4.3.1	OPT scans	74
4.3.2	CT scans	78
4.3.3	LSCM micrographs	81
4.4	Conclusions	84
4.4.1	Summary	84

4.4.2 Recommendations and future work	85
Chapter 5: Conclusions	89
5.1 Summary	89
5.2 Recommendations and future work	93
Bibliography	95
Appendices.....	102
Appendix A - Supplementary methods.....	102
A.1 ImageJ script of macro for needle alignment image analysis	102
A.2 Excel VBA script of macro for needle alignment analysis.....	104
A.3 Script of ImageJ macro for particle size distribution image analysis	106
A.4 R script of statistical analysis for effects of outer flow rate and design geometry on alginate bead size and polydispersity.....	107
Appendix B - Supplementary figures	112
B.1 CT scans for needle alignment measurements	112
B.2 Histograms from particle size analysis in 3D printed devices	118
B.3 Scatterplots of needle alignment vs. polydispersity	122
B.4 Micrographs of NPI.....	124
B.5 Micrographs of alginate particles	125
B.6 Size distribution of alginate capsules generated through emulsification-internal gelation.....	128
B.7 Additional CT scans with magnetic particles as contrast agents.	129
Appendix C - Supplementary tables	130
C.1 Summary of results for orthogonal Friedman tests	130

C.2	Summary of ANOVA results for simple ranked transform data.....	132
C.3	Summary of ANOVA and post hoc results for ART data.....	133

List of Tables

Table 1.1. Classes of antidiabetic drugs.....	3
Table 1.2. Current state of alginate encapsulation using microfluidic droplet generators.	13
Table 2.1. Design characteristics of 3D printed devices.....	23
Table 3.1. Classification of tested devices based on needle alignment error.	45
Table 3.2. Alginate droplet size estimates for co-flowing stream geometry.	55
Table 3.3. Alginate droplet size estimates for flow-focusing geometry and experimental results.	56
Table 3.4. Recalculated alginate droplet size estimates for flow-focusing geometry.	57
Table 4.1. Iron oxide particle solutions used as contrast agents in CT scans.	73
Table 5.1. Summary of dimensions of droplet generators and their operating conditions.	90
Table C.1 Friedman ranked sum tests for $D[2,0]$	130
Table C.2. Friedman ranked sum tests for $D[4,3]$	130
Table C.3. Friedman ranked sum tests for $IQR_{2,0}$	130
Table C.4. Friedman ranked sum tests for $IQR_{4,3}$	131
Table C.5. Friedman ranked sum tests for frequency.	131
Table C.6. Analysis of deviance for rank transformed $D[2,0]$	132
Table C.7. Analysis of deviance for rank transformed $D[4,3]$	132
Table C.8. Analysis of deviance for rank transformed $IQR_{2,0}$	132
Table C.9. Analysis of deviance for rank transformed $IQR_{4,3}$	132
Table C.10. Analysis of deviance for rank transformed frequency.	132
Table C.11. Analysis of deviance for aligned rank transformed $D[2,0]$	133
Table C.12. Analysis of deviance for aligned rank transformed $D[4,3]$	133

Table C.13. Analysis of deviance for aligned rank transformed $IQR_{2,0}$.	133
Table C.14. Analysis of deviance for aligned rank transformed $IQR_{4,3}$.	133
Table C.15. Analysis of deviance for aligned rank transformed frequency.	133
Table C.16. Contrasts resulting from Tukey's honest significance difference test on ART D[4,3].	
.....	134
Table C.17. Contrasts resulting from Tukey's honest significance difference test on ART $IQR_{2,0}$.	
.....	134
Table C.18. Contrasts resulting from Tukey's honest significance difference test on ART D[2,0].	
.....	134

List of Figures

Figure 2.1. Channel layout of microfluidic devices.....	19
Figure 2.2. Schematic drawing of 3D printed devices.....	22
Figure 2.3. Placement of objects in the printing tray.....	24
Figure 2.4. Cleaning of 3D printed parts and assembly into devices.	26
Figure 3.1. Particle size distributions of alginate beads generated in microfluidic devices.	34
Figure 3.2. Micrograph of alginate beads generated with microfluidic devices.....	37
Figure 3.3. Effect of processing time on cell viability during microfluidic device operation.	38
Figure 3.4. Evaluating the precision of CT scans.	41
Figure 3.5. Concentricity error in 3D-printed droplet generators.	43
Figure 3.6. Correlation between alignment error and polydispersity.	46
Figure 3.7. Effects of outer flow rate and design geometry on select descriptive statistics of alginate particle size distributions.....	49
Figure 3.8. Lognormal plot of alginate bead size distributions of 3D-printed droplet generators.	58
Figure 3.9. Alginate bead size distributions with and without surfactant added to the oil phase. 59	
Figure 3.10. Comparing polydispersity of alginate beads generated with or without surfactants.60	
Figure 3.11. Size distributions of alginate capsules containing NPI.	62
Figure 3.12. Comparing $D[4,3]$ of empty alginate beads and alginate capsules containing NPI. 63	
Figure 3.13. NPI viability before and after encapsulation.	64
Figure 4.1. Schematic of imaging principles in tomographic techniques.....	69
Figure 4.2. Schematic of labeling protocol for detecting partially encapsulated NPI using laser scanning confocal microscopy.....	71

Figure 4.3. OPT scan of alginate capsules containing NPI.....	75
Figure 4.4. OPT scanning with alignment of center of mass and axis of rotation.....	77
Figure 4.5. CT scans using different contrast agents.....	80
Figure 4.6. CT imaging with 30 nm iron nanoparticle solution as contrast agent.....	81
Figure 4.7. Imaging of alginate capsules with confocal microscopy.....	83
Figure 5.1. Design of a device to be fully fabricated with a 3D-printer.....	94
Figure B.1 Replicate CT scans of device 1-1.	112
Figure B.2. Precision of concentricity error measurements in triplicate CT scans of device 1-1.	113
Figure B.3. CT scans of design 1.....	114
Figure B.4. CT scans of design 2.....	115
Figure B.5. CT scans of device 3.....	116
Figure B.6. CT scans of device 4.....	117
Figure B.7. Particle size distributions obtained with device 1-1.	118
Figure B.8. Particle size distributions obtained with device 1-3.	118
Figure B.9. Particle size distributions obtained with device 2-1.	119
Figure B.10. Particle size distributions obtained with device 2-2.	119
Figure B.11. Particle size distributions obtained with device 2-3.	119
Figure B.12. Particle size distributions obtained with device 3-1.	120
Figure B.13. Particle size distributions obtained with device 3-2.	120
Figure B.14. Particle size distributions obtained with device 3-3.	120
Figure B.15. Particle size distributions obtained with device 4-1.	121
Figure B.16. Particle size distributions obtained with device 4-2.	121

Figure B.17. Particle size distributions obtained with device 4-3.	121
Figure B.18. Interquartile range of alginate bead size number-weighted distribution and maximum concentricity error at each flow rate.	122
Figure B.19. Interquartile range of alginate bead size volume-weighted distribution and maximum concentricity error at each flow rate.	122
Figure B.20. Interquartile range of alginate bead size number-weighted distribution and misalignment angle at each flow rate.	123
Figure B.21. Interquartile range of alginate bead size volume-weighted distribution and misalignment angle at each flow rate.	123
Figure B.22. NPI before manual disaggregation.	124
Figure B.23. NPI after manual disaggregation.	124
Figure B.24. Empty alginate beads.	125
Figure B.25. Tween 20 alginate beads.	125
Figure B.26. Span 80 alginate beads.	126
Figure B.27. Alginate capsules containing NPI produced at outer flow rate of 30 mL/min.	126
Figure B.28. Alginate beads containing NPI produced at outer flow rate of 40 mL/min.	127
Figure B.29. Alginate capsules containing NPI produced via emulsification-internal gelation.	128
Figure B.30. Side projections of scans using iron oxide particles as contrast agents.	129
Figure B.31. CT scan using colloidal dispersions of iron oxide nanoparticles as contrast agent.	129

List of Abbreviations

ANOVA	analysis of variance
anti-IL-2R α	anti-interleukin-2 receptor α
ART	aligned rank transform
ATP	adenosine triphosphate
BABB	benzyl alcohol benzyl benzoate
CAD	computer-aided design
CCD	cooled charge-coupled device
CHO	Chinese ovary hamster
CI	confidence interval
CoM	center of mass
CT	X-ray computerized tomography
CV	coefficient of variation
DAPI	(4',6-diamidino-2-phenylindole)
DI	deionized water
DICOM	digital imaging and communications in medicine
DMEM	Dulbecco's modified Eagle's medium
FITC	fluorescein isothiocyanate
G	gauge
GFP	green-fluorescent protein
GIP	glucose-dependent insulinotropic polypeptide
GLP-1	glucagon-like peptide 1
HEPES	4-(2-hydroxyethyl)-1-piperazineethanesulfonic acid
ID	inner diameter
IEQ	islet equivalents
IL-2	interleukin 2
IQR	interquartile range
LOWESS	locally weighted scatterplot smoothing
LSCM	laser scanning confocal microscopy
mAb	monoclonal antibody
MIN	mouse insulinoma
NPI	neonatal porcine islets
OPT	optical projection tomography
PDMS	poly(dimethylsiloxane)
PFTE	polytetrafluoroethylene
PLL	poly-L-lysine
PP	pancreatic polypeptide
PPAR γ	peroxisome proliferator-activated receptor γ
RGB	red-green-blue color model
SGLT2	sodium-glucose co-transporter 2

SW
UV

southwest
ultraviolet

List of Symbols

c	weight per volume concentration of alginate
Ca	capillary number
d	theoretical droplet diameter
$D[2,0]$	number area mean diameter
$D[4,3]$	volume moment mean diameter
D_i	diameter of inner channel
D_o	diameter of orifice
f	droplet formation frequency
G	effective elongation rate
h	height of microfluidic channel
$IQR_{2,0}$	IQR of number-weighted distribution
$IQR_{4,3}$	IQR of volume-weighted distribution
N	number of droplets detached from interface per unit time
Q	volumetric flow rate
R_d	theoretical radius of droplet
R_j	theoretical radius of jet
R_o	radius of orifice
Re	Reynolds number
s	spacing between droplets
U	linear velocity
V_a	droplet volume estimated from image analysis
w	width of microfluidic channels
w_o	width of orifice
We	Weber number
$[\eta]$	intrinsic viscosity
ΔZ	distance from inner channel to orifice
ϕ	disperse-to-continuous phase volumetric flow rate ratio
ι	interval between droplets
λ	disperse-to-continuous phase viscosity ratio
σ	interfacial tension
μ_c	viscosity of the continuous phase (mineral oil)
μ_d	viscosity of disperse phase (alginate)
μ_s	viscosity of solvent

Acknowledgements

I greatly appreciate the opportunity to work under the supervision of Jamie and Urs; I am forever thankful for their patience, advice and guidance. Thanks a lot to both for your trust throughout this project. I am very grateful for the invaluable help provided by Dr. Karen Cheung and Dr. Linfen Yu. I thank Dr. Ujendra Kumar for his insightful feedback and discussions. I thank Dr. Gregory Korbitt and Cara Ellis at the Department of Surgery in the University of Alberta for contribution of neonatal porcine islets.

I thank Chris Sherwood for being a proficient and fun lab manager. I am grateful to Blanche for her disposition to offer help and for her contributions to this work. Roger Kiang and Erin Charman were extremely helpful in the early stages of this project. John Schipilow was diligent in doing CT scans, provided helpful advice on image analysis and training for the OPT scanner. Guobin Sun provided training and help with confocal microscopy. David CC provided training and advice for 3D printing. I also thank all Piret and Hafeli lab members for their support and input.

A mis padres, les agradezco todo el apoyo que me han proveído sin el cual no podría haber empezado y terminado esta maestría. También quiero darle las gracias a los doctores Pedroza (Jorge, Gaby e Isabela) por ser una fuente de inspiración y motivación para completar este proyecto. Le agradezco a Cheche por brindarme las herramientas para realizar este proyecto. 恭子へいろいろありがとうございました、終わったよ！

I received a fellowship from the National Council of Science and Technology (CONACyT). The Canadian Stem Cell Network also provided travel grants.

Dedication

A la memoria de Marianita y Tere.

Chapter 1: Introduction

Diabetes mellitus is a metabolic disease characterized by high blood glucose levels, *i.e.*, hyperglycaemia, resulting from the impairment of insulin secretion (type 1) and/or the development of insulin resistance (type 2). Hyperglycaemia causes abnormal glycation of proteins that can lead to severe circulatory problems, increased cardiovascular risks, renal failure and retinopathy, among other conditions. As of 2014, diabetes affects ~9% of adults worldwide (World Health Organization 2014), and it is estimated that over 300 million people will suffer from diabetes by 2030 (Mathers & Loncar 2006). In Canada, as of 2013, there were almost 2 million diabetics (Statistics Canada 2013), and according to the Canadian Diabetes Association, between 5 – 10% of them are afflicted by type 1 diabetes (Canadian Diabetes Association n.d.).

Type 2 diabetes is commonly associated with obesity, and can be managed by a combination of life-style modifications (*e.g.*, meal planning and physical activity) and pharmaceuticals devised to reduce blood glucose levels (*i.e.*, antidiabetic drugs). There is a relatively wide gamut of antidiabetic therapeutics and combinations available to manage type 2 diabetes, including oral medications (Table 1.1). Conversely, type 1 diabetes, which is caused by the autoimmune-mediated destruction of the insulin-producing β cells from the pancreas, always requires insulin replacement therapy via subcutaneous injections to control blood glucose levels (Mansell & Arnason 2015).

The Diabetes Control and Complications Trial was a landmark study that demonstrated that insulin replacement therapy complemented with frequent self-monitoring can effectively reduce blood glucose levels to delay further complications from type 1 diabetics (Skyler 2004). Nonetheless, insulin therapy normally does not offer optimal glycemic control and can incur episodes of extremely low blood glucose levels (*i.e.*, hypoglycemia) that can cause loss of

consciousness and seizures leading to permanent damage to the nervous system. The advent of insulin pumps and continuous blood-glucose monitoring systems have augmented the precision of insulin dosing. There are also closed-loop control systems capable of reducing hypoglycemic episodes by utilizing the alternating infusion of insulin and glucagon (Russell *et al.* 2014). Yet, the performance of these devices does not resemble the blood glucose control achieved by a functional pancreas, and most commercially available devices remain open-loop and un-integrated, requiring the patient to perform calorie counts to adjust insulin dosage.

Table 1.1. Classes of antidiabetic drugs.

Class	Example	Mechanism of action	Route	Indication
α -glucosidase inhibitors	Acarbose	Delay glucose absorption by inhibiting hydrolyzation of saccharides to glucose.	Oral	Type 2 diabetes
Biguanides	Metmorfin	Reduce hepatic glucose production and increase sensitivity of muscle tissue to insulin.	Oral	Type 2 diabetes
Dipeptidyl peptidase-IV inhibitors	Sitagliptin	Stimulate β -cells to release insulin by suppressing the degradation of glucagon-like peptide-1 (GLP-1) and glucose-dependent insulinotropic polypeptide (GIP).	Oral	Type 2 diabetes
Incretin mimetics	Exenatide	Have longer half-life than GLP-1. Stimulate β -cells to release insulin by binding to GLP-1 receptor.	Subcutaneous injection	Type 2 diabetes
Insulin		Control cellular intake of glucose.	Subcutaneous injection	Type 1 & type 2 diabetes
Insulin secretagogues	Sulfonylureas, meglitinides	Stimulate β -cells to release insulin by binding to ATP-sensitive potassium channels.	Oral	Type 2 diabetes
Sodium-glucose co-transporter 2 (SGLT2) inhibitors	Canagliflozin	Reduce glucose reabsorption in the kidneys.	Oral	
Thiazolidinediones	Pioglitazone	Enhance insulin sensitivity by activating peroxisome proliferator-activated receptor γ (PPAR γ).	Oral	Type 2 diabetes

This table was constructed using information from e-Therapeutics (Mansell & Arnason 2015).

1.1 Islet transplantation

Whole pancreas transplantation is an effective method to reverse type 1 diabetes and attain insulin independence (Kelly *et al.* 1967). However, this is a high risk procedure and thus only employed for a highly select group of patients who have difficulty controlling their blood

glucose levels and require a simultaneous kidney transplant (Sutherland *et al.* 1987). The introduction of the Edmonton protocol (Shapiro *et al.* 2000) was an important advance since it provided a more effective and less invasive means to attain insulin independence through islet transplantation, *i.e.*, β -cell replacement therapy.

Islets constitute ~2% of the total volume of the pancreas and contain cells responsible for the secretion of glucagon, insulin, somatostatin, ghrelin and pancreatic polypeptide (α , β , δ , ϵ and PP cells, respectively). For islet transplantation, these cell clusters are isolated from the pancreas of cadaveric donors through enzymatic digestion, purified via density gradient separation, and infused into the hepatic portal vein (at ~10,000 islet equivalents/kg of body weight) (Robertson 2004). Shortly after transplantation, the grafted islets begin to sense and control blood glucose levels by releasing insulin at physiological levels in response to glucose, thus minimizing the occurrence of hypoglycemic episodes. Since the procedure involves engraftment of allogeneic donor tissue, transplant recipients are subjected to long-term administration of immunosuppressants to protect the transplanted islets from allogeneic rejection. This immunosuppression regime begins immediately before transplantation with 5 bi-weekly doses of daclizumab, an anti-interleukin-2 receptor α (anti-IL-2R α) mAb, and maintained with continuous administration of rapamycin and tacrolimus, inhibitors of the IL-2 response and calcineurin, respectively (Berney *et al.* 2004).

In the cohort subjected to Edmonton protocol, over 90% of the patients had insulin independence lasting less than 5 years (Ryan *et al.* 2005), suggesting that future islet recipients will require multiple islet infusions to maintain long-term blood glucose control. However, most islet infusions necessitate the pancreas of two or three human cadaveric donors so this further limits the application of islet transplantation to a few patients with recurrent hypoglycemia and

poor symptom recognition (Sogayar *et al.* 2005; Vaithilingam & Tuch 2011; Robertson 2004). Segmental pancreas transplantation from the relatives of patients has been employed as an effort to increase the availability of donor tissue, but post-operative complications represent major risks to donors and the approach requires strict exclusion criteria (*e.g.*, obesity, abnormal glucose tolerance, and/or abnormal islet-cell antibodies) (Sutherland *et al.* 2001).

Another challenge limiting the widespread application of islet transplantation is that the side effects of immunotherapy pose serious risks to the transplant recipient (*e.g.*, lymphopenia, long-term toxicity, mouth ulcerations, dyslipidemia, myelotoxicity, increased risk of pneumonia and other opportunistic infections) (Berney *et al.* 2004; Piper *et al.* 2004). Additionally, there are concerns about the side effects of immunosuppression on graft survival (*e.g.*, diabetogenicity of tacrolimus, homeostatic peripheral expansion of autoreactive and alloreactive T cell populations) (Berney *et al.* 2004; Van Belle & Von Herrath 2008).

1.2 Neonatal porcine islets

There has been great interest in finding alternative sources for the cellular therapy of diabetes since the demand for human islet donors far exceeds their availability and this has hindered the more widespread application of islet transplantation. To satisfy the demand, alternatives considered include transformed human β -cell lines (de la Tour *et al.* 2001), and *ex vivo* islet expansion (Bonner-Weir *et al.* 2000). More recently, stem cell-derived pancreatic progenitors that secrete insulin have also demonstrated their capabilities for restoring blood glucose control in animal models (Kroon *et al.* 2008; Rezanian *et al.* 2011; Schulz *et al.* 2012; Pagliuca *et al.* 2014; Rezanian *et al.* 2014).

Alternatively, use of xenogeneic tissue, *e.g.*, pig islets, provides a virtually unlimited and readily available supply of islets for transplant; moreover, porcine insulin resembles its human homologue, has equivalent physiological levels and is functional in humans (Hering & Walawalkar 2009). Pig islets also have the potential to offer transplantable islets with superior and consistent quality because they are not compromised by human islet comorbidities, senescence, brain death, and cold ischemia injury. Pig islets can be obtained from adult, fetal or neonatal animals (*e.g.*, neonatal porcine isles, NPI). Isolation of adult pig islets is costly due to animal maintenance, and once isolated the islets are difficult to maintain in culture with poorly reproducible process yields. Fetal pig islets are less difficult to maintain in culture but they require long maturation periods to attain glucose-induced insulin secretion. Conversely, NPI can be isolated consistently in high yields and already secrete low levels of insulin *in vitro* (Korbitt *et al.* 1996). Furthermore, NPI transplants have been reported to restore blood glucose control in immunodeficient mice after 6 – 8 weeks of *in vivo* maturation, and reverse hyperglycemia after one month in immunocompetent allogeneic pig and xenogeneic non-human primate transplants. NPI also exhibit resistance to hypoxia-induced apoptosis in the early post-transplant setting, especially when compared to adult human and mouse islets (Emamaullee *et al.* 2006).

Human xenogeneic transplantation using NPI requires approaches to prevent recognition by pre-formed antibodies against the glycation patterns on the epithelial cells of non-primate mammals, that can lead to graft rejection and destruction. Genetic modification of pigs could enable attenuation of such antigens besides providing a platform for stable overexpression of genes encoding cytoprotective and immunomodulatory peptides in order to reduce the need for immunosuppression (Marigliano *et al.* 2011). However, these improved xenogeneic islets are not yet available and the overall effectiveness of this approach remains to be seen.

1.3 Islet encapsulation

Islet transplantation should benefit from the continued development of more effective and milder immunosuppressive therapies, but strategies to reduce, minimize or eliminate the burden of immunosuppressive therapy could greatly improve its applicability with the added benefit of facilitating the use of alternative islet sources (Souza *et al.* 2011).

Encapsulation of islets, *i.e.*, immobilization within an inert semi-permeable membrane that allows the passage oxygen, glucose and insulin (~6 kDa) while blocking the transport of antibodies (≤ 150 kDa) and immune cells (~7 μm), has been studied for over 80 years as a means to achieve immunoisolation (Vaithilingam & Tuch 2011). Extravascular encapsulation devices are likely to be more appropriate for islet transplantation than intravascular encapsulation devices (*e.g.*, shunts) because the former do not incur the risk of thrombus formation and can be retrieved more easily. Extravascular encapsulation devices with planar geometry implanted subcutaneously have been used successfully to reverse hyperglycemia with murine islets (Yang *et al.* 2002), human β -cell precursors (S.-H. Lee *et al.* 2009) and NPI (Sörenby *et al.* 2008; Elliott *et al.* 2005) in allogeneic rat transplantation models (Sweet *et al.* 2008), as well as xenogeneic transplantation models. Other encapsulation devices have been fabricated by casting an alginate sheet containing islets, cross-linked with additional layers of alginate on both sides; these thin (~250 μm thick) devices allow retrieval of the encapsulation islets, and have successfully maintained blood glucose control in murine xenogeneic (Lamb *et al.* 2011) and canine allogeneic (Storrs *et al.* 2001) transplantation models. However, long-term graft survival remains a major concern hindering the clinical application of such devices (Vaithilingam & Tuch 2011).

1.3.1 Microencapsulation in alginate

In the aforementioned devices, the whole islet volume is immobilized in one or a few devices. Alternatively, one or a few islets can be encapsulated in <1 mm-sized semi-permeable spheres that provide a large volume-to-surface area ratio for nutrient and insulin transport. This is known as microencapsulation.

Alginate is an ideal material for islet encapsulation. It is a natural biopolymer obtained from brown algae composed of β -D-mannuronic acid and α -L-guluronic acid, and, under mild conditions without affecting islet viability and function, can be cross-linked into hydrogels stabilized by polycations such as Ca^{2+} . These characteristics allow the facile fabrication of microcapsules by preparing a mixture of the islets and the alginate in solution, that is then dispersed into small droplets, each containing a few islets, and these droplets are solidified by Ca^{2+} or other divalent cations. Typically, the alginate phase is dispersed into microdroplets by extruding the solution through a nozzle where droplets are formed under the influence of gravity. This is often facilitated by nozzle vibration, coaxial airflow or electrostatic repulsion, and then the droplets drip into a calcium solution bath to achieve cross-linking (Hoesli 2010). This approach, known as extrusion-external gelation, allow the fabrication of small microcapsules of uniform size (and down to < 200 μm), but can yield tear-shaped droplets that may lead to pericapsular fibrotic overgrowth (Vaithilingam & Tuch 2011) hence potentially compromising graft survival.

Hoesli *et al.* proposed emulsification-internal gelation as a scalable alternative to encapsulate islets (2010; 2011) that allows the fabrication of capsules from concentrated (5% w/v) alginate solutions. This process yields smooth spherical microcapsules with smaller pores that excluded more antibody-sized molecules *in vitro*, and improved graft survival in murine

allogeneic transplantation models (Hoesli *et al.* 2012). This process was adapted from the work of Poncelet *et al.* (1995), and depends on supplementing the alginate-islet mixture with insoluble CaCO_3 , and emulsification into smaller droplets by stirring with mineral oil in a closed vessel (*e.g.*, spinner flask). Gelation of the alginate droplets in the emulsion is achieved by addition of acidified mineral oil containing acetic acid (*i.e.*, oil-soluble acid with rapid partitioning to the aqueous phase) that causes a drop in pH and release of soluble Ca^{2+} from the carbonate. Importantly, unlike the aforementioned encapsulation processes based on extrusion-external gelation, emulsification-internal gelation is amenable for the generation microcapsules from concentrated alginate solutions (Hoesli 2010). However, a disadvantage of emulsification-internal gelation when compared to extrusion-external gelation is the production of alginate capsules with a broader size distribution, with some microcapsules that could be too small to embed islets, while others might be too big to allow a sufficient supply of oxygen to the encapsulated islets. Overall, such polydispersity in the size distribution of alginate microcapsules might not be an optimal use of the transplant volume.

Encapsulation of bioactive species, including cells and islets, can be achieved using microfluidic droplet generators that exploit the interactions between immiscible fluids to create discrete volumes (Seemann *et al.* 2012). While emulsification-internal gelation takes advantage of shear induced instabilities of the alginate-mineral oil interface to produce thousands of droplets at a time, microfluidic droplet generators disperse the alginate mixture drop by drop and has the advantage of producing monodisperse (*i.e.*, uniformly sized) droplets that can then be cross-linked to yield alginate microcapsules. Droplet generation in microfluidic devices relies on two immiscible fluids encountering in a junction where local fluid stresses acting to deform the interface compete with capillary pressure resisting interface deformation. Eventually interfacial

instabilities initiate droplet pinch off from the interface, with steady flow of both fluids, periodic formation of uniformly-sized droplet is achieved (Christopher & Anna 2007). The geometry of the fluid junction, flow rate and the physical properties of the fluids (*i.e.*, interfacial tension, viscosity) dictate the characteristics of the interface formed and hence the size of the resulting droplets as well as the frequency of production (Baroud *et al.* 2010). The most common types of fluid junction geometries of microfluidics droplet generators are T-junctions, co-axial flow and flow-focusing (Christopher & Anna 2007). In T-junctions, droplet formation is achieved by flowing the immiscible fluids perpendicularly; in co-axial flow devices, the fluids flow in parallel; while flow-focusing devices combine cross-flow and co-flow to form an elongated interface, *i.e.*, two counter-flowing streams of the outer fluid squeeze the inner fluid, and typically are forced through an orifice (Christopher & Anna 2007; Baroud *et al.* 2010). Examples of the application of microfluidic droplet generators with the aforementioned geometries for encapsulation in alginate are shown in Table 1.2.

1.4 Fabrication of microfluidic droplet generators

Early microfluidic devices were fabricated in silicon and glass through photolithography and etching, but these processes have to be performed in cleanroom environments and the substrates are expensive. Conversely, polymers constitute less expensive substrates that can be casted and sealed with adhesives or via low temperature thermal bonding. A salient example of the latter is Poly(dimethylsiloxane) (PDMS), a nontoxic elastomer that can reproduce micron-sized features with high fidelity via replica molding, cures (*i.e.*, solidifies) at low temperatures (60°C), and can be sealed reversibly through van der Waals forces or permanently through covalent bonds after exposure to air plasma. Fabrication in PDMS is known as soft lithography

and involves the following steps: (i) design of the channels of the device in computer-aided design (CAD) software, (ii) printing of the drawing in a transparency to generate a mask, (iii) use of the mask in contact photolithography to produce a “master” (*i.e.*, a positive relief of the mask in photocurable epoxy on a silicon wafer), (iv) replica molding by casting PDMS against the master and curing, (v) removal of PDMS negatives from the master, sealing of the channels (*e.g.*, by bonding with PDMS or glass) (McDonald *et al.* 2000). This fabrication approach results in microfluidic devices with rectangular channels, but cylindrical channels can also be fabricated in PDMS with hemicylindrical reliefs of photocurable epoxy generated through casting and curing on base molds covered with thin deflectable PDMS membranes (Kang *et al.* 2010). Microfluidic droplet generators with cylindrical channels have also been fabricated in PDMS by removing the insulation layer (0.75 mm) from optical fibers (0.25 mm) and casting PDMS blocks on them, after curing the fiber was removed and glass capillaries were inserted to serve as inlet and outlet (Takeuchi *et al.* 2005). However, these approaches to fabricate cylindrical channels in PDMS might not be appropriate if iterative approaches are employed for device development, as the former would require the production of several hemicylindrical reliefs and base molds, while the latter might be hindered by the limited sizes of optical fibers available and the difficulty in alignment of glass capillaries. Alternatively, droplet generators have been fabricated in photopolymers using stereolithography (Morimoto *et al.* 2009), *i.e.*, an additive manufacturing approach utilizing 3D-printers where layers of polymer (~25 – 100 μm thick) are deposited and cured by UV laser exposure one at a time (Melchels *et al.* 2010; Skoog *et al.* 2014); however, the resolution of this fabrication method (~20 μm), even though it is the best among rapid prototyping strategies (50 – 200 μm) (Melchels *et al.* 2010), does not allow the fabrication of channels as small as those obtained through soft lithography. Still, droplet generators fabricated

through stereolithography could potentially be used for encapsulation of islets, which typically are larger than 100 μm .

Table 1.2. Current state of alginate encapsulation using microfluidic droplet generators.

Device description	Capsule size ¹	Cross-linking strategy	Alginate concentration & encapsulant	Reference
Axisymmetric flow-focusing geometry with 250 μm orifice fabricated using stereolithography	32.4 μm (4.4%)	Internal gelation	1% w/v <i>Chlamydomonas reinhardtii</i>	(Morimoto <i>et al.</i> 2009)
Co-axial flow geometry fabricated with 300 μm needle inside 2.5-mm glass tubule	48 μm (16.7%)	None ²	2% w/v CHO-K1 cells	(Sakai <i>et al.</i> 2004)
T-junction geometry fabricated in PDMS with separate perpendicular channels for cross-flow of oil phase, alginate, encapsulant and cross-linker	75 μm (1.5%)	External gelation	1% w/v GFP producing yeast cells	(Choi <i>et al.</i> 2007)
T-junction geometry fabricated in PDMS with downstream addition of oil with acetic acid	100 – 150 μm ($< 3.2\%$)	Internal gelation	2% w/w Jurkat cells	(Tan & Takeuchi 2007)
Flow-focusing geometry with three inlets (oil, alginate + CaCO_3 , alginate + cells), and two junctions (alginates merged, then oil merged), fabricated in PDMS	35 μm (not reported)	Off-chip Internal gelation	1.5% w/v M6C cells	(Akbari & Pirbodaghi 2013)
Co-axial flow geometry with 8 outlets employing compressed air for alginate dispersion, fabricated using stereolithography.	$\sim 715 \mu\text{m}$ (not reported) ³	External gelation	3% w/v Rat islets	(Tendulkar <i>et al.</i> 2012)
Commercially available device (snake mixer slide by Thinxxs, Germany) with Y-junction flow geometry fabricated in a cycloolefin co-polymer	234 μm (21.2%)	External gelation	2% w/v None	(Capretto <i>et al.</i> 2008)
	249 μm (11.8%)	Internal gelation		
	225 μm (11.4%)	Partial gelation ⁴		
T-junction geometry fabricated in polytetrafluoroethylene (PFTE)	297 μm (7.6%)	External gelation	0.65% w/v Rat islets	(Wiedemeier <i>et al.</i> 2011)

¹In studies where capsules were generated at more than one flow rate, the minimal capsule size is reported. Polydispersity in the size distribution of capsules is

reported between parentheses in terms of the coefficient of variation (CV), which is defined as the standard deviation divided by average capsule diameter

expressed as a percent. ²Authors documented and reported the size of ungelated alginate droplets. ³ Estimated from micrographs in the article (n = 3 capsules).

⁴Approach consists in adding 0.375% w/v BaCl_2 to alginate prior to injection, and full cross-linking through external gelation after the capsules are formed.

1.5 Research goals

Islet transplantation represents an alternative to treat type 1 diabetes that reduces recurrence of hypoglycemia compared to conventional insulin therapy, and could potentially reverse diabetes. Currently, however, these benefits have to be weighed against the risks associated with life-long immunosuppression thus limiting the applicability of this therapy to the most severe cases of type 1 diabetes; additionally, even for this select group of recipients, islet availability further restricts the application of islet transplantation. Islet microencapsulation in alginate prior to transplantation can overcome these problems by allowing the use of readily available and virtually unlimited sources of islets like NPI, while prospectively diminishing or abolishing the need for immunosuppressive therapy. Using concentrated alginate solutions, emulsification-internal gelation allows the production of microcapsules with superior immunoisolation properties but with polydisperse size distributions; conversely, extrusion-internal gelation techniques are able to produce microcapsules with uniform size but are not compatible with concentrated alginate solutions.

The overall goal of this study was to develop droplet generators capable of generating alginate capsules from concentrated alginate solutions with a narrow size distribution for the encapsulation of NPI. Novel droplet generators were constructed using two different fabrication techniques (soft lithography and 3D-printing) and, using an adapted emulsification-internal gelation approach, employed for encapsulation of pancreatic cells. These droplet generators were employed in order to fulfill the following specific aims:

1. Compare the performance of the devices in terms of their throughput and resulting size distribution when fabricating 5% alginate beads without cells, *i.e.*, empty alginate beads.
2. Assess the effect of processing on pancreatic cell survival.

After encapsulation of NPI, a supplementary goal was to explore imaging techniques capable of detecting partially encapsulated islets to add another dimension in the comparison of encapsulation approaches, as well as provide a platform for the assessment of separation processes aimed to remove defective capsules.

Chapter 2: Materials and methods

2.1 Pancreatic cells

2.1.1 Neonatal porcine islets

Primary pancreatic cell clusters were isolated by Dr. Greg Korbitt's group (University of Alberta) and shipped in proprietary islet media for transport (Prodo Laboratories Inc., Irvine, CA) to Vancouver after 7 days of culture (Korbitt *et al.* 1996). On arrival, neonatal porcine islets (NPI) were counted on an inverted microscope (AE31, Motic, Hong Kong) before and after handling. NPI were triturated by gently pipetting up and down ten times using a 10-mL pipette to break cluster aggregates generated during shipping into single NPI, seeded at approx. 1,000 islet equivalents (IEQ) per mL in 125-cm² suspension culture T-flasks (Sarstedt, Germany), and maintained up to 1 week with Hams F10 medium supplemented with 10 mM nicotinamide, 10 mM D-glucose, 2 mM glutamine, 1.6 mM CaCl₂, 0.5% v/v bovine serum albumin, 50 mM 3-isobutyl-1-methylxanthine (all from Sigma, St. Louis, MO), 14.3 mM NaHCO₃ (Fisher Scientific, Waltham, MA), 100 units/mL penicillin and 100 µg/mL streptomycin (all from Invitrogen, Carlsbad, CA) referred to as “complete F10”, at 37 °C and 5% CO₂ in a humidified incubator.

2.1.2 MIN6 cell line

The immortalized murine pancreatic β-cell line MIN6 was a gift from Dr. Jun-Ichi Miyazaki (University of Osaka) (Miyazaki *et al.* 1990). Adherent and encapsulated cells were cultured in DMEM supplemented with 10% v/v fetal bovine serum, 6 mM glutamine, 100 units/mL penicillin and 100 µg/mL streptomycin (all from Invitrogen), referred to as “complete

DMEM". Adherent cultures were seeded at $4 \cdot 10^4$ cells/cm² in tissue culture treated T-flasks (Sarstedt) and maintained at 37 °C and 5% CO₂ in a humidified incubator.

2.2 Reagents

2.2.1 Cross-linker suspension

A stock was prepared by adding 2 g CaCO₃ (Mallinckrodt Baker, Ireland) to 20 mL process buffer, consisting of 10 mM HEPES (Sigma), 170 mM NaCl (Fisher Scientific) at pH 7.4. The suspension was autoclaved for 30 min, and stored at 4 °C.

2.2.2 Mineral oil and acidified oil

Acidified oil was prepared by dissolving 4 mL of glacial acetic acid in 2 L of light mineral oil (all from Fisher Scientific), stirred overnight at 700 rpm on a hot plate magnetic stirrer. The mineral oil and acidified oil were sterilized using 500-mL Stericup[®] disposable vacuum filtration units (Millipore, Billerica, MA) under aseptic conditions, and stored at room temperature.

2.2.3 Alginate

The alginate stock solution was prepared by dissolving 2.62 g ultrapure low viscosity high guluronate content sodium alginate and 0.29 g ultrapure low viscosity high mannuronate content sodium alginate (all from Pronova/Novamatrix, Norway) in 50 mL of process buffer. The solution was stirred overnight on a hot plate magnetic stirrer (RCT basic safety control, IKA, Wilmington, NC) at 100 rpm and 40 °C. Complete dissolution of the alginate powder was achieved by supplementing the stirring with mixing overnight in a bottle roller (Bellco Biotechnology, Vineland, NJ) at 4 rpm and 37 °C. The alginate solution was autoclaved at 121

°C, 1.1 atm for 30 min. To avoid spills, the alginate stock solution was retrieved after the temperature inside the autoclave's chamber dropped below 40 °C. The alginate stock solution was stored at 4 °C.

Prior to generation of alginate beads, 1.8 mL alginate stock solution were warmed to room temperature and transferred to the barrel of a sterile 10-mL Luer lock tip syringe (BD Biosciences, San Jose, CA) capped with a female Luer lock plug (Cole-Parmer, Vernon Hills, IL). The cross-linker solution was re-suspended by vortexing, then 100 μ L were added to the syringe and mixed using a sterile tapered blade spatula (Corning, Corning, NY). The plunger was replaced, and the mixture was degassed by centrifugation at 100 x g for 1 min. The degassed mixture was transferred to the barrel of another capped syringe, while simultaneously adding 200 μ L process buffer. The plunger was replaced, and the syringe was rotated gently for 1 min to mix the solutions. The syringe was held upright to let the mixture settle on the plunger, the headspace was evacuated, and the syringe was re-capped and stored at room temperature until further use.

2.3 Microfluidic droplet generators

2.3.1 Design and fabrication

Devices were drafted in AutoCAD 2011 (Autodesk, San Rafael, CA). The microfluidic channel layout (Figure 2.1) consisted of three 1.6-mm circular chambers upstream converging in two junctions. The first junction had a T-shape, where the alginate flow in the inner channel was focused with mineral oil flow from the outer channels, and was followed by an inverted nozzle, where the alginate phase was broken into droplets. The second junction had a Y-shape, and allowed the injection of acidified oil. A fourth 2.4-mm circular chamber downstream of the junctions served as outlet.

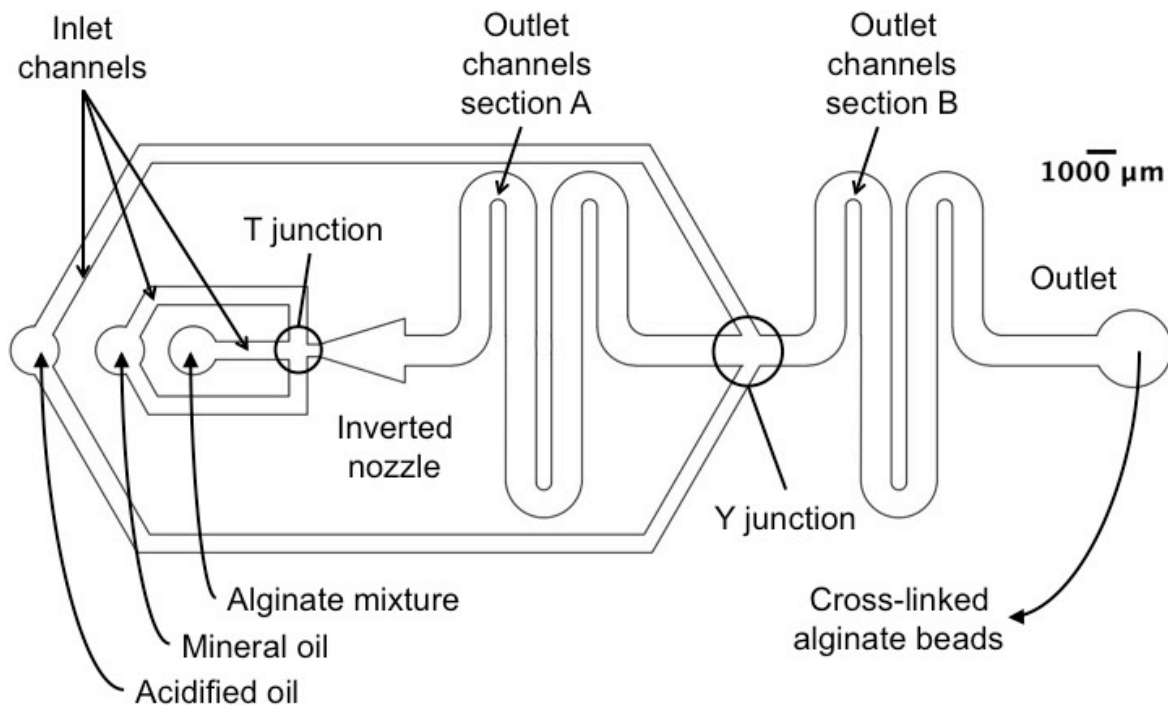


Figure 2.1. Channel layout of microfluidic devices.

Inlet channel width was set at 600 μm . The inverted nozzle expanded from 400 μm to 2,100 μm at the outlet at 17°. After the nozzle, the outlet channel width was set at 1,000 μm .

In collaboration with Dr. Linfen Yu from Dr. Karen Cheung's laboratory, the design was patterned by standard contact photolithography into a silicon substrate using SU-8 photoresist to generate a master mold, resulting in features with a height of 480 μm .

Devices were fabricated in Sylgard 184 poly-(dimethylsiloxane) (PDMS) elastomer (Dow Corning, Midland, MI). The PDMS base and hardener were mixed in a 10:1 ratio using an automatic mixer, poured onto the mold and degassed for 30 min, followed by curing overnight at 60 °C.

The cured replica was peeled off the mold and cut into blocks embossed with the features on the bottom face. Holes traversing the blocks were punched in the inlets using a 1 mm biopsy

punch. Additional blocks of similar size were cut from the PDMS rubber leftovers and 1.5-mm holes were punched in them.

To assemble a device, a PDMS block with features and a leftover block were exposed to short oxygen plasma treatment. Then, the blank block was bonded to the bottom of the block with features while aligning the 1.5-mm hole with the outlet. Finally, the features were sealed to form channels by bonding the PDMS block with features to a microscope slide through further plasma treatment. The 1.5-mm hole in the leftover block was not obstructed while sealing, and allowed the in-flow from the top and out-flow through the bottom of the PDMS block.

2.3.2 Operation

The syringe containing the alginate mixture was mounted on a syringe pump (Fusion 400, Chemyx, Stafford, TX). Mineral oil and acidified oil were transferred to 60-mL syringes under aseptic conditions, and mounted on a double syringe pump (Pump 33 twin syringe pump, Harvard Apparatus, Holliston, MA).

The syringes were connected to the device using 40 cm of 4.8-mm PharMed tubing (Cole-Parmer) fitted with female Luer hose barb (RK-45501-08, Cole-Parmer) and male Luer hose barb adapters (RK-45504-08, Cole-Parmer) on each end of the tubing. The male adapters were connected to the each syringe whereas the female adapters were connected to the hubs of 0.5-in long 20G blunt needles (Nordson EFD) inserted on the inlets. The outlet of the device was fitted with 15 cm of 4.8-mm Tygon tubing (Cole-Parmer). A lab jack was used to provide a platform at 30 cm in height to facilitate bead collection from underneath the device.

The alginate line was primed at a flow rate of 2 mL/h, and after 15 min the mineral oil and acidified oil lines were primed at a flow rate of 2.5 mL/h. The mineral oil and acidified oil flow

rates were adjusted to the operating conditions (30 mL/h) after letting the system equilibrate for 5 min. Cross-linked alginate beads were collected in 50-mL conical tubes containing 10 mL process buffer with 1.5 mM CaCl₂, referred to as “storage buffer”.

Alginate beads were recovered after discarding the oil phase, and then washed 3 times with storage buffer, centrifuging at 100 x g for 5 min between steps to accelerate bead settling and phase separation.

In encapsulation experiments, the storage buffer in the collection tubes and washing steps was mixed 10% v/v complete DMEM, and the process buffer volume in the alginate mixture was replaced with MIN6 cell suspension containing $9 \cdot 10^7$ cells/mL.

2.4 3D-printed droplet generators

2.4.1 Design

The channel layout of the devices consisted of two concentric cylindrical channels. Blunt needles (0.5-in long) of 21G or 18G (all from Nordson EFD, Westlake, OH) were used for the inner channel. The structure for the outer channel (Figure 2.2) was drafted in AutoCAD 2011, and consisted of a hollow cylinder with a port for the blunt needle at the top, and a hose barb connector at the bottom serving as outlet. Two additional hose barb connectors orthogonally oriented to the outlet were added near the top of the cylinder. Dimensions of channels and other features are reported in Table 2.1. After drafting, the object in the canvas was relocated to positive X-Y-Z coordinates to avoid truncation while exporting as a STL Gerber file.

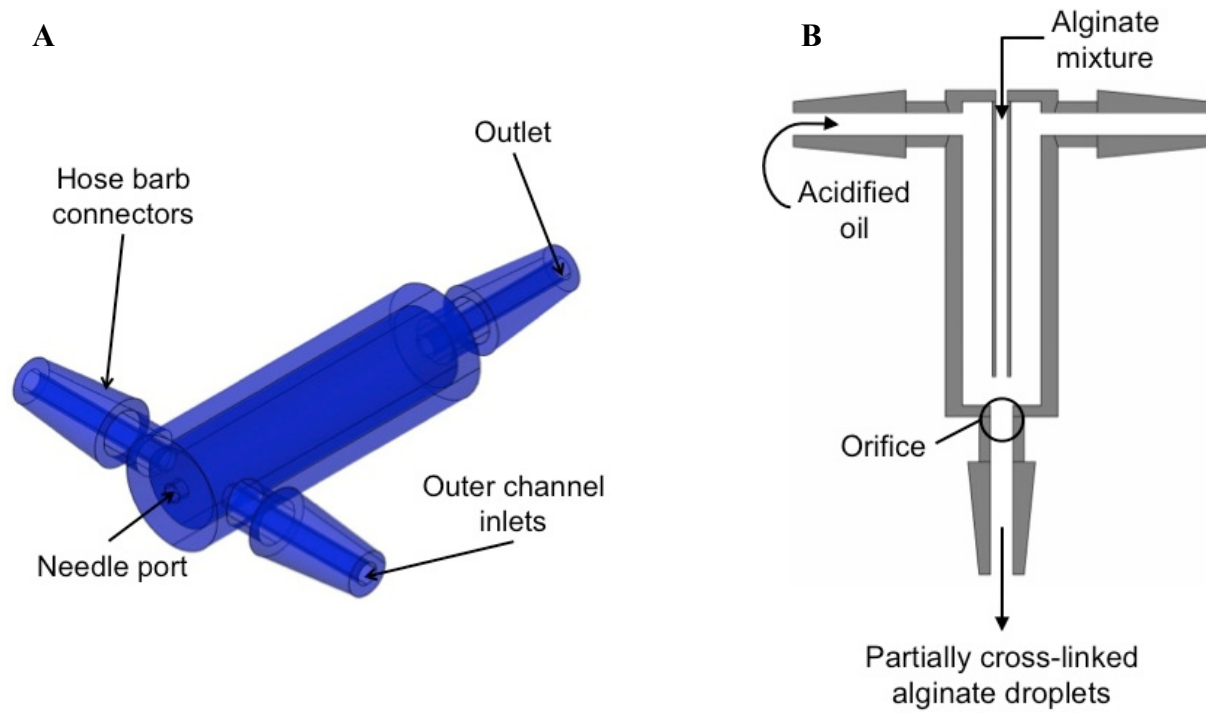


Figure 2.2. Schematic drawing of 3D printed devices.

(A) Isometric southwest (SW) view of the structure for the outer channel. (B) Cross-section of the concentric cylindrical channels.

Table 2.1. Design characteristics of 3D printed devices.

Design	Dimensions in mm				Catalogue numbers of compatible Cole-Parmer parts			
	Oil inlets	Outlet	Inner channel	Barb hose ¹	Tubing (inner diameter)	Male Luer lock barb hose adapter	Female Luer lock barb hose adapter	T-connector
1	1.0	1.0	0.5 (21G)	2.0 3.0 5.0	(1.6 mm) EW-95702-02	EW-45504-00	EW-45501-00	EW-06365-77
2	1.0	1.0	0.5 (21G)	3.1 4.0 5.0	(3.2 mm) EW-96410-16	EW-45504-04	EW-45501-04	EW-40623-66
3	1.0	1.0	0.8 (18G)	3.1 4.0 5.0				
4	1.0	0.7 ²	0.8 (18G)	3.1 4.0 5.0				

¹ Barb hose dimensions are reported as follows: diameter at tip of the connector, maximum barb diameter and barb length. Connector length was 8.8 mm.

² The orifice in device 4 consisted of an inverted nozzle expanding from 700 µm to 1,000 µm at 3°.

2.4.2 Fabrication

Fabrication was performed using an Objet 24 3D printer (Stratasys, Eden Prairie, MN). Before printing, the placement and orientation of the objects on the printing tray were manipulated in Objet Studio software (Stratasys) in order to print the parts from the top of the cylinder to the bottom of the cylinder (Figure 2.3).

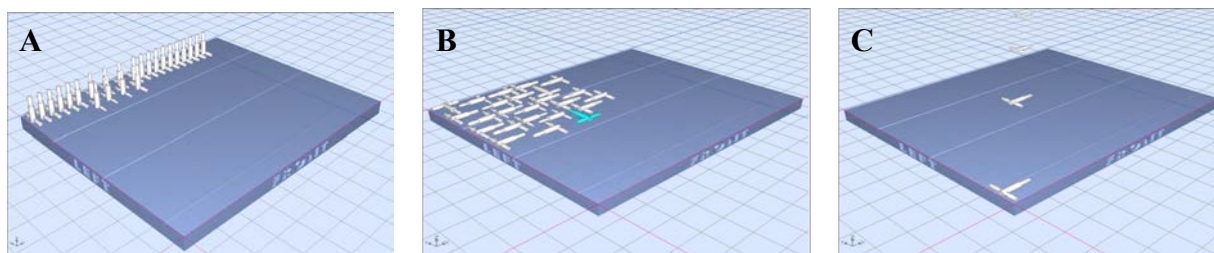


Figure 2.3. Placement of objects in the printing tray.

By default, Objet Studio inserted objects lying on their side and, in some cases, outside of the printing tray (A). The automatic placement function was used to bring all of the objects within the boundaries of the printing tray (B). Then, objects were rotated to minimize the amount of support material in the interior of the cylinder. The new object orientation was locked and automatic placement was used again to minimize the fabrication time (C).

The steps followed after 3D fabrications are depicted in Figure 2.4. First, the excess support material surrounding the parts was carefully removed by hand (Figure 2.4A). Next, the parts were rinsed with tap water to remove traces of support material on the outside. Then, the inlets and the needle ports were cleaned with a 21G blunt needle, while outlets were cleaned with a 2-in long 25G blunt needle (Hamilton, Reno, NV). Lastly, the support material inside of the parts was removed by injecting water 3 times through the outlet using a 21G blunt needle, and the parts were dried with pressurized air (Figure 2.4B).

The concentric cylinder configuration was fabricated by inserting a clean blunt needle through the needle port, which was aligned by inserting a 2-in long 26G needle (Hamilton) through the outlet and gluing the hub of the needle to the needle port using epoxy glue (Devcon, Danvers, MA) with the 26G needle still in place (Figure 2.4C). Designs 1 and 2 used 21G needles with inner diameters $\sim 514 \mu\text{m}$, while the 26G needles used for alignment during the fabrication process had outer diameters $\sim 464 \mu\text{m}$, resulting in a clearance $\sim 50 \mu\text{m}$. Designs 3 and 4 used 18G needles with inner diameters $\sim 838 \mu\text{m}$, and were aligned as described before, but since the clearance between a 18G and a 26G was more than $300 \mu\text{m}$, a 21G needle was inserted from the top between the 18G and 26G needles to reduce the clearance to less than $20 \mu\text{m}$.

Final assembly consisted in adding tubing and Luer lock fittings (Figure 2.4D). A 10-cm piece of compatible tubing was connected to the outlet's hose barb, and a male Luer hose barb adapter was fitted on the opposite end of the tubing. Each inlet was fitted with a 5-cm long piece of tubing, and these tubing pieces were connected to a T-connector. A 15-cm tubing piece of was connected to the third port of the T-connector, and fitted with a female Luer hose barb adapter on the other end. All hose barb connections were secured with 102-mm cable zip ties (Avery Dennison, Glendale, CA).

For encapsulation experiments, assembled devices were placed in individual autoclave bags, and up to 6 individual bags were placed in a larger autoclave bag. Devices were submitted for sterilization in an ethylene oxide chamber at the Animal Research Unit (UBC Hospital).

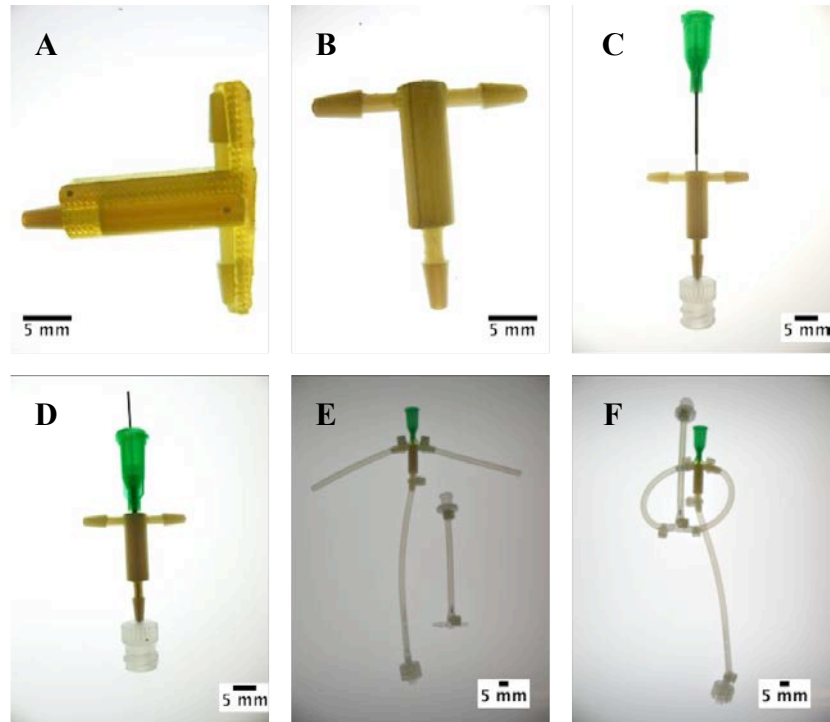


Figure 2.4. Cleaning of 3D printed parts and assembly into devices.

3D printed parts before (A) and after (B) removal of support material. Cleaned parts were fitted with a blunt needle to serve as inner channel (C-D), and then assembled into full devices compatible with Luer lock connectors (E-F).

2.4.2.1 Assessment of needle alignment

Prior to final assembly, the placement of the blunt needle was assessed. The parts were submitted to the Centre for High-Throughput Phenogenomics for imaging in a Scanco Medical μ CT100 X-ray computer tomography specimen scanner (SCANCO Medical AG, Switzerland). The needle hub of part was taped to the cap of a 34-mm cylindrical sample holder, and a preliminary scan was performed to identify the regions of interest and assign the detectors to capture the desired scanned. The definitive scan was performed at 17 μ m/pixel resolution, 70 keV beam energy, 200 μ A current, and 1000 ms integration time. At least 400 projections per sample were captured and reconstructed by the Scanco Medical software suite yielding Z-stacks of 17- μ m thick cross-sections, which were exported as 16-bit DICOM files.

The alignment was measured using a custom macro written in ImageJ freeware devised to track the coordinates of the centers of mass of the needle and of the outer channel structure throughout all cross-sections using the particle analyzer plug-in (see appendix A.1). The X, Y and Z coordinates of the centers of mass of both objects were exported to Excel for analysis (see appendix A.2).

2.4.3 Operation

2.4.3.1 Setup

The outer inlet of the device was connected to mineral oil and acidified oil reservoir bottles using a peristaltic pump as actuator (Masterflex L/S pump, Cole-Parmer). The inner inlet of the device was connected to a syringe containing the alginate mixture, actuated by a syringe pump (Harvard Instruments, Holliston, MA). The outlet of the device was connected to collection and waste bottles, passing through a downstream channel.

The reservoir bottles were two-liter glass bottles (Corning), filled with either mineral oil or acidified oil, and fitted with custom reservoir caps. A custom reservoir cap consisted of an open top screw cap (Corning) on top of a three-port insert (2 inlets, 1 outlet) for connecting flexible tubing. The lower section of the outlet was fitted with a 15-cm piece of 3.2-mm tubing, while the upper section of the outlet was connected to a 10-cm piece of tubing fitted with a male Luer lock barb hose adapter. The inlets were bridged with a piece of tubing to close them.

The reservoir bottles were connected to the outer inlets of a device through a 30-cm piece of 3.2-mm Masterflex tubing mounted on a standard peristaltic pump head (RK-07016-20, Cole-Parmer). The tubing's inlet was fitted with a female Luer lock barb hose adapter, and was connected to the outlets of the reservoir bottles using an autoclavable three-way stopcock (RK-

41507-12, Cole-Parmer). The tubing's outlet was fitted with a male Luer lock barb hose adapter, and was connected to the outer inlet of a device.

The downstream channel consisted of a 2.75-m piece of 3.2-mm tubing, fitted with barb hose-to-female and barb hose-to-male Luer lock adapters for the inlet and outlet, respectively. The tubing's inlet was fitted with a female Luer lock barb hose adapter, and was connected to the outlet of a device. The tubing's outlet was fitted with a male Luer lock barb hose adapter, and was connected to a three-way stopcock. The remaining two ports of the stopcock were connected to the collection and waste bottles through 25-cm pieces of tubing using the corresponding Luer lock barb hose adapters.

The customs caps for the collection and waste bottles consisted of open top screw caps on top of two-port (inlet and exhaust) inserts for connecting flexible tubing. The ports were fitted with 5-cm pieces of tubing containing male Luer lock barb hose adapters. A tubing clamp was added to the inlet of the collection bottle, and the exhausts were fitted with 0.2- μ m membrane filters. The collection bottle was filled with 200 ml storage buffer.

The devices were part of a closed system that could be assembled under aseptic conditions in a biosafety cabinet. Excepting the devices, all components of the system (tubing, fittings, bottles and caps) could be autoclaved for encapsulation experiments.

2.4.3.2 Generation of alginate beads and capsules

After all the components of the system were connected, the closed system was transferred from the biosafety cabinet. The pump head and the syringe were mounted on the peristaltic pump and the syringe pump, respectively.

The acidified oil line was primed at 5 mL/min until the stopcock, and the mineral oil line was primed at 5 mL/min until the T-fitting. To avoid backflow to the inner channel during operation, the alginate line was primed at the operating inner flow rate for 2 min before starting flow in the outer inlet, and the system was equilibrated for 2 min with mineral oil flowing in the outer inlet. The outer inlet's flow rate was adjusted to the desired operating conditions in steps of 5 mL/min lasting 30 s each, and equilibrated for 2 min before changing the upstream stopcock position to replace the outer inlet's flow with acidified oil. After an additional 2 min, collection was engaged by switching the downstream stopcock position, ensuring the collection of cross-linked alginate beads. After collection was completed, the downstream stopcock position was returned to allow flow into the waste bottle, the clamp in the collection bottle was closed, and the collection was transferred to the biosafety cabinet. The volume trapped in the tubing was evacuated into the collection bottle by re-opening the clamp.

Alginate beads were recovered by aspiration of the aqueous phase using wide bore 25/50-mL pipettes (Sarstedt), and washed 3 times with process buffer solution, centrifuging at 100 x g for 5 min between steps to accelerate bead settling and phase separation.

In encapsulation experiments, the buffer in the collection bottle and washing steps was replaced with storage buffer mixed with 10% v/v complete F10, and the process buffer volume in the alginate mixture was replaced with NPI suspension containing either 60,000 or 120,000 IEQ/mL.

2.5 Emulsification-internal gelation

A 200- μ L aliquot of NPI suspension containing 60,000 IEQ/mL was combined with 1.8 mL of alginate stock solution and 100 μ L of cross-linker suspension as described in section

2.4.3.2. This mixture was added drop-wise to 10 mL of mineral oil inside a sterilized spinner flask (Bellco), stirred at approx. 100 rpm. The binary system was emulsified at 1,000 rpm for 12 min, and then 10 mL of acidified oil were added to reduce the pH releasing the calcium ions from the carbonate and cross-linking the alginate droplets. After 3 min, the stirrer speed was decreased to 400 rpm, and the reaction was stopped by adding 40 mL 10 mM HEPES, 170 mM NaCl, pH 7.4 buffer solution mixed with 10% v/v medium. The agitation was stopped after 1 min, and the alginate beads were recovered and washed as previously described in section 2.4.3.2.

2.6 Alginate bead size distribution analysis

Washed alginate beads were stained for 1 h in an orbital shaker (Rotamax 120, Heidolph Instruments, Germany) using 3 g/L toluidine blue (Sigma) in process buffer at 100 μ L/mL of wet bead volume. After staining, the volume was topped to 10 mL with storage buffer, and the solution was transferred to a 10-cm Petri dish. The dish was placed on a light box (Artograph, Delano, MN) with a ruler, and 5 images with a field of view of 12.4 cm x 9.3 cm were captured with a Powershot A630 digital camera (Canon, Japan), gently mixing the sample between snapshots.

Image analysis was performed in ImageJ. Each image was scaled, cropped to a 7.8-cm circular region of interest and converted to an 8-bit image. The contrast and brightness were adjusted by the software, and analyzed using the particle analyzer plug-in (size threshold > 100 μ m, circularity threshold > 0.5), excluding particles in the edges (see appendix A.3).

Using Excel 2011 (Microsoft, Redmond, WA), the areas of the resulting binary masks were converted to diameter measurements of the equivalent spheres, the resulting area-number

distributions were mathematically transformed to volume-weighted distributions, and the descriptive statistics of analytical replicates were calculated. The area-number and volume-weighted distributions were plotted in Prism 5.0b (GraphPad Software, San Diego, CA).

2.7 Cell viability assay

Cell-containing alginate beads were liquefied for 15 min in an orbital shaker at 75 rpm, using a chelating solution consisting of 55 mM citrate, 10 mM HEPES, 90 mM NaCl, pH 7.4 buffer mixed with 10% v/v complete DMEM for MIN6, or complete F10 for NPI. After the alginate capsules were dissolved, MIN6 cells were spun down at 200 x g for 5 min and re-suspended in 1 mL of complete DMEM. NPI were centrifuged at 100 x g for 5 min, and pellets were disaggregated into single cells by incubation in TrypLE (Invitrogen) for 10 min prior to re-suspension. Fifty-microliter aliquots of the cell suspensions were mixed with 50 μ L trypan blue, and counted with a hemacytometer.

Chapter 3: Performance of microfluidic and 3D-printed droplet generators

3.1 Microfluidic droplet generators

3.1.1 Analysis of dimensionless numbers

The capillary number (Ca) was estimated based on the effective elongation rate in flow focusing geometries using Equation 3-1, proposed by Christopher and Anna *et al.* (Christopher & Anna 2007). The effective elongation rate is defined as the linear velocity difference of the continuous phase as it flows into the orifice (see Equation 3-2), where ΔZ is the distance from the end of the inner microchannel to the orifice entrance. In this study's microfluidic devices, the aforementioned distance is equal to the width of the microchannels (*i.e.*, $w = \Delta Z$). The Reynolds number (Re) for each phase was calculated based on Equation 3-3. The alginate flow velocity and shear rate were low in the inlet channel (10^{-6} s^{-1} , assuming injection flow), thus shear thinning of the alginate mixture during operation was unlikely. Therefore, in the determination of Re of the disperse phase, the viscosity of the alginate phase was estimated using Equation 3-4 (Morris *et al.* 1981), where μ_s is the viscosity of the solvent (0.891 mPa·s, assuming water at 25 °C), c is the final weight per volume alginate concentration, and $[\eta]$ is the intrinsic viscosity of the alginate (~500 mL/g) (Owusu-Apenten 2005). The Weber number (We) of the continuous phase was calculated based on Equation 3-5 (Seemann *et al.* 2012).

$$Ca = \frac{\mu_c Q_c}{2\sigma h} \left[\frac{1}{w_o} - \frac{1}{2w} \right] \quad \text{Equation 3-1}$$

$$G = \frac{U_{orifice} - U_{upstream}}{\Delta Z} \quad \text{Equation 3-2}$$

$$Re_i = \frac{2\rho Q}{\mu(w + h)} \quad \text{Equation 3-3}$$

$$\mu_d \approx \mu_s(c[\eta])^{3.3}/10 \quad \text{Equation 3-4}$$

$$We = \frac{\rho_c w_o U_c^2}{\sigma} \quad \text{Equation 3-5}$$

The ratio of volumetric flow rate ($\phi = Q_d/Q_c$) was $6.7 \cdot 10^{-2}$, while the viscosity ratio ($\lambda = \mu_d/\mu_c$) was 126.5. The Ca was $8.5 \cdot 10^{-2}$, indicating that interfacial tension dominated the viscous stresses, as well as suggesting that droplet formation transpired in the dripping regime which is characterized by yielding highly monodisperse droplets with diameters smaller than the orifice (Christopher & Anna 2007). The Re_d and Re_c were $3.2 \cdot 10^{-4}$ and $4.5 \cdot 10^{-1}$, respectively, showing that both phases operated in the laminar flow regime. Finally, the We was $5.8 \cdot 10^{-3}$, revealing interfacial tension as the force governing alginate droplet formation and implying that inertia had little to no effect in the system.

Some of the scaling rules that have been proposed to predict droplet size (d) in flow focusing geometries consider the breakup of the discontinuous phase into droplets due to pure Rayleigh capillary wave instabilities (Equation 3-6) or pure viscous drag (Equation 3-7), where w_A stands for the width of section A of the downstream channel (see Figure 2.1). The theoretical droplet sizes calculated with these equations were 103 μm and 2,101 μm , respectively.

Alternatively, Tan *et al.* proposed estimating the droplet size by rewriting the capillary number as Equation 3-8 (Tan *et al.* 2006), arguing that the difference in the cross-sectional areas at the entrance and exit of the inverted nozzle allow for approximation of the shear rate as the velocity of the oil flow divided by the width of the channel. The theoretical droplet size obtained with this equation was 133 μm .

$$\frac{d}{w_o} \approx \phi^{0.5} \quad \text{Equation 3-6}$$

$$\frac{d}{w_o} \approx \frac{\sigma \phi^{0.5} w_A^2}{Q_c \mu_c} \quad \text{Equation 3-7}$$

$$d \approx Ca \left\{ \frac{\sigma w_o^2 h}{\mu_c Q_c} \right\} \quad \text{Equation 3-8}$$

3.1.2 Particle size distribution

The number area (D[2,0]) and volume moment (D[4,3]) mean diameter of alginate particles generated in three different runs were $449 \pm 10 \mu\text{m}$ and $561 \pm 46 \mu\text{m}$ (average \pm standard error, $n = 3$), respectively (Figure 3.1). The majority of the generated alginate beads ($\sim 85\%$ by number) had a size between $300 \mu\text{m}$ and $600 \mu\text{m}$. The fraction of the alginate beads larger than 1 mm was less than 1% by number, but these large particles constituted $\sim 4\%$ of alginate volume. The droplet formation frequency, as estimated from the number of collected alginate beads, was 9.3 ± 1.4 droplets per minute.

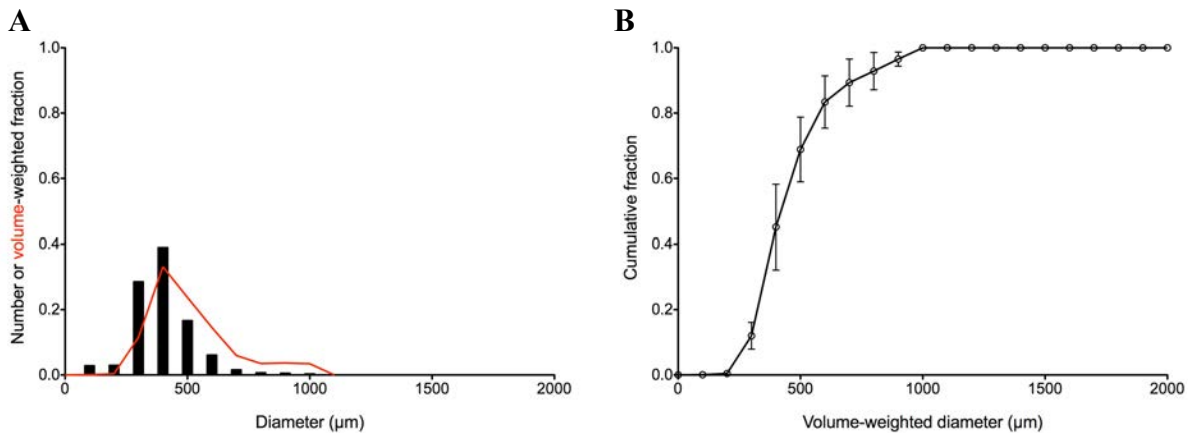


Figure 3.1. Particle size distributions of alginate beads generated in microfluidic devices.

(A) Histograms of the pooled number-weighted alginate bead size distribution and pooled volume-weighted alginate bead size distribution. (B) Cumulative volume-weighted alginate bead size distribution.

Polydispersity, expressed as the coefficient of variation of the volume-weighted distribution of the generated alginate droplets, was ~ 10 -times larger (26.7 ± 3.8) than what is usually achieved with a microfluidic device operating in the dripping regime. Furthermore, D[2,0] did not agree with the predicted droplet diameters estimated in Section 3.1.1. However, studies have revealed that droplet formation occurs due to a complex mixture of viscous drag effects, capillary instabilities and end-pinching mechanisms that cannot be fully described by the proposed equations (Zhou *et al.* 2006). Still, it is important to note that the theoretical droplet sizes were calculated using the injection flow of the alginate mixture. A better estimate of the alginate flow rate during operation could have been obtained from Equation 3-9 (Ward *et al.* 2005), where f stands for the droplet formation frequency, s is the spacing between droplets and U_d is the droplet velocity. However, the lack of a high-speed microscope camera impeded data collection for estimating s or U_d . Instead, Berthier *et al.* have proposed Equation 3-10 for verifying the flow rate of the disperse phase with only the number of droplets detached per unit time (N) and the volume of each droplet measured by image analysis (V_a) (Berthier *et al.* 2010).

$$f \cdot s = U_d \quad \text{Equation 3-9}$$

$$Q_d = N \cdot V_a \quad \text{Equation 3-10}$$

The droplet formation frequency estimated from the number of collected alginate beads and the volume of an equivalent sphere with diameter equal to D[2,0] were used as the values for N and V_a in Equation 3-10. The revised values for Q_d and Re_d were 0.3 mL/min and $2.8 \cdot 10^{-3}$, while the recalculated droplet size from Equation 3-6 was 310 μm , which is closer to D[2,0]. The mode of the generated alginate beads (between 300 μm and 500 μm) approached the dimensions of the orifice ($w_o = 400 \mu\text{m}$ and $h = 480 \mu\text{m}$), suggesting droplet formation might

have transpired in the squeezing regime described by Garstecki *et al.*, which is characterized by yielding monodisperse droplets equal or larger in size to the dimensions of the orifice (Garstecki *et al.* 2005). Equation 3-11 was used for approximating droplet diameter in the squeezing regime as function of the hydraulic diameter of the orifice (D_o) (W. Lee *et al.* 2009), resulting in a predicted droplet size of 991 μm .

$$\frac{d}{D_o} = Ca^{-1/3} \quad \text{Equation 3-11}$$

The theoretical droplet sizes from the squeezing and droplet regimes offer a range that approximates the number-weighted distribution of the generated alginate beads (Figure 3.1). The slight discrepancy between theoretical and experimental results could be partly explained by alginate swelling after cross-linking (Lee *et al.* 2000). Additionally, Lee *et al.* showed that the squeezing and the dripping regimes are separated by a thread formation regime, which is characterized by forming primary droplets that pull a thin thread of disperse phase that breaks into smaller droplets (W. Lee *et al.* 2009). Squeezing involves obstruction of the orifice with a concomitant increase in pressure applied by the syringe pumps actuating the system (Garstecki *et al.* 2005). This sudden increase in pressure might have caused shear thinning in the alginate mixture, resulting in a higher flow rate than either the injection of flow or the revised flow from Equation 3-10, thus changing λ and ϕ . Furthermore, the increase in pressure might have also lead to an increase in the continuous phase flow rate and concomitant increase in Ca , thus explaining the transition to thread formation and dripping. Assuming that droplet formation transitioned from squeezing early on to a transient thread formation regime and then dripping throughout the remainder of operation might help in reconciling the theoretical droplet sizes with the experimental observations, thus implying that a 5-min long equilibration was not long

enough in the studied system. Furthermore, the observed polydispersity could have arisen from droplet coalescence prior to cross-linking (see Figure 3.2). This explanation seems plausible, as some of the generated alginate beads were larger than the dimensions of the microfluidic channels suggesting that alginate droplets coalesced in sections A and B of the downstream channels (see Figure 2.1), or in the collection vessel. Unfortunately, the lack of a high-speed microscope camera to capture droplet formation and on-chip transit impeded the confirmation of droplet formation under a mixed mechanism and/or alginate droplet coalescence as being responsible for the observed polydispersity.

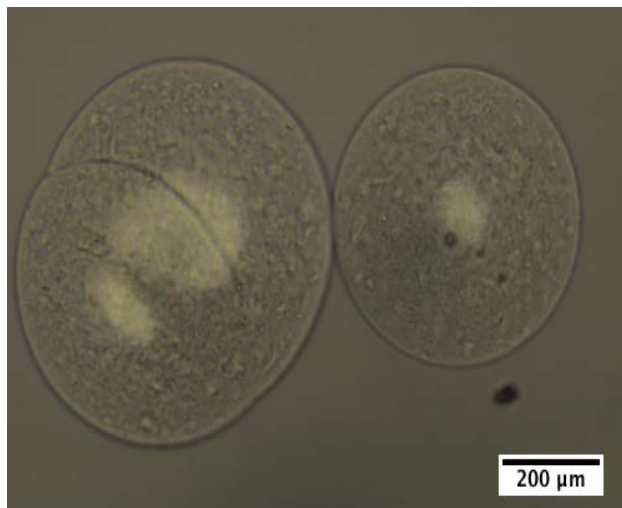


Figure 3.2. Micrograph of alginate beads generated with microfluidic devices.

The bead on the right resembles the majority of the alginate beads produced ($d \approx 300 \mu\text{m}$), while the bead on the left is the product of the fusion of two typical beads that coalesced prior to gelation either while transiting in the outlet channels or in the collection vessel.

3.1.3 Cell viability during processing

In an encapsulation experiment, MIN6 cell viability decreased from 94% to 68% as a function of processing time (Figure 3.3). The processing time was long due to the low droplet formation frequency (see section 3.1.2), resulting in a long residence time of the encapsulated cells inside of the syringe where the supply of nutrients, especially oxygen, might be limited.

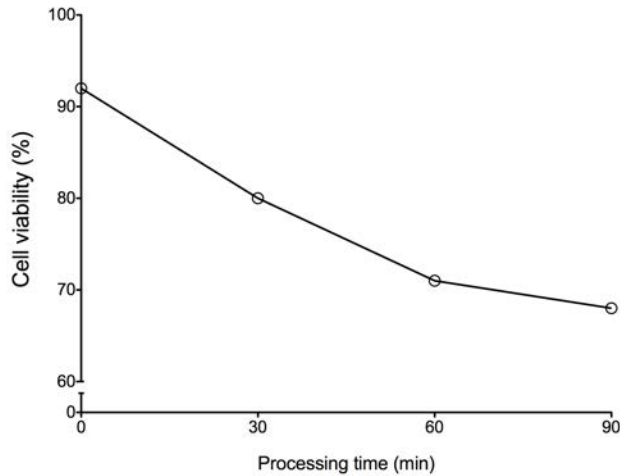


Figure 3.3. Effect of processing time on cell viability during microfluidic device operation.

Cross-linked alginate beads were collected every 30 min. Half of the sample volume was used for viability analysis, while the remainder was pooled for size distribution analysis.

Alginate droplet formation studies in microfluidic devices with similar geometries have revealed that the droplet formation frequency decreases as alginate viscosity increases. The authors also observed droplet formation frequencies ≤ 10 droplets per minute when using alginate solutions with an $\mu_d \approx 2.7 \text{ Pa}\cdot\text{s}$ ($\lambda \approx 80$) (Berthier *et al.* 2010). With the current throughput, it would take more than 20 h to produce enough alginate beads for one mouse transplant. Although increasing the injection flow rates of both phases could certainly increase throughput, the device connections and the seal between the PDMS layers are not strong enough to withstand the high pressures incurred while operating at higher flow rates; moreover, such increase could change the balance of interfacial, viscous and inertial forces (*i.e.*, higher Ca , Re and We numbers), resulting in a different mechanism for droplet formation. Instead of a simple increase in the injection flow rates, the throughput could be increased by running various microfluidic devices in parallel or by integrating a series of droplet generators into a fluidic circuit with dividing manifolds for each injected fluid. These approaches have yet to be tested with highly viscous fluids, and their implementation for encapsulation with alginate should

address concerns such as the increased pumping requirements, connections and seals resistant to the concomitant high pressure, appropriate inlet manifold design to ensure flow distribution while minimizing shear thinning of the alginate phase, as well as independent outlets to reduce the occurrence of droplet coalescence.

Alternatively, replacing the disperse phase with a less viscous alginate solution could serve as a more immediate solution for producing more alginate beads per minute and reducing the residence time of the cells inside of the syringe. The most direct approach to reduce the viscosity of an alginate solution is by decreasing the alginate concentration, however this strategy would most likely result in larger pores allowing the diffusion of antibodies and other smaller components of the immune system *in vivo*, compromising the immunoprotection offered by the alginate capsule. Reducing the molecular weight of the alginate polymer chains could also decrease the final viscosity of the alginate solution. This approach would require procuring and characterizing the alginate from a single algal source, because most commercial alginates are a mixture of gums extracted from different algae with varying molecular weight, and then the development of a polymer degradation and purification method that yields alginate chains with relatively uniform molecular weight. However, such approach is beyond the scope of the current project.

3.2 3D-printed droplet generators

3.2.1 Assessment of needle alignment

3.2.1.1 Precision of needle alignment measurements

The misalignment in a device with design 1 (see Table 2.1), referred to as “device 1-1” (numbering: design and replicate number, respectively), was measured three times to assess precision. The X-ray scans were performed on different days, and the device was removed from the sample holder between scans.

Cross-sectional views of the reconstructed volumes (Figure 3.4A) were analyzed as described in Section 2.4.2.1, resulting in a measure of misalignment between the needle and the outer channel structure defined as concentricity error, which was calculated as the hypotenuse of the absolute difference in the X and Y coordinates of the centers of mass of both objects throughout the Z-axis (Figure 3.4B). The device was not perfectly aligned with the axis of rotation of the sample holder during the scans (Figure 3.4C), but the latter did not affect the tracing of the center of mass of either the needle or the outer channel structure during analysis.

The concentricity error measurements remained approximately constant throughout the longitude (Z-axis) of the analyzed reconstructions, and passed a D’Agostino & Pearson omnibus K2 normality test. Therefore, for each scan, the arithmetic means of the concentricity error were calculated and compared using their 95% confidence intervals (95% CI). The mean concentricity error for the first scan was $6.42 \cdot 10^{-2}$ mm (95% CI: $6.33 \cdot 10^{-2}$ to $6.52 \cdot 10^{-2}$ mm). The second scan had a mean concentricity error of $6.49 \cdot 10^{-2}$ mm (95% CI: $6.45 \cdot 10^{-2}$ to $6.55 \cdot 10^{-2}$ mm). And, the mean concentricity error in the third scan was $6.66 \cdot 10^{-2}$ mm (95% CI: $6.59 \cdot 10^{-2}$ to $6.73 \cdot 10^{-2}$ mm). The 95% CI of the third scan did not overlap with the 95% CI of the first and second scans; however, when fitting horizontal lines to the concentricity error estimates of each scan, the

differences between the best-fit values, obtained through least squares fitting, differ by approximately one-tenth of the CT scanner resolution. These results support the conclusion that the measurements are highly reproducible between scans, and that variations in the placement of the device inside the sample holder between scans had no practical effect.

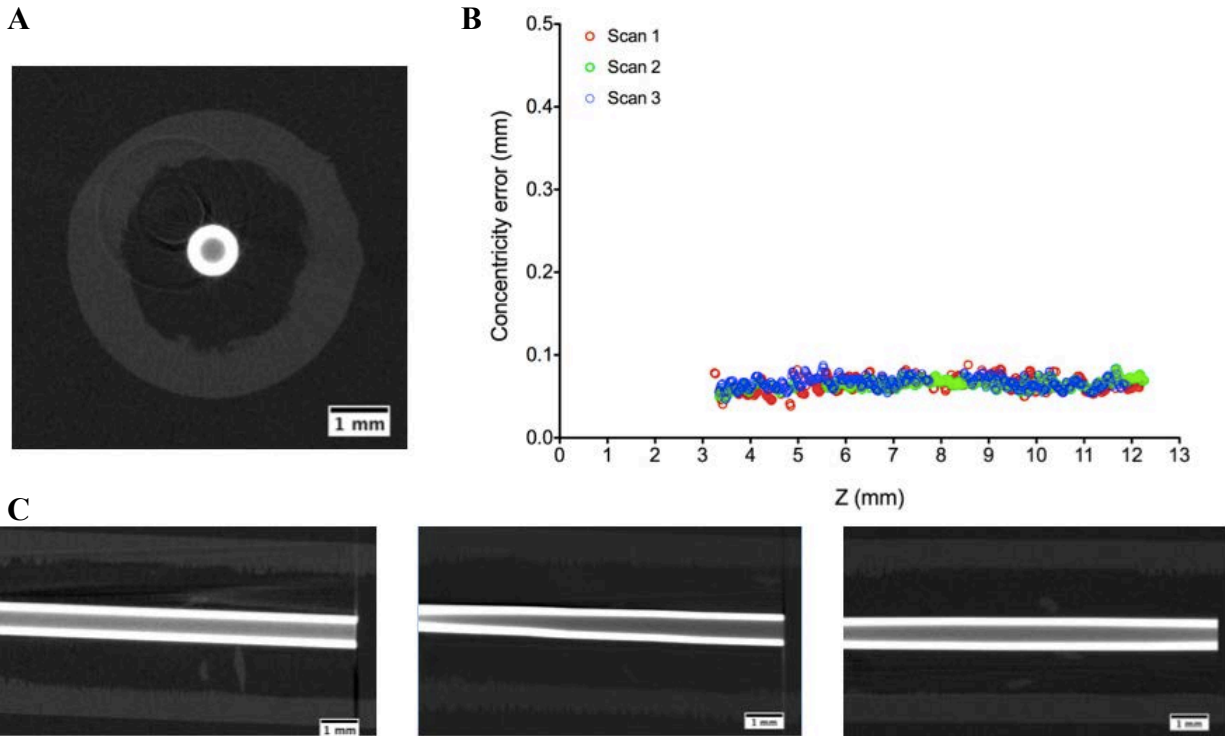


Figure 3.4. Evaluating the precision of CT scans.

(A) Representative cross-sectional view of concentric cylinder configuration in device 1-1. (B) Concentricity error calculated from cross-sectional views displaying concentric cylinder configuration after segmentation through image analysis. (C) Orthogonal views of three separate scans of the concentric cylinder configuration in device 1-1.

3.2.1.2 Alignment errors in 3D-printed droplet generators

Three devices of each design (see Table 2.1) were scanned and analyzed. Figure 3.5 shows the concentricity error measurements smoothed using the 20-nearest neighbors for locally

weighted scatterplot smoothing (LOWESS). The concentricity error measurements displayed two characteristic behaviors: in the majority of the scanned devices, the concentricity error increased as a function of the distance from the needle port (located at $Z = 0$ mm); while in device 3-3 (blue line in Figure 3.5C), as seen during the triplicate scans of device 1-1 (see Figure 3.4), the distance between the needle and the outer channel remained approximately constant onwards from $Z = 5$ mm.

Interestingly, besides device 3-3, devices 2-1 and 4-1 displayed a decrease in concentricity error between $Z = 4$ and 5 mm (red lines in panels B & D of Figure 3.5). Inspection of those cross-sectional views revealed that the stem from the hose-barb connectors appeared in them, and the segmentation algorithm was identifying the stems as part of the outer cylinder structure yielding oval-shaped binary masks with displaced coordinates of the centers of mass.

Adjustments of the circularity threshold during image analysis compromised the quality of the concentricity error measurements as it resulted in too few cross-sectional views displaying the concentric cylinder configuration. Therefore, only the concentricity error measurements for lengths of $Z \geq 5$ mm were considered for further analysis.

To confirm the observations on the behavior of the concentricity error, a best-fit regression analysis was run on a subset of the measurements ($Z \geq 5$ mm) for all devices. The best-fit line was chosen with Akaike's informative criteria comparison, using horizontal lines and lines through origin with range $Z = 0$ to 13 mm as possible models. The preferred model, *i.e.*, the model more likely to have generated the data, for each device was plotted with the LOWESS curves (dashed lines in Figure 3.5). The results from the best-fit regression analysis agreed with the aforementioned behaviors of the concentricity error in all devices except for device 1-2, where the preferred model was a horizontal line. However, the corresponding LOWESS curve

resembles an asymmetric parabola (green line in Figure 3.5A), suggesting either oval-shaped binary masks due to the presence of stems at $Z = 6$ mm, or a bent needle.

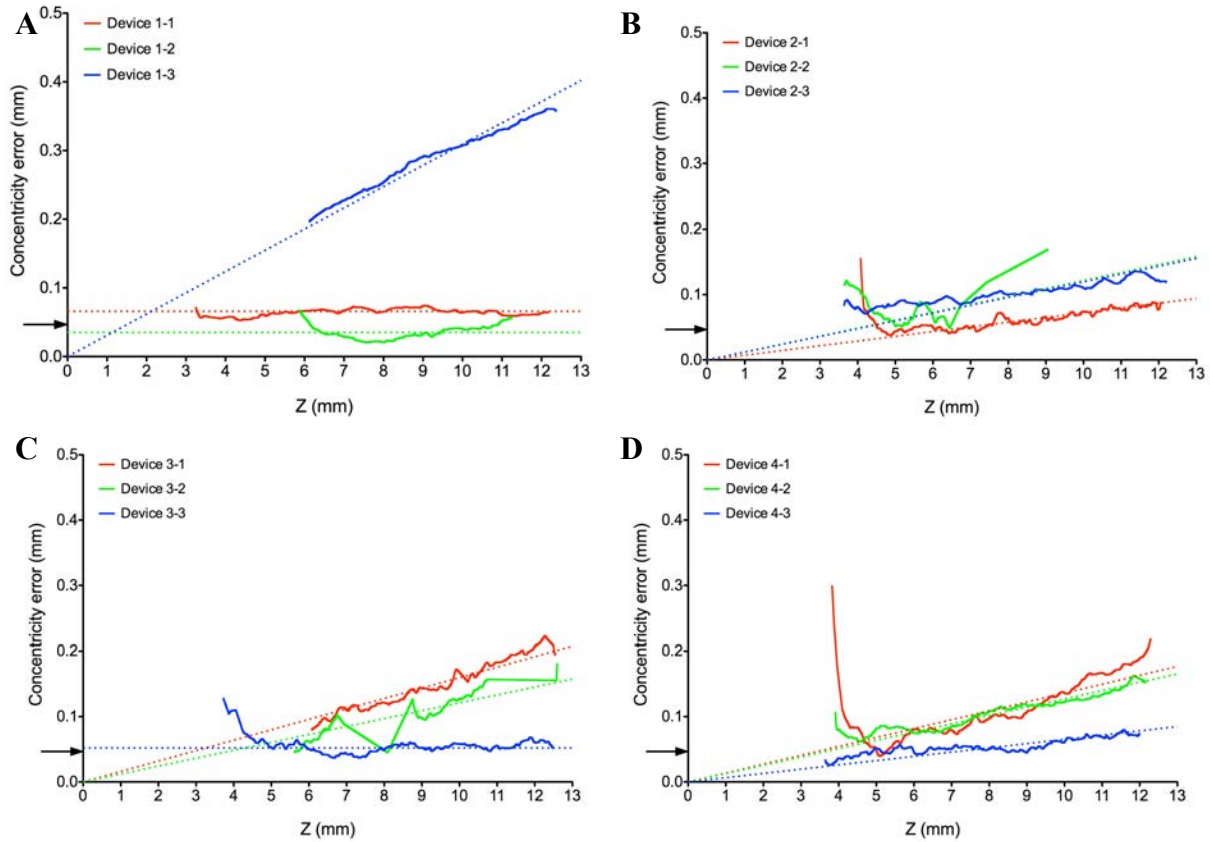


Figure 3.5. Concentricity error in 3D-printed droplet generators.

LOWESS curves of the concentricity error (solid lines) and best-fit regression lines (dashed lines) estimating either offset or misalignment between outer cylinder and needle. Arrows in the Y-axis shows the approximate accuracy of the 3D printer. (A) Devices with design 1. (B) Devices with design 2. (C) Devices with design 3. (D) Devices with design 4.

In 10 of the fabricated devices (or 9, according to the best-fit regression analysis) where the concentricity error increased as a function of Z, it is clear that the needle was angled relative to the outer cylinder. These “angled needles” most likely arose because the needle ports served

as pivots and the tips of needles were able to move during alignment, especially before the epoxy glue anchored the needle hub to the top outer channel structure.

As for the devices with constant concentricity errors, it is clear that the needles were perpendicularly aligned with the outer channel structure, but not truly concentric because of the offset between the centers of mass. These “offset needles” are harder to explain considering that needle ports were designed for a snug fit according to the gage of the needle; however, the offsetting might have occurred due to the 3D printer (accuracy $\sim 50 \mu\text{m}$) fabricating needle ports with larger dimensions.

In addition to the aforementioned possible causes, the clearance ($\sim 50 \mu\text{m}$ for Designs 1 & 2, and $\leq 20 \mu\text{m}$ for Designs 3 & 4) between the inner diameter of the anchored needle and outer diameter of the needle used during alignment (see section 2.4.2) might have also contributed to either type of needle alignment error.

3.2.1.3 Effects of alignment errors on device performance

Following the assessment of needle alignment, devices were classified according to their type of needle alignment error (Table 3.1), and used for generating empty alginate beads to study the effect of needle alignment error on device performance. Alginate beads were generated at three different outer flow rates (30, 40 & 50 mL/min), and the interquartile range (IQR) of the number- and volume-weighted alginate bead size distributions were used as measures of performance (Figure 3.6). Device 1-2 had a leak in the needle port, thus it did not generate alginate beads and was excluded from further analyses.

Table 3.1. Classification of tested devices based on needle alignment error.

	Type of alignment error	Minimum concentricity error (mm)	Maximum concentricity error (mm)	Angle of misalignment (degrees)	Offset (mm)
Device 1-1	Offset	0.039	0.088	-	0.066
Device 1-3	Angled	0.194	0.367	1.770	-
Device 2-1	Angled	0.003	0.202	0.415	-
Device 2-2	Angled	0.010	0.169	0.699	-
Device 2-3	Angled	0.029	0.149	0.688	-
Device 3-1	Angled	0.076	0.237	0.917	-
Device 3-2	Angled	0.037	0.179	0.693	-
Device 3-3	Offset	0.006	0.145	-	0.052
Device 4-1	Angled	0.011	0.326	0.779	-
Device 4-2	Angled	0.034	0.183	0.728	-
Device 4-3	Angled	0.005	0.119	0.374	-

Angle of misalignment and offset were calculated using the best-fit regression lines. Minimum and maximum concentricity error were obtained from truncated range of measurements ($Z \geq 5$ mm).

The number-weighted IQR in devices with offset needles (range: 250 – 380 μm) were narrower than in devices with angled needles (range: 140 – 370 μm). Similarly, volume-weighted IQR were also narrower in devices with offset needles (60 – 309 μm) when compared to devices with angled needles (40 – 470 μm). However, the mean of the number-weighted IQR was lower in devices with angled needles (325 vs. 250 μm), while the means of volume-weighted IQR were relatively similar for devices with either type of misalignment error (average IQR for devices with angled needles = 190 μm ; average IQR for devices with offset needles = 180 μm).

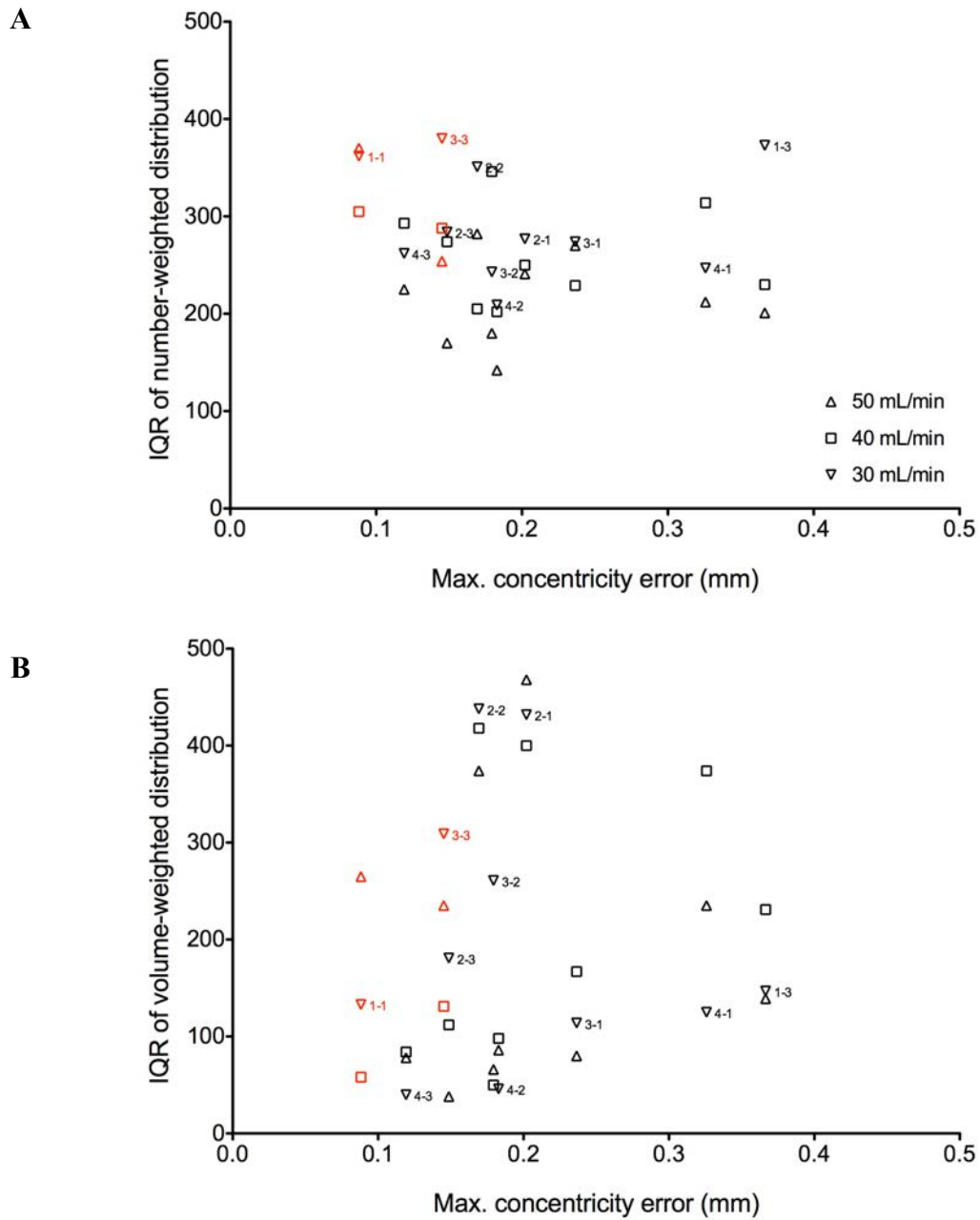


Figure 3.6. Correlation between alignment error and polydispersity.

Scatterplots were used to screen correlation between polydispersity, represented by the interquartile ranges (IQR) of the number (A) and volume-weighted distributions (B), and alignment error. Maximum concentricity error was used to account for alignment error in devices with angled needles (in black) and devices with offset needles (in red).

Panel B of Figure 3.6 displays an ostensible positive correlation between maximum concentricity error and IQR. Spearman correlation followed by hypothesis testing was applied to the entire scattergram, pooling regardless of type of alignment error and outer flow rate. The resulting Spearman correlation coefficient (r_s) was 0.3 but not statistically significant (95% CI: -0.383 to 0.771, two-tailed p-value = 0.371). The aforementioned analysis was repeated for the number-weighted IQR, also resulting in a non-statistically significant r_s of -0.369 (95% CI: -0.8 to 0.315, two-tailed p-value = 0.261). Interestingly, when analyzing the number-weighted IQR at each flow rate and testing their correlation with maximum concentricity error (see appendix B.3), r_s decreased as outer flow rate increased; conversely, the r_s of the volume-weighted IQR did not show this behavior. Finally, the analysis was repeated only for devices with angled needles, maximum concentricity error was replaced for angle of misalignment, and the correlation with the number- and volume-weighted IQR were assessed with and without pooling for outer flow rate. The pooled r_s were 0.259 (two-tailed p-value = 0.493) for the number-weighted IQR, and 0.167 (two-tailed p-value = 0.678) for the volume-weighted IQR. The r_s at each flow rate did not show any particular behavior for either the number- or volume-weighter IQR.

The observed correlations between the maximum concentricity error and the number- or volume-weighted IQR might have occurred due to chance, thus suggesting that generating alginate beads in devices with either type of alignment errors might not substantially increase polydispersity of the alginate beads generated with them. This conclusion seems to hold especially for devices with misaligned needles, as the misalignment angle of 2°, or the next largest angles, did not translate into wider IQR. As for devices with offset needles, the sample size was too small to test for correlations and the range of measured offsets is too narrow; still, neither IQR increased concomitantly with the magnitude of this type of alignment error.

3.2.2 Design geometry, outer flow rate and particle size distribution

The 3D-printed droplet generators possessed four different geometries and were exposed to three pre-specified outer flow rate operating conditions. Thus, the following descriptive statistics were chosen to assess the effect of these two factors on the resulting alginate bead batches: the number area mean diameter ($D[2,0]$), the volume moment mean diameter ($D[4,3]$), the interquartile ranges of the number-weighted distribution ($IQR_{2,0}$), and of the volume-weighted distribution ($IQR_{4,3}$). Also of interest were the effects of the factors on droplet formation production frequency as estimated during collection.

In Figure 3.7, the horizontal bars were used to roughly estimate grand means grouped by each factor. For the $D[2,0]$ in panel A, grand means by outer flow rate did not seem to differ substantially, but grand means of designs 1 and 4 sat on opposite sides of the distribution, where their ranges might not have overlapped. In panel B, grand means of $D[4,3]$ decreased as outer flow rate increased, but remained more or less equal across design geometries. Similarly, grand means for both IQR did not differ substantially, except for design 2 in panel D. Finally, grand means of frequency (Figure 3.7E) for the two higher flow rates seemed higher than for 30 mL/min, also the grand means for designs 1 and 4 sat again at opposite sides of the distribution.

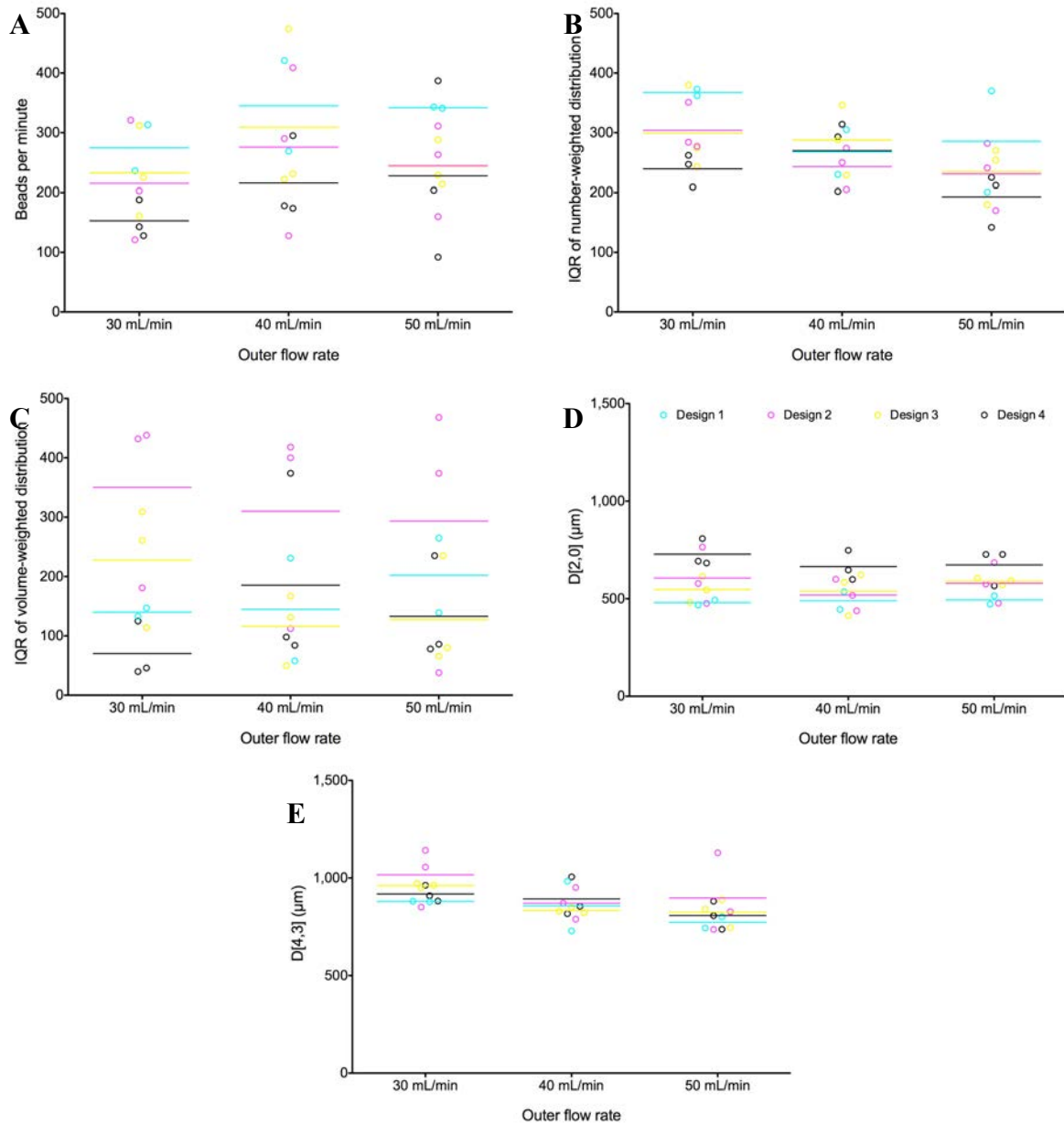


Figure 3.7. Effects of outer flow rate and design geometry on select descriptive statistics of alginate particle size distributions.

Scatter dot plots were used to represent all select descriptive statistic (A – D) and frequency (E) of each replicate grouped by outer flow, horizontal lines correspond to cell average (*i.e.*, mean of *i*-th design at *j*-th outer flow rate).

(A) number area mean diameter, $D[2,0]$; (B) volume moment mean diameter, $D[4,3]$; (C) interquartile ranges of the number-weighted distribution, $IQR_{2,0}$; (D) volume-weighted distribution, $IQR_{4,3}$.

Analysis of variance (ANOVA) offers a more rigorous and formal analysis than comparing grand means pooled by factors. However, for the data in question, the low and uneven number of replicates in each cell hampered fulfillment of normality and homogeneity assumptions. The Friedman test is a commonplace alternative to one-way ANOVA for nonparametric data; furthermore, independent Friedman tests on each factor have been used to replace two-way ANOVA (*e.g.*, (Findlater *et al.* 2009)). However, Friedman tests are limited to balanced designs, thus requiring data truncation for complete case analysis or data imputation, which is beyond the scope of this project. As an alternative, the two-test approach was run on the 54 data sets resulting from complete case analysis (for more details on methodology see appendix A.4). Test statistics were summarized (see appendix C.1), and indicated that increasing the outer flow rate resulted in a statistically significant change ($\chi^2_{2,8}$ range: 7.750 – 12.250, p-value range: 0.002 – 0.021) in D[4,3]. For the remainder of the select descriptive statistics and the frequency, changes in the outer flow rate did not result in statistically significant differences; although some of them had relatively low mean and median p-values their ranges extended over the 0.05 significance threshold. The differences in design geometry did not translate into statistically significant differences for any of the studied variables. However, the employed approach might not be fully appropriate because it ignores interactions between factors as it implies data transformation by row ranking (*i.e.*, by outer flow rate) in both Friedman tests. Therefore, no post-hoc analyses were performed.

For the data in question, one of the factors varied between groups (*i.e.*, the different geometries in each design), while 11 devices (two or three devices of each geometry) were exposed to the same three levels of flow rate (*i.e.*, this factor varied within groups). This case corresponds to a two-way ANOVA with repeated measures on one factor, also known as a split-

plot two-way ANOVA or, more generally, as mixed ANOVA. Unfortunately, there is no robust nonparametric test equivalent to mixed ANOVA. From the wide variety of data transformations suggested for these situations, the simple ranked transform by columns (*i.e.*, across design geometries) proposed by Conover & Iman (Conover & Iman 1981) was applied to the data and satisfied ANOVA assumptions, then mixed ANOVA assuming possible interactions was run (see appendix A.4). These results also indicated that increasing the outer flow rate rendered statistically significant differences in $D[4,3]$ ($F_{2,14}$: 10.999, p-value: 0.001) and $IQR_{4,3}$ ($F_{2,14}$: 10.999, p-value: 0.001), but not in $D[2,0]$, $IQR_{2,0}$ or frequency (see appendix C.2). Conversely, design geometry and interaction between the factors did not induce statistically significant differences in any of the dependent variables (see appendix C.2). Nevertheless, further research revealed that the simple rank transform by columns is not recommended for ANOVA designs with two or more factors because it systematically undervalues interactions, while attributing a higher proportion of the variance to the main effects (Fawcett & Salter 1984). Therefore, no post-hoc analyses were performed.

Salter and Fawcett proposed the aligned ranked transform (ART) as an alternative method to analyze nonparametric data through ANOVA with interactions (Salter & Fawcett 1993) and/or incomplete balanced designs (Salter & Fawcett 1985), the method was expanded by Higgins *et al.* (Higgins *et al.* 1990; Higgins & Tashtoush 1994), and has been found capable of handling almost any ANOVA design (Wobbrock *et al.* 2011). The transformation consists in isolating the effect of every factor (k : number of factors) and possible interactions through data alignment, ranking each aligned response ($k + 2^k - 1$: number of aligned responses), performing a full independent ANOVA using one ranked-aligned response at a time, extracting from them the information corresponding to the effect for which the response was aligned, and repeating the

process for the remainder of ranked-aligned responses. The process of data alignment involves the calculation of cell means, *i.e.*, pooled means at every level of the factors; followed by residual computation, which consists in subtraction between the original response variable and the corresponding cell mean; then marginal means are calculated, *i.e.*, level-specific means subtracted from the grand pooled mean, in order to estimate the effect of every factor and interaction; then, aligned responses are obtained for every factor by summing each residual with a corresponding marginal mean; finally, the aligned responses are ranked. The correctness of the transformation can be confirmed after calculation of the aligned responses, which should sum to zero, or by performing ANOVAs on the aligned responses, whose resulting F values should be close to zero. Results of the combination of ART algorithm with mixed ANOVA (see appendix C.3) indicated that changes in outer flow rate resulted in statistically significant differences in D[4,3] ($F_{2,14}$: 9.553, p-value: 0.002), confirming the results from the previous analyses in spite of them being less appropriate. Additionally, changes in outer flow rate also caused statistically significant differences in IQR_{2,0} ($F_{2,14}$: 3.832, p-value: 0.047). No statistically significant differences were observed for IQR_{4,3} and frequency, but changes in design geometry resulted in substantial differences in D_{2,0} ($F_{3,7}$: 4.052, p-value: 0.058). For further analysis, contrasts (Tukey's honest significance difference test) were performed on D[4,3] & IQR_{2,0} over flow, and D[2,0] over design geometry. Results indicated that changing the outer flow rate from 30 mL/min to 40 or 50 mL/min occasioned statistically significant differences on D[4,3], but increases in outer flow rate from 40 to 50 mL/min did not. Similarly, for IQR_{2,0}, increases in the outer flow rate from 30 to 50 mL/min also resulted in statistically significant differences. While for D[2,0], only the geometry changes between designs 1 and 4 resulted in statistically significant differences.

3.2.2.1 Dimensionless numbers

The capillary number was estimated using its general definition (Equation 3-12), while the Re and We numbers were calculated using Equation 3-3 and Equation 3-5, respectively (see section 3.1.1).

$$Ca = \frac{\mu_c U_c}{\sigma} \quad \text{Equation 3-12}$$

The ratio of volumetric flow rate, assuming injection flow, was between 150 and 250, while the viscosity ratio was 126.5. The range of Ca was 1.1 to $2.8 \cdot 10^{-1}$; greater values corresponded with higher outer flow rates and larger blunt needles. The maximum Re_c was $1.8 \cdot 10^1$, corresponding to outer flow rates of 50 mL/min in devices with 18G blunt needles, while the Re_d number was $1.5 \cdot 10^{-3}$ in 18G needles and $2.4 \cdot 10^{-3}$ for devices with 21G needles. Finally, while calculating the We , the diameter of the blunt needle was used for w_o in Equation 3-5, resulting in values of $5.9 \cdot 10^{-1}$ for 21G needles, and $9.7 \cdot 10^{-1}$ for 18G needles. Overall, the values of the dimensionless number indicate that operating parameters ensured laminar flow, and that interfacial tension dominated over viscous and inertial forces.

Umbanhowar *et al.* (Umbanhowar *et al.* 2000) proposed the first set of scaling rules for predicting droplet size generated in co-flowing streams expressed in terms of the ratio between droplet diameter (d) and inner channel diameter (d_i) (Equation 3-15). Equation 3-13 resulted from a force balance of surface tension and viscous drag acting on the growing droplet, and can be reduced to Equation 3-14 when the inner flow rate is small in comparison to the outer flow rate.

$$\bar{d}^3 - \left(1 + \frac{1}{3Ca}\right) \bar{d}^2 - \frac{\phi}{\alpha} \bar{d} + \frac{\phi}{\alpha} = 0 \quad \text{Equation 3-13}$$

$$\bar{d} \approx 1 + \frac{1}{3Ca} \quad \text{Equation 3-14}$$

$$\bar{d} = \frac{d}{D_i} \quad \text{Equation 3-15}$$

The droplet size estimation proposed by Equation 3-14 seemed appropriate when considering the flow rates used during alginate droplet formation, and was confirmed by the agreement when compared with the droplet size estimates obtained from Equation 3-13 (Table 3.2). However, the theoretical alginate droplet sizes are larger than the experimental results, and even larger than the dimensions of the outlet channel. The divergence between experimental and theoretical results might be explained by the differences in the geometries of the devices used for deriving and validating the scaling rules. In (Umbanhowar *et al.* 2000), the authors injected the disperse phase through a capillary glass tube ($D_i < 100 \mu\text{m}$) immersed in a rotating cup containing the continuous phase; besides the obvious differences in the dimensions of the inner channels used for the injection of the disperse phase, the most striking difference is the confinement of the continuous phase in the devices employed during this study. Essentially, all the devices in this study had the oil phase co-flowing through a 3-mm cylindrical channel, and then passing through an orifice 0.7 to 1 mm in diameter. Therefore, this set of scaling rules might not be appropriate for reconciliation with experimental results.

Table 3.2. Alginate droplet size estimates for co-flowing stream geometry.

Needle gauge	Outer flow rate	Equation 3-13	Equation 3-14
21 (510 μm) (Designs 1 & 2)	30	2,144	2,135
	40	1,741	1,730
	50	1,493	1,487
18 (840 μm) (Designs 3 & 4)	30	2,502	2,501
	40	2,090	2,085
	50	1,838	1,835

Outer flow rate in mL/min. Droplet size estimates from equations in μm .

Alternatively, Takeuchi *et al.* proposed scaling rules for three-dimensional cylindrical devices fabricated in PDMS (Takeuchi *et al.* 2005) and through stereolithography (Morimoto *et al.* 2009). The authors denominate their devices as axisymmetric flow-focusing devices, fundamentally because these confine the emerging interface through orifices after the junction of the inner and outer cylindrical channels. The authors propose rewriting the capillary number as Equation 3-16, where the radius of the inner jet stream (R_j) can be estimated as function of the flow ratio and the cross-sectional area of the orifice. The radius of the generated droplets (R_d) can then be estimated based on the interval between droplets (ι), which can be expressed either as a function of droplet volume and cross-sectional area of the inner jet stream (Equation 3-18), or a function of droplet radius and the viscosity ratio (Equation 3-19). The combination of these equations yields Equation 3-20, which is only valid for the dripping regime when droplets are produced at equal intervals.

$$Ca = \frac{\mu_c Q_d}{\pi \sigma R_j^2} \quad \text{Equation 3-16}$$

$$R_j^2 = \frac{R_o^2}{\phi^{-1} + 1} \quad \text{Equation 3-17}$$

$$\iota = \frac{4R_d^3}{3R_j^2} \quad \text{Equation 3-18}$$

$$\iota = \lambda R_d \quad \text{Equation 3-19}$$

$$R_d = \left\{ \frac{3\lambda}{4} \cdot \frac{R_o^2}{\phi^{-1} + 1} \right\}^{\frac{1}{2}} \quad \text{Equation 3-20}$$

The geometry of Takeuchi's devices is comparable to the devices used in this study, and values of D[4,3] for devices with design 4 seem to agree with theoretical estimates (Table 3.3); however, most theoretical estimates still exceeded the dimensions of the outlet channel.

Table 3.3. Alginate droplet size estimates for flow-focusing geometry and experimental results.

Orifice	Outer flow rate	Equation 3-20	D[2,0]			D[4,3]		
1,000 (Designs 1 – 3)	30	1,551	481	606	547	880	1099	961
	40	1,344	491	518	540	857	911	825
	50	1,200	494	579	590	773	978	817
700 (Design 4)	30	1,086	728			936		
	40	941	665			931		
	50	842	673			844		

Outer flow rate in mL/min. Orifice sizes, droplet size estimates, D[2,0] and D[4,3] in μm . Values in D[2,0] and D[4,3] correspond to pooled averages obtained from replicates. Sub-columns in D[2,0] and D[4,3] correspond to designs 1, 2 & 3, respectively.

Theoretical estimates were recalculated using Equation 3-10 to correct the alginate flow rate based on the droplet formation frequency estimated from the collected alginate beads and the volume of an equivalent sphere with diameter equal to D[2,0]. The resulting estimates had a better agreement with experimental values of D[2,0] for devices with designs 1 – 3, and none of the theoretical estimates exceeded outlet channel dimensions.

Table 3.4. Recalculated alginate droplet size estimates for flow-focusing geometry.

Orifice	Outer flow rate	Corrected with Equation 3-10		
1,000 (Designs 1 – 3)	30	439	440	395
	40	551	427	425
	50	491	481	436
700 (Design 4)	30	428		
	40	384		
	50	360		

Theoretical estimates obtained with **Equation 3-20** were recalculated using the disperse flow rate correction proposed by **Equation 3-10**, using corresponding experimental values of $D[2,0]$. Outer flow rate in mL/min. Orifice sizes, droplet size estimates in μm . Sub-columns correspond to designs 1, 2 & 3, respectively.

3.2.3 Effects of surfactant addition on particle size distribution

As discussed in Section 3.1.2, alginate swelling might contribute to the discrepancy between theoretical and experimental results. Additionally, the alginate bead size distributions resulting from all devices turned out more polydisperse than what has been reported with similar devices, *e.g.*, see (Morimoto *et al.* 2009; Sakai *et al.* 2004). However, these occurrences are more likely to have been caused by alginate droplet coalescence. As can be seen in Figure 3.8, the resulting size distributions for most of the devices appear as two distinct lines with different slopes connecting at an inflexion point, which is an indication of the presence of a bimodal distribution. These bimodal distributions of particle size are likely to have occurred due to the generation of satellite droplets. In turn, the presence of these satellite droplets could have also contributed towards obtaining large coefficients of variation. These results support the notion that droplet coalescence was partly responsible for the high levels of polydispersity. Especially when considering that droplet coalescence and generation of satellite droplets might have not been mutually exclusive phenomena.

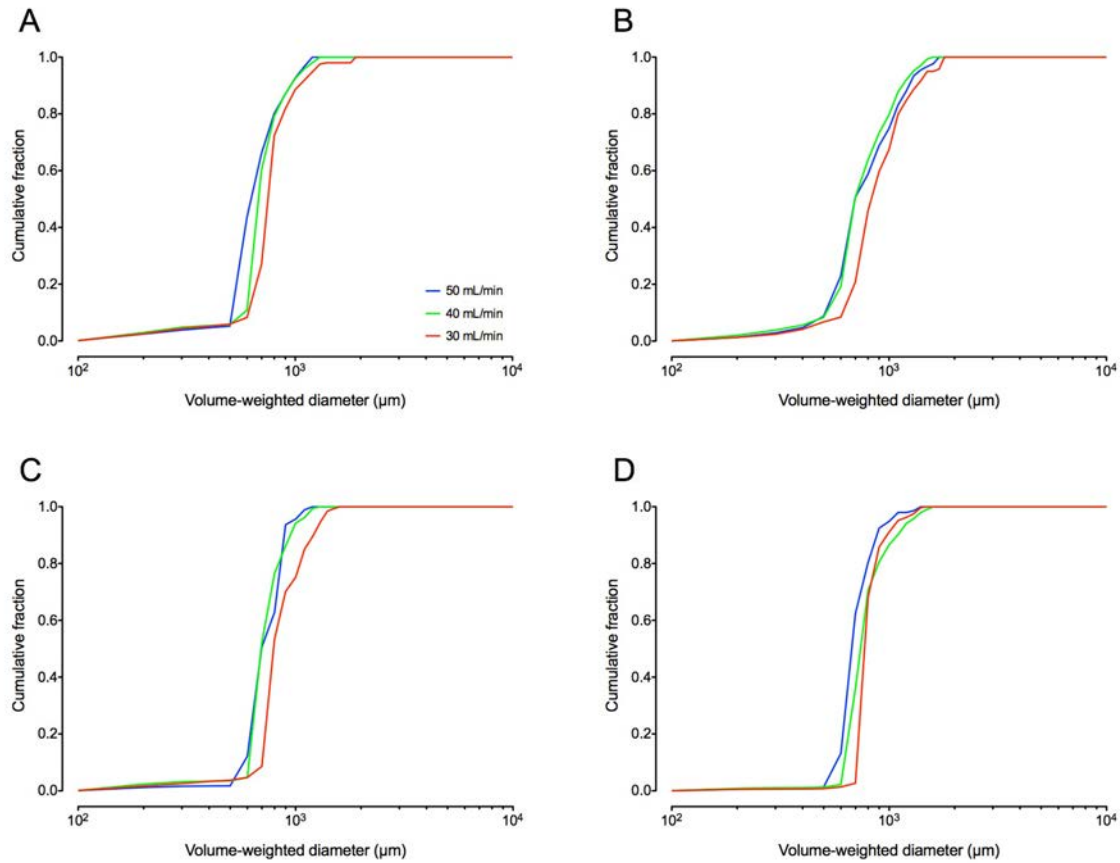


Figure 3.8. Lognormal plot of alginate bead size distributions of 3D-printed droplet generators.

Cumulative size distributions weighted by volume and pooled by outer flow rate ($n = 3$ batches produced in 2 – 3 different devices). (A) Design 1, (B) design 2, (C) design 3 and (D) design 4.

Coalescence of alginate droplets was witnessed during transit to the collection chamber, especially in the second half of the downstream channel, but this phenomenon could not be documented. On the other hand, image analysis suggests the generation of satellite droplets by offering evidence of the presence of alginate beads with about one fifth of the size of the main particles (~ 200 vs. $1,000 \mu\text{m}$) (see Appendix B.2 for size distributions histograms), but the formation of the satellite droplets could not be observed because the 3D-printed devices were opaque.

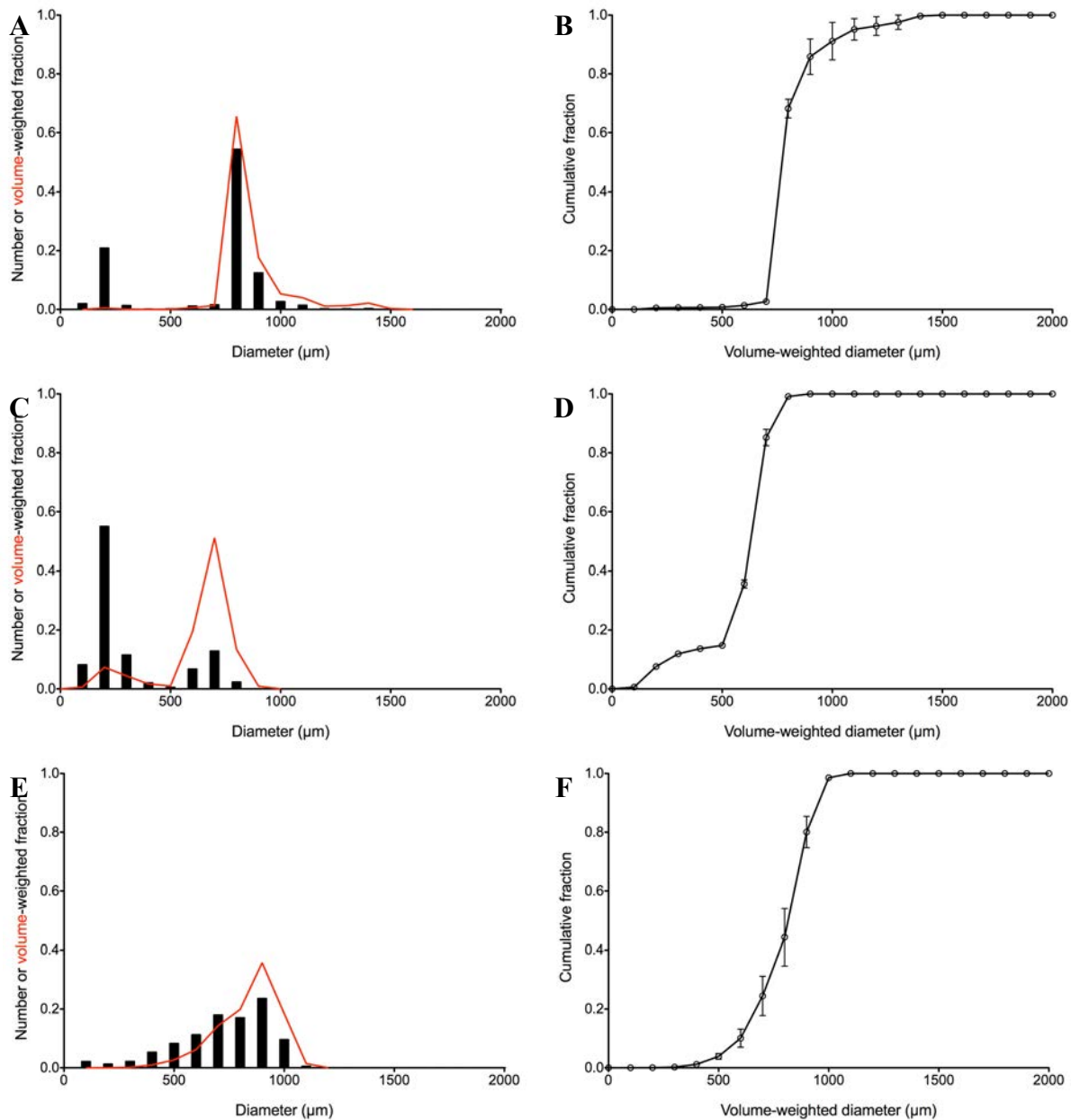


Figure 3.9. Alginate bead size distributions with and without surfactant added to the oil phase.

(A, C & E) Histograms of the pooled ($n = 3$ batches) number-weighted alginate bead size distribution and pooled volume-weighted alginate bead size distributions. (B, D & F) Cumulative volume-weighted alginate bead size distributions. Alginate beads were generated in devices with design 4 at an outer flow rate of 30 mL/min of mineral oil without (A & B) and with surfactants (C – F). The surfactants added to the oil phase were (C & D) 1% w/v Tween 20 and (E & F) 1% w/v Span 80.

Following suggestions from the literature, Span 80 or Tween 20 were added to the oil phase in an attempt to prevent droplet coalescence. In Figure 3.9A, the $D[2,0]$ was $362 \pm 6 \mu\text{m}$, $D[4,3]$ and its coefficient of variation were $680 \pm 2 \mu\text{m}$ and $24.6 \pm 0.7\%$, respectively. Use of Tween 20 resulted in a bimodal distribution that could have arisen due to the generation of 2 – 3 satellite droplets $\sim 200 - 300 \mu\text{m}$ in size per major droplet; otherwise, if coalescence occurred despite the presence of the surfactant, the larger droplets ($\sim 800 - 900 \mu\text{m}$ in size) could have arisen as a byproduct due to the fusion of 3 smaller droplets. Conversely, the use of Span 80 (Figure 3.9B) resulted in a unimodal alginate bead size distribution were $D[2,0]$, $D[4,3]$ and the latter's coefficient of variation were $773 \pm 29 \mu\text{m}$, $889 \pm 26 \mu\text{m}$ and $14.9 \pm 0.9\%$, respectively.

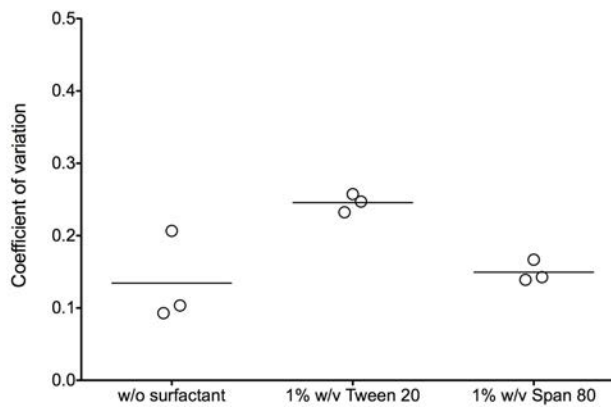


Figure 3.10. Comparing polydispersity of alginate beads generated with or without surfactants.

Three batches of alginate beads were generated on devices with design 4 at 30 mL/min outer flow rate. Coefficients of variation of the volume-weighted size distributions were used as measures of polydispersity.

The coefficient of variation for beads generated without surfactant was $13.4 \pm 3.6\%$. While the use of Tween 20 and Span 80 resulted in average coefficients of variation of $24.6 \pm 0.7\%$ and $14.9 \pm 0.9\%$, respectively. As can be seen in Figure 3.10, addition of surfactants to the oil phase did not seem to improve the performance of devices with design 4 in terms of reducing polydispersity, *i.e.*, the mean coefficient of variation remained at $\sim 15\%$. Surfactant addition did

decrease the variation in the levels of polydispersity, suggesting that droplet coalescence might have been partially prevented, and that other unforeseen events contributed to the observed variability in alginate bead size. Unfortunately, devices were opaque and droplet formation could not be observed, thus it was impossible to confirm if alginate droplet formation transpired solely in the dripping regime.

3.2.4 NPI encapsulation using 3D-printed droplet generators

Devices with design 4 (needle ID: 838 μm) were used for encapsulation experiments because NPI often aggregate into large ($> 500 \mu\text{m}$) clusters (see appendix B.4). Furthermore, in one encapsulation run, addition of 1% w/v Span 80 to the oil phase resulted in the precipitation of the serum proteins present from the cell culture media in the collection bottle, and no alginate beads were recovered. Therefore, subsequent encapsulations were performed without surfactants.

In Figure 3.11, as expected, capsules generated at higher outer flow rates were smaller in terms of $D[2,0]$ and $D[4,3]$. At an outer flow rate of 30 mL/min $D[2,0]$ was $1,016 \pm 58 \mu\text{m}$ for alginate capsules generated at 30 mL/min, while at 40 mL/min, $D[2,0]$ was $894 \pm 128 \mu\text{m}$. Similarly, the $D[4,3]$ were $1,387 \pm 86$ and $1,089 \pm 79 \mu\text{m}$ for outer flow rates of 30 and 40 mL/min, respectively. Coefficients of variation of the volume-weighted distribution were also smaller for outer flow rates of 40 mL/min ($25.6 \pm 3.5\%$ vs. $11.8 \pm 0.9\%$). Alginate capsules containing NPI were larger than empty alginate beads in terms of $D[4,3]$ when the outer flow rate was 30 mL/min, but not significantly different when at outer flow rates of 40 mL/min (Figure 3.12, see figure caption for statistical tests).

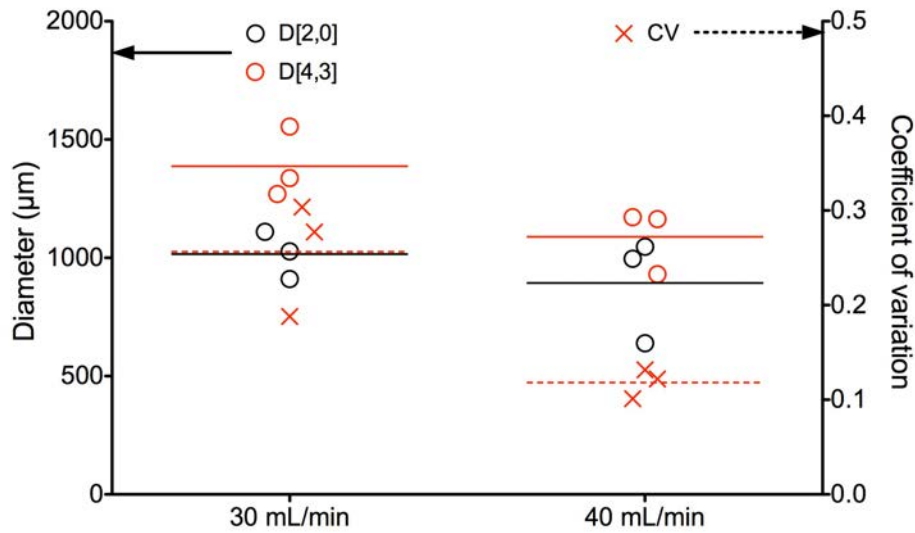


Figure 3.11. Size distributions of alginate capsules containing NPI.

Scatterplot of the number-weighted mean diameter (D[2,0], black circles), volume-weighted mean diameter (D[4,3], red circles), and the coefficient of variation of the volume-weighted distribution (CV, red crosses). The mean values of D[4,3] and D[2,0] are represented by solid lines, while the dashed lines represent the mean value of the coefficient of variation of the volume-weighted distribution. Arrows point to corresponding axes for the size distribution statistic. NPI were encapsulated in alginate beads using devices with design 4 at 30 or 40 mL/min outer flow rate. Coefficients of variation of the volume-weighted size distributions were used as surrogate measures of polydispersity.

In parallel to encapsulation experiments performed with 3D-printed droplet generators, NPI were also encapsulated through emulsification-internal gelation (see appendix B.6 for size distribution of alginate capsules). NPI were recovered from the alginate capsules, dissociated into single cells in order to assess cell viability, and compared to viability before processing (Figure 3.13).

Results indicate that the studied encapsulation processes are not statistically different in terms of their relative viabilities after encapsulation (p -value = 0.561, Kruskal-Wallis statistic =

1.156). And, although all encapsulation processes did have a negative impact in the absolute cell viability, the magnitude of this effect is small and its practical significance is, at best, ostensible because it is not clear if the observed decreases in viability were caused by the encapsulation process, or a systematic factor (*e.g.*, alginate capsule dissolution or sensitivity of acinar cells in islet preparations to processing).

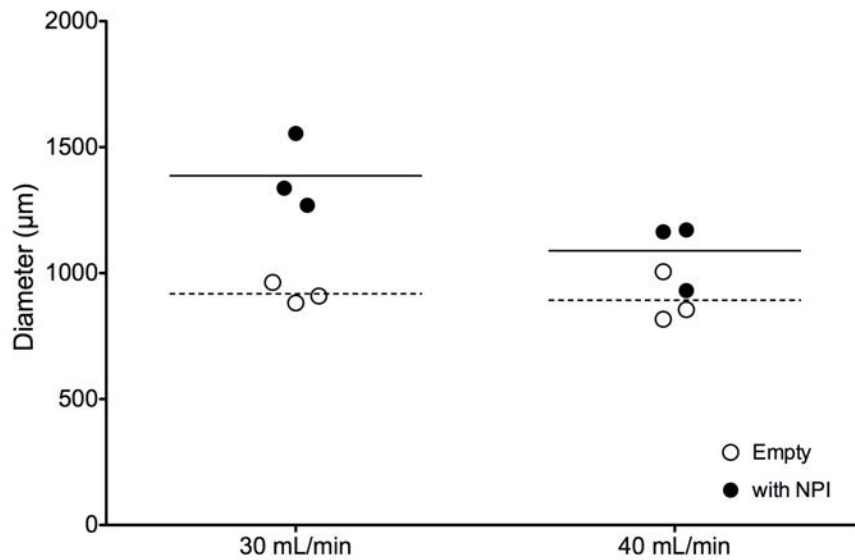


Figure 3.12. Comparing D[4,3] of empty alginate beads and alginate capsules containing NPI.

Solid lines represent the mean value of D[4,3] for alginate capsules containing NPI, while dashed lines represent the mean value of D[4,3] for empty alginate beads. Three different statistical tests were applied to the data:

Unpaired t test (assuming normality and homogeneity) – capsules with NPI vs. empty beads at 30 mL/min, two-tailed p-value = 0.006, $t = 5.259$, $df = 4$; at 40 mL/min, two-tailed p-value = 0.115, $t = 2.005$, $df = 4$.

Unpaired t test with Welch's correction (assuming normality) – capsules with NPI vs. empty beads at 30 mL/min, two-tailed p-value = 0.034, Welch's $t = 5.259$, $df = 2$; at 40 mL/min, two-tailed p-value = 0.139, $t = 2.005$, $df = 2$.

Mann-Whitney test (no assumptions) – capsules with NPI vs. empty beads at 30 mL/min, p-value = 0.100, $U = 0$, sum of ranks = 15, 6; at 40 mL/min, p-value = 0.200, $U = 1.000$, sum of ranks = 14, 7.

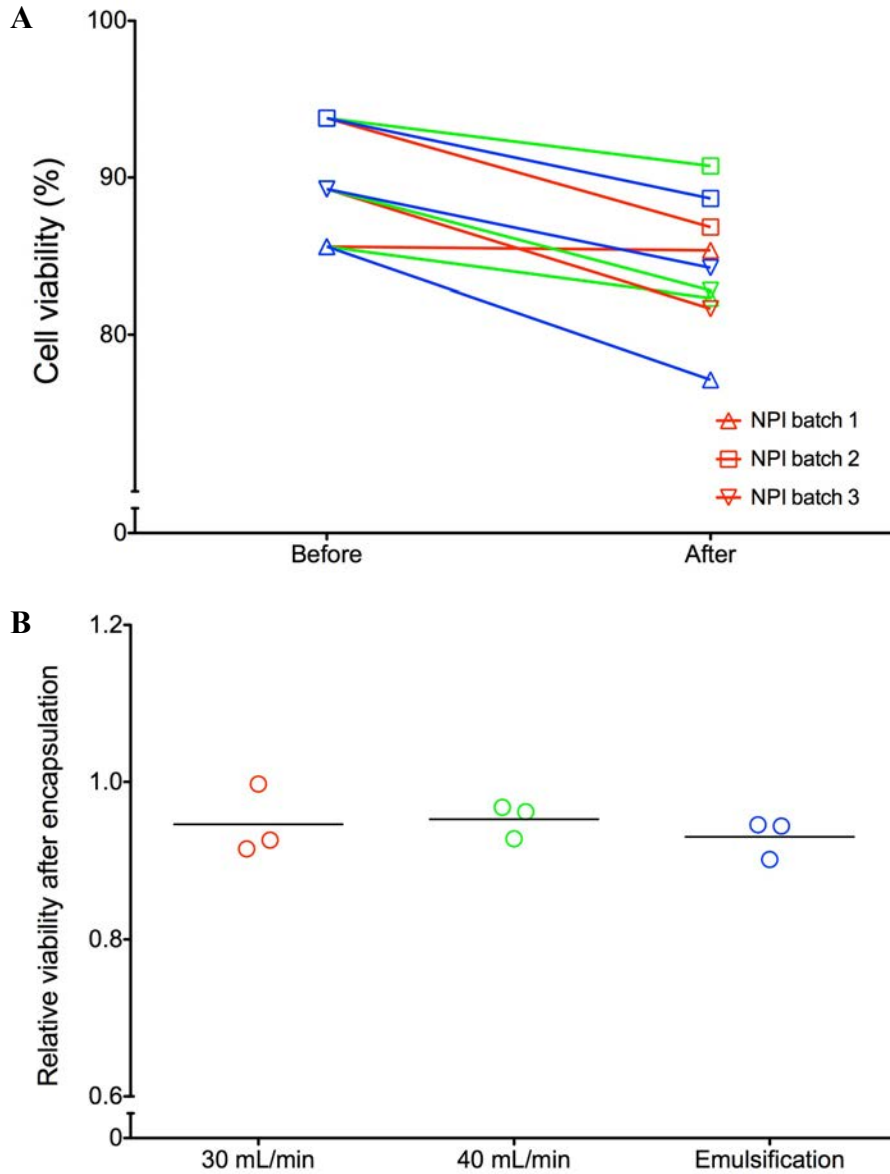


Figure 3.13. NPI viability before and after encapsulation.

(A) NPI from three different batches were dissociated into single cells and viability was assessed via trypan blue exclusion in a hemacytometer before and after encapsulation in alginate through emulsification-internal gelation (blue) or in 3D-printed droplet generators at outer flow rates of 30 mL/min (red) and 40 mL/min (green). (B) Relative viabilities were obtained by normalizing viability after encapsulation (*i.e.*, dividing viabilities after encapsulation by its corresponding viability before encapsulation), and compared using a Kruskal-Wallis test. Lines represent mean of relative viabilities after encapsulation.

In summary, microfluidic devices produced smaller alginate beads than 3D-printed droplet generators. Yet, 3D-printed droplet generators had higher throughput than microfluidic devices, and were more appropriate for encapsulation of NPI without affecting cell viability. However, both types of devices had higher polydispersity than expected when generating empty alginate beads and alginate capsules containing NPI. This issue might have been caused by droplet coalescence and remains to be addressed, and study of droplet formation could contribute in finding a solution (*e.g.*, iterative design of devices and development of more effective cross-linking approaches to prevent coalescence). So far, the comparison of encapsulation processes has been performed mainly in terms of sizing metrics, but a more thorough analysis of capsule quality ought to include measures of encapsulation efficiency and compare encapsulant delivery (*i.e.*, volume ratio between alginate and NPI for better use of transplant volume).

Chapter 4: Exploration of imaging methods for assessment of partial encapsulation

4.1 Rationale

After encapsulation, it is relevant to visualize and analyze the distribution of the encapsulant. Typically, such analyses employ microscopy and their aims include estimation of encapsulation efficiency (*i.e.*, counting number of islets within alginate capsules in a microscope), detection of non-encapsulated islets and defective capsules (*i.e.*, containing partially encapsulated islets), among others. However, common imaging techniques rarely allow the visualization of inner structures (*e.g.*, scanning electron microscopy) or are hampered by the scattered or emitted light from the structures outside the plane of focus (*e.g.*, light microscopy) (Lamprecht *et al.* 2000). In the case of islet encapsulation, light microscopy often misleads analysis by displaying ostensibly encapsulated islets, which might be aligned with the objective while being located at the very bottom of the capsule due to their higher density (Ma *et al.* 2013). These errors in analysis are critical if overlooked in the transplant setting, as partially- and non-encapsulated islets might trigger immune rejection and compromise graft survival.

In the previous chapter, encapsulation methods were assessed in terms of sizing metrics (D[2,0], D[4,3], polydispersity) and potential effects of processing (absolute and relative cell viability). In this chapter, an additional variable for such assessment is introduced. This additional variable is defined as “partial encapsulation”, and pertains to alginate capsules that are defective in the sense that they are not fully covering the encapsulant, *i.e.*, the NPI. The imaging methods explored in this study offered non-destructive analysis platforms to assess encapsulation, *i.e.*, they relied on optical sectioning instead of physical sectioning of samples,

making it possible to perform cross-platform confirmations, as well as allowing the possibility of re-analyzing samples. Furthermore, techniques and protocols that require modifications to the specimen prior to encapsulation (*e.g.*, labeling of the alginate and/or the NPI) were excluded. Additionally, the capacity to scan large regions of interest, *i.e.*, hundreds to thousands of alginate capsules, was deemed crucial not only to reduce measurement time, but also to perform the appropriate comparisons with sufficient statistical power. Finally, resolving power was also considered; imaging techniques that did not sacrifice wide-field imaging capacity for resolution, or vice versa, were preferred because they would allow the estimation of NPI-to-alginate volume ratio that could be used as a surrogate to encapsulation efficiency, thus replacing manual counting in the microscope and/or plate assays (Pisania 2007). Overall, the objective was to find a simple, fast and high-throughput imaging approach to aid in the detection of partially encapsulated NPI.

4.1.1 X-ray computerized tomography

X-ray computerized tomography (CT) enables visualization of three-dimensional structures in opaque samples with a wide range of sizes at micrometer resolution. Biological materials, *e.g.*, soft tissue (NPI) and biopolymers (alginate), are mainly composed of low atomic number elements which are electron-poor structures (elements in the first three rows of the periodic table), hence they yield low contrast in CT because X-rays interact with electrons in the sample. Typically, visualization of biological materials resorts to X-ray-specific labeling with one or more contrast agents, *i.e.*, probes containing high atomic number elements (preferably in the 5th or 6th rows of the periodic table), that absorb X-rays due to their electron density. Differential probe binding leads to differential X-ray absorption rendering an image with contrast between

the materials composing the sample. By taking advantage of the transmissive nature of X-rays when compared to visible light, the internal structure of the sample can be reconstructed in terms of its X-ray absorbance by rotating it in front of an array of X-ray detectors (Figure 4.1A). Sequential two-dimensional images, or projections, are obtained while the sample is being rotated, then broken down into rows of pixels that are subjected to a back projection algorithm to add spatial information resulting in a microtomogram, *i.e.*, a block of images representing the sampled volume sectioned perpendicularly to the axis of rotation (Figure 4.1C).

4.1.2 Optical projection tomography

Optical projection tomography (OPT) is analogue of a CT scan but using an optical source instead of X-rays, and incorporating the capabilities of fluorescence microscopes and some colorimetric assays (Sharpe 2003; Sharpe *et al.* 2002) instead of using differential X-ray absorption and labeling with high atomic number elements. The latter is achieved by imaging specimens embedded in agarose blocks, which are immersed in clearing solution (1:2 mixture of benzyl alcohol and benzyl benzoate) that renders them transparent. Then, a wave of diffuse light passing through the specimen is collimated by the microscope and recorded by a cooled charge-coupled device (CCD) camera (Figure 4.1B). The raw data obtained from every pixel corresponds to a narrow light cone projected through the specimen resulting in images with a view right through the specimen that lack explicit information about depth; however, as the specimen is rotated and images are obtained at several angles, the data in all these views can be mathematically transformed to recreate the original object (Figure 4.1C).

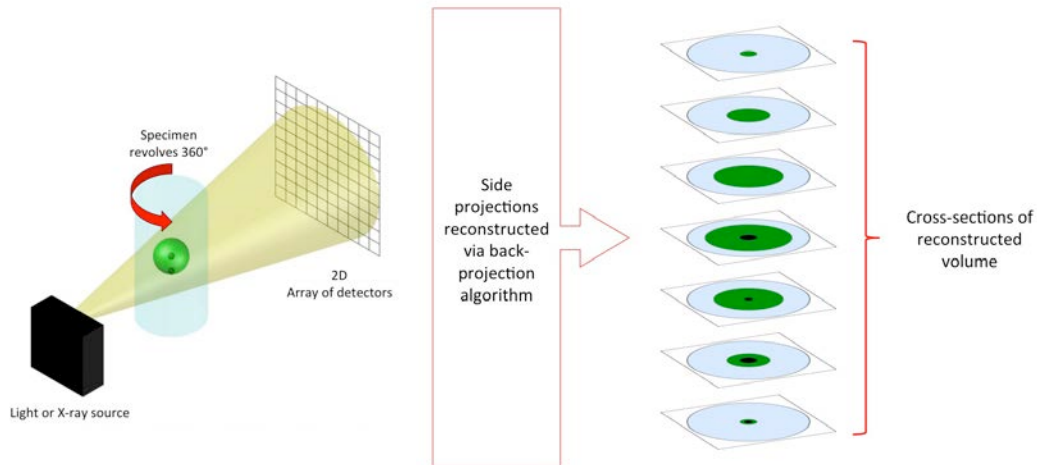


Figure 4.1. Schematic of imaging principles in tomographic techniques.

The specimen is exposed to a cone beam of X-rays in CT, or a cone of light in OPT, while being rotated in front of a detector array. The latter captures information at every angle of the revolution generating projections. The data is mathematically reconstructed into a volume consisting of cross-sectional images of the specimen.

4.1.3 Confocal microscopy

Laser scanning confocal microscopy (LSCM) allows visualization of three-dimensional structures by virtue of its ability to optically section a sample. This optical sectioning is possible due to the exclusive collimation of the photons emitted and/or reflected in the plane of view, while the sample is being exposed to light of a specific wavelength. The exclusive collimation is achieved by using a pinhole to exclude photons emitted/reflected from sections of the sample that are out of focus, and concentrating the photons that pass through the pinhole with a set of mirrors. Light of a specific wavelength is used to preferentially excite one or more fluorophores, *i.e.*, fluorescence-emitting dyes, added to the sample to serve as probes targeted to different components of the sample in order to obtain differential coloring and/or intensity. Then, a set of two-dimensional images obtained at different planes of view (*i.e.*, Z-steps) can be combined, or

stacked spatially, to obtain a three-dimensional rendering of the sample with detailed visualizations of its internal structure.

Recently, through confocal microscopy analysis, Ma *et al.* compared the encapsulation of mouse islets attained with traditional droplet generators and a two-fluid co-axial electro-jetting encapsulator capable of generating core-shell alginate capsules (Ma *et al.* 2013). Hydrogel-fluorophore conjugates were generated for capsule shell labeling, and stained islets with DAPI for visualization. Although this approach seems applicable for the purposes of this study, the authors' analysis was qualitative and restricted to a limited number of alginate capsules; furthermore, the on-demand need for fluorescently labeled alginate conflicts with the purpose of retrospective analysis established earlier. Alternatively, by taking advantage of the commercial availability of high molecular weight proteins and polymers labeled with fluorophores, the milieu around the alginate capsules can be stained to resolve their boundaries (Figure 4.2). This approach has been used to monitor permeability changes in cultured alginate microcapsules (Lv *et al.* 2009), and complies with the aforementioned requirements for analysis of partial encapsulation.

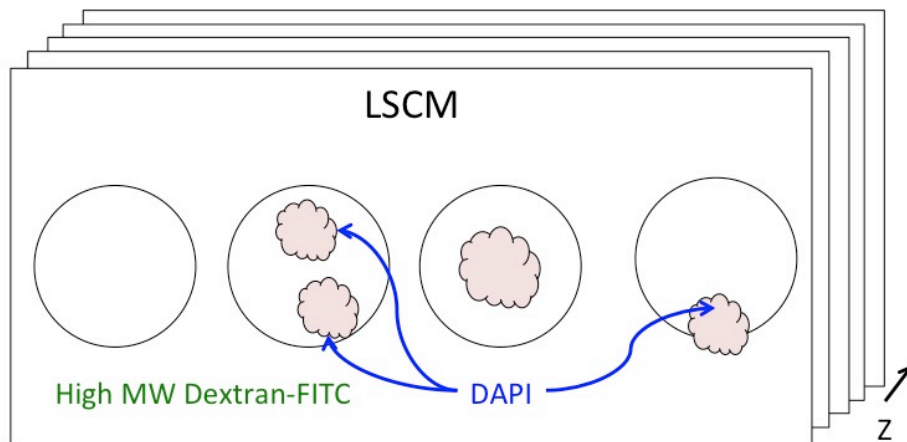


Figure 4.2. Schematic of labeling protocol for detecting partially encapsulated NPI using laser scanning confocal microscopy.

NPI inside alginate capsules are labeled with a nuclear stain (*e.g.*, DAPI), while the boundaries of the alginate capsules are resolved by labeling the medium with a conjugate of fluorescein isothiocyanate (FITC) and high molecular weight dextran, which is size-excluded from the alginate matrix. Imaging is performed over a wide region of interest and at several focal planes to obtain cross-sectional images of the sample.

4.2 Materials and methods

4.2.1 Sample fixation

Alginate capsules containing NPI were fixed overnight in an orbital shaker at 100 rpm, using storage buffer mixed with 10% v/v of a 40% v/v formaldehyde solution (Fisher Scientific).

4.2.2 Imaging with OPT

Fixed alginate beads were embedded layer-by-layer in agarose blocks. Briefly, a 20-cm petri dish was filled with 2% w/v agarose (Sigma) solution. After the agarose solution cooled down and solidified, holes were punched using a #9 cork borer. A 50- μ L aliquot of fixed alginate beads was dried on a piece of paraffin paper by buffer aspiration. The alginate beads were re-

suspended in 100 μL agarose solution at 60 $^{\circ}\text{C}$, and transferred to a hole in the agarose. The dish was placed at -20 $^{\circ}\text{C}$ for 5 min to cool down the agarose, and then topped with 50 μL agarose solution. The process was repeated until the hole was filled to the brim.

Agarose blocks were cut using a #11 cork borer and trimmed to ensure a flat bottom. Trimmed blocks were dried in methanol for 24 h, replacing the solution every 6 h. The agarose blocks were incubated in 1:2 benzyl alcohol/benzyl benzoate (all from Fisher Scientific) (BABB) solution for 24 h for clearing, which rendered them transparent, and stored in fresh BABB solution.

Samples were imaged using an OPT scanner 3001M (Bioptronics). Briefly, cleared agarose blocks were removed from storage tubes and mounted in the sample holders using the cyanoacrylate adhesive Permabond 200 (Sigma). The sample holder was placed and centered in the instrument's motorized stage. The sample was lowered into a cuvette filled with fresh BABB solution, and regions of interest were identified in transmission mode at a resolution of 24 $\mu\text{m}/\text{pixel}$. A snapshot was captured and exported to ImageJ to calculate the projection's center of mass, which was aligned with the instrument's axis of rotation by adjusting the placement of the stage; the process was repeated after rotating the sample 90 $^{\circ}$. After alignment, samples were scanned in transmission and fluorescence mode at 400 positions while completing one revolution. Sample projections were reconstructed using NRecon software (Bioptronics), yielding a Z-stack of TIFF files containing 24- μm thick optical cross-sections of the scanned volume in two channels.

4.2.3 Imaging with CT

A 50- μ L aliquot of fixed alginate beads was dried on a piece of parafilm by buffer aspiration and transferred to screw cap flat bottom 5.5 mm x 57 mm vial (Sarstedt). A 150- μ L aliquot of a ferrofluid solution (see Table 4.1) was added to the sample. Alternatively, the alginate beads were embedded in 1% w/v agarose loaded with 2% w/v E-Z-HD BaSO₄ (E-Z-EM Canada Inc.) suspension.

Table 4.1. Iron oxide particle solutions used as contrast agents in CT scans.

Solution	Diameter of magnetic particles	Dispersant	Source
1	3 – 5 μ m	Water	Chemicell
2	1 μ m	Ethanol	Hafeli lab
3	200 nm	Water	Chemicell
4	30 nm	DI water	Ferro Tec

Samples were submitted to the Centre for High-Throughput Phenogenomics for scanning in a Scanco Medical μ CT100. Unless stated otherwise, samples were placed in 73-mm sample holders stuffed with kimwipes to hold the samples in place during scanning. A preliminary scan was performed to identify the regions of interest and assign the detectors to capture the desired scanned volume. The definitive scan was performed at 17 μ m/voxel resolution, 45 keV beam energy, 200 μ A current, 600 ms integration time, 500 projections. Five hundred projections per sample were captured and reconstructed by the Scanco Medical software suite yielding Z-stacks of 17- μ m thick cross-sections, which were exported as 8-bit TIFF files.

4.2.4 Imaging with LSCM

A 50- μ L aliquot of fixed alginate beads was stained with 300 nM DAPI (Invitrogen) solution for 5 min. The beads were washed 3 times with 1 mL storage buffer. Stained beads were

spun down and incubated in 10 mL storage buffer mixed with 1% w/v poly-L-lysine (PLL from Sigma) for 30 min in an orbital shaker at 100 rpm, followed by another 3 washes in storage buffer. Coated beads were spun down and re-suspended in 2 mL 0.2 mg/L 20 kDa dextran-FITC (Sigma).

Samples in dextran-FITC were transferred to dual-chambered slides (Lab-Tek) and imaged with a Leica SP5 X laser scanning confocal microscope.

Image acquisition consisted of a preliminary scan where the full area of a chamber was scanned in a single optical slice using the FITC and DAPI filters. After the region of interest was identified, its volume was imaged in tile mode with auto-stitching, using a resolution of 20 $\mu\text{m}/\text{pixel}$ and a Z-step of 50 μm .

4.3 Results and discussion

4.3.1 OPT scans

OPT had the fastest turnover time for scanning and reconstruction. A typical scan took around 7 min per channel, while reconstruction took between 5 to 10 minutes depending on the number of channels used during the scan – most samples were scanned in 2 or 3 channels. However, sample preparation was laborious due to agarose mould preparation and sample embedding, and rather lengthy (> 48 h) because of the dehydration and clearing steps. More importantly, as can be seen in Figure 4.3, simple embedding by sample re-suspension in melted agarose resulted in a random spatial distribution of the alginate capsules that might complicate the analysis. Additionally, the random spatial distribution of the alginate capsules generated reconstruction artifacts, *i.e.*, slight shifts in the location of some alginate capsules that resulted in overestimation of their true size.

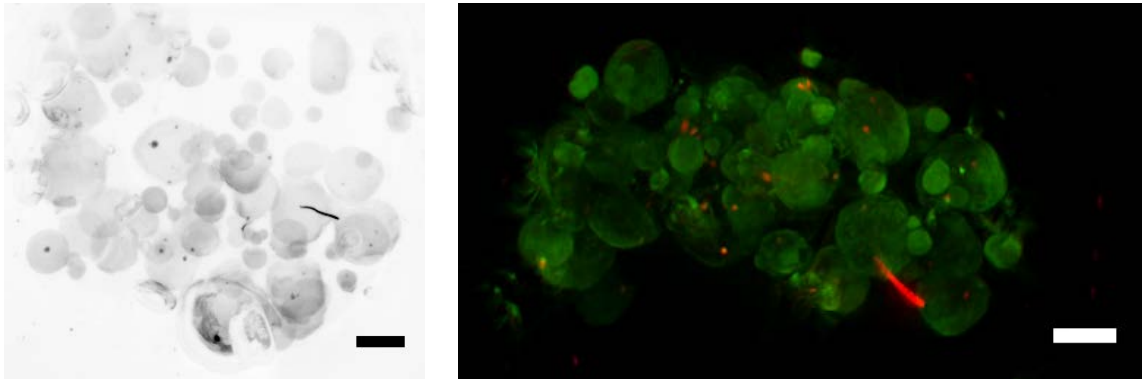


Figure 4.3. OPT scan of alginate capsules containing NPI.

A 100- μ L sample of alginate capsules containing NPI was dried, re-suspended in melted agarose, and transferred to an agarose mould. After the agarose gelled, a block embedding the sample was cut, then dehydrated, cleared and scanned. Left: side view of sample scanned in the visible channel. Right: top view of maximum intensity reconstruction of the same sample scanned in visible (green) and autofluorescence (red) channels. Alginate capsules were imaged in the visible channel, while the autofluorescence channel was used to image NPI. Scale bar: 1 mm.

For subsequent imaging via OPT (*e.g.*, Figure 4.4), layered embedding of samples was adopted to potentially facilitate analysis by introducing references (*i.e.*, top and bottom of a layer) common to sub-sets of alginate capsules embedded in the agarose block, but substantially diminishing the number of alginate capsules per sample. Also, an alignment step, as described in (Eriksson *et al.* 2013), was introduced to minimize the occurrence of artifacts; prior to every scan, the centers of mass of two orthogonal side projections of the alginate capsules in the visible channel were aligned with the axis of rotation of the sample holder. Nevertheless, reconstruction artifacts were still present despite the alignment (Figure 4.4D). These artifacts might be the product of inadequate sample preparation, specifically tilted cuts on agarose blocks yielding uneven surfaces that are difficult to anchor to the sample holder. Considering only one of the faces of the agarose block is fixed to the sample holder, uneven surfaces inevitably result in

scanning of crooked samples. Thus, although the software used for reconstruction can handle these impending motion artifacts (Walls *et al.* 2005), OPT was developed as a technique for analyzing a single specimen per agarose block. The samples in this study contained a three-dimensional array of alginate particles, some of which were located in the outer rims of the agarose block. The particles there orbited around the axis of rotation while being scanned. Therefore, the reconstruction algorithm might have not been able to cope with motion artifacts, as the imperfect axial alignment of the agarose block with the axis of rotation, coupled with orbital movement of the alginate capsules, results in poor spatial data for the array of alginate capsules and overestimated the size of some of them. In summary, sample preparation, especially embedding in agarose blocks, introduced artifacts that produced images inadequate for assessment of partial encapsulation. Furthermore, it seems that imaging via OPT might not allow scanning hundreds or thousands of alginate capsules per sample.

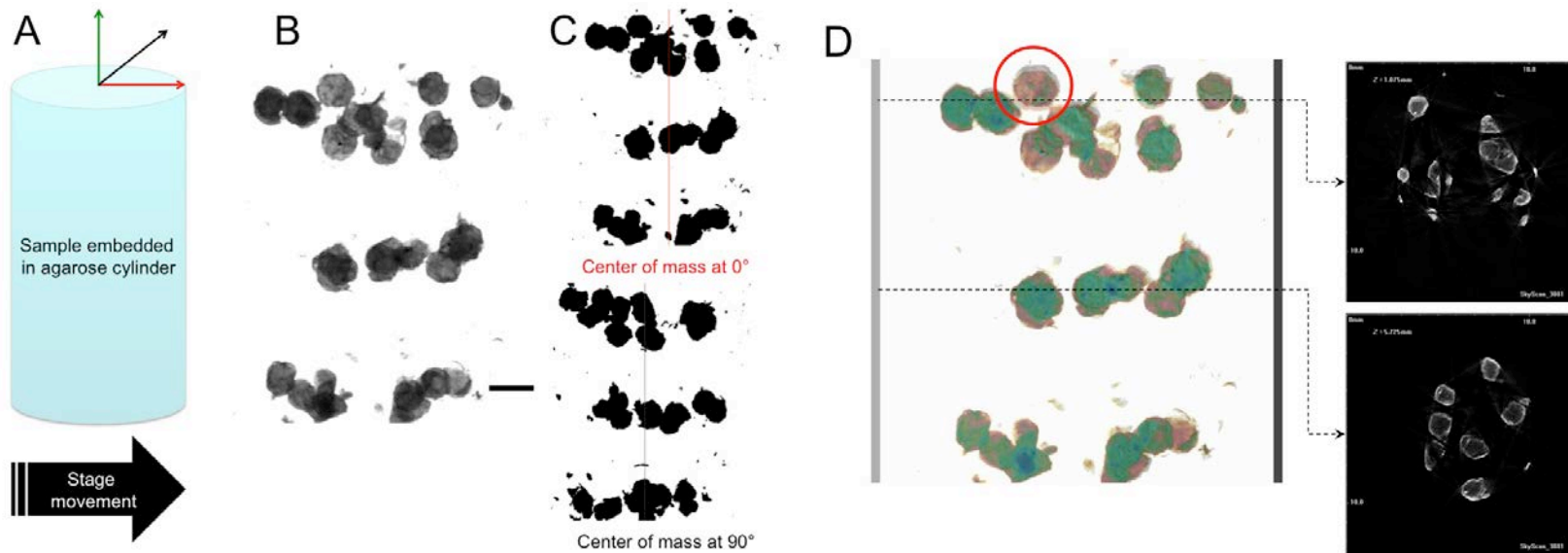


Figure 4.4. OPT scanning with alignment of center of mass and axis of rotation.

(A) Diagram of OPT sample holder, colored arrows denote the axes of the agarose block; X, Y and axis of rotation are shown in red, black and green, respectively. (B) Projection of agarose block containing alginate capsules with NPI. Scale bar: 1 mm. (C) Prior to a scan, binary masks were used for orthogonal alignment of centers of mass of projections with the axis of rotation. (D). Side view of scanned volume reconstructed from projections (left panel) and optical cross-sections (right panels). The red circle denotes an example of a poorly reconstructed section due to orbital movement of alginate capsules around the axis of rotation.

4.3.2 CT scans

CT scan and reconstruction times were slower compared to OPT. A typical scan lasted 20 – 30 min, while reconstruction was usually performed overnight, resulting in a turnover time of about 1 day. Conversely, sample preparation for CT was rather simple, as it only required re-suspension of the alginate capsules in buffer containing the contrast agent. Even in the case of barium sulfate-loaded agarose, sample preparation rarely exceeded 5 – 10 min per sample (considering agarose melting/dissolution, re-suspension and gelation). Unfortunately, despite all its simplicity, CT by itself did not offer enough resolving power because of the small contrast resulting from the differential X-ray absorbance of the alginate, the buffer and NPI (Figure 4.5A). Therefore, high atomic number elements were added to the media in order to increase its X-ray absorbance and enhance its contrast against the alginate capsules.

Alginate capsules were placed in a 1.4 mg/mL solution of Omnipaque, a commercial iodine contrast agent containing water-soluble iohexol. However, because of its small size, iohexol permeated through the alginate matrix and stained the NPI, resulting in images with no contrast between the NPI and the alginate, and a negligible contrast between the alginate and the media (Figure 4.5B) that made it difficult to even find regions of interest. Therefore, particulate contrast agents were employed to enhance the contrast of the media.

Barium sulfate was used because of its commercial availability and relatively small grain sizes ($< 10 \mu\text{m}$). However, this salt has limited solubility in water and formed suspensions with rapid sedimentation. To counter the latter, well-mixed barium suspensions were combined with melted agarose in order to slow down sedimentation by modulating viscosity (*i.e.*, adding more agarose and/or increasing temperature) and inducing agarose gelation through rapid cooling. Alginate capsules were embedded in barium-loaded agarose and imaged, but particle

sedimentation persisted (Figure 4.5C). Lower concentrations of barium sulfate did not sufficiently enhance the contrast between the media and the alginate (not shown). In subsequent tests, suspensions of contrast agents were replaced with solutions containing smaller particles to reduce sedimentation, while ensuring that particle size was not small enough to allow diffusion through the alginate matrix.

Magnetic silica microparticles and iron oxide nanoparticles of different sizes were used to enhance the contrast of the media (Figure 4.5D–F), but dispersions of iron oxide nanoparticles as small as 200 nm still precipitated, and only 30-nm iron oxide nanoparticles resulted in a stable dispersion (see appendix B.7) adequate for further imaging. Nevertheless, in subsequent scans using the aforementioned contrast agent, the contrast between the NPI and the alginate was negligible, and when resorting to smaller sample holders to improve resolution, analysis was hampered by granularity in the X-ray absorbance of the media (Figure 4.6). Additionally, due to the use of a smaller container, the alginate capsules stacked on top of each other, *i.e.*, packing the vessel, which made it difficult to identify their boundaries during analysis. Moreover, the possibility of analyzing large sample volumes, and hence thousands of alginate particles per particles, was compromised while using microcentrifuge tubes. In summary, visualization of alginate capsule boundaries was only possible with the aid of iron oxide contrast agents, especially colloidal dispersions. However, NPI were not resolved unless relatively small sample volumes were scanned. Therefore, for the assessment of partial encapsulation, CT scans might require use of additional contrast agents in order to resolve NPI and alginate capsules boundaries.

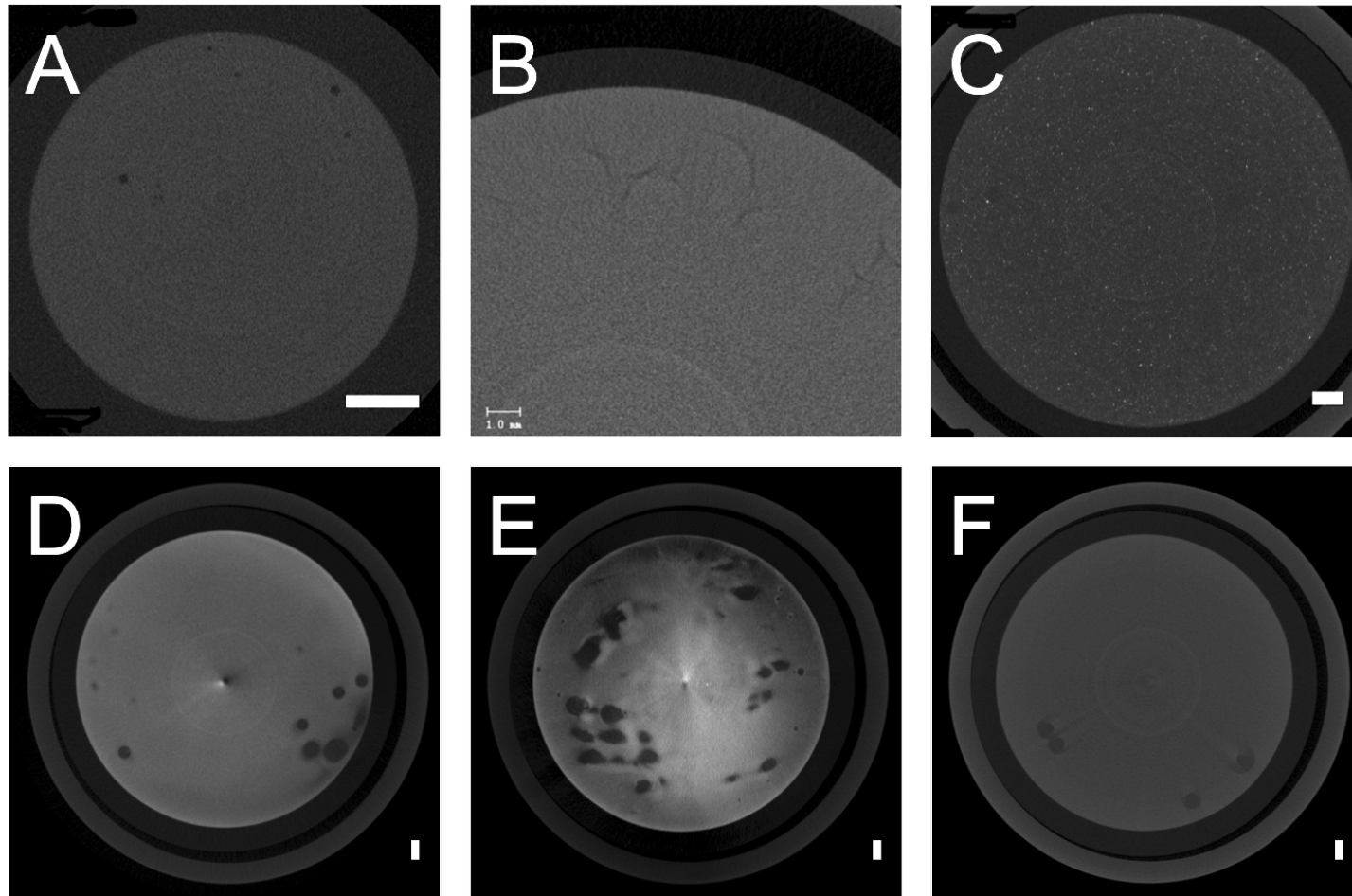


Figure 4.5. CT scans using different contrast agents.

(A) No contrast agent added. (B) Iodinated contrast agent, iohexol (Omnipaque). (C) Barium sulfate. (D) Suspension of 3 to 5- μm sized magnetic silica particles.

(E) Suspension of 1- μm magnetic particles. (F) Dispersion of 200-nm magnetic nanoparticles. All scale bars: 1 mm.

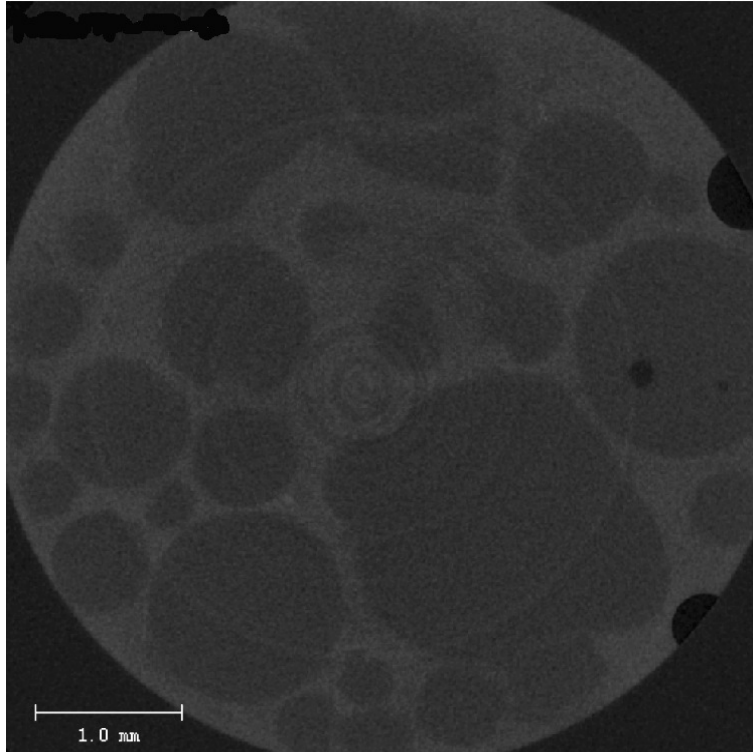


Figure 4.6. CT imaging with 30 nm iron nanoparticle solution as contrast agent.

Alginate capsules containing NPI were re-suspended in buffer containing ~0.025% w/v 30 nm iron nanoparticles, transferred to a 1.5-mL microcentrifuge tube, and scanned using a 19-mm sample holder at 10 μm /voxel resolution. CT parameters: 45 keV peak voltage, 200 μA current, 600 ms integration time, 500 projections.

4.3.3 LSCM micrographs

Confocal microscopy was relatively slow in image acquisition (typically 1 h for a volume of 1.5 mL). The ensuing image analysis was done by tile stitching, not volume reconstruction, which typically took less than 1 h, resulting in measurements transpiring in 90 – 120 min.

Sample preparation was rather simple, consisting mostly of cycles of incubation and washing steps accounting for about 1 h. The use of chamber slides allowed the possibility of imaging a larger number of alginate capsules while ensuring a spatial arrangement where all capsules had a common reference (*i.e.*, the bottom of the chamber slide) hence facilitating the possibility of

analysis. About half of the volume of the chambers was packed with alginate capsules, while the remainder was filled with FITC-dextran solution. This approach made it difficult to stitch the image tiles because the void space allowed the alginate capsules to roll while the motorized stage was moving to image the whole slide (Figure 4.7A). To obtain higher quality images, the stage was moved to focus on a region of interest and remained static for the remainder of image acquisition, although this meant a smaller number of alginate capsules was imaged. Interestingly, imaging revealed that DAPI stained both the NPI and the PLL coating on the alginate capsules. Moreover, the signal from FITC was rather noisy and made it difficult to distinguish the boundaries of the alginate capsules (not shown). Therefore, it seems that the washes between the incubations in DAPI and PLL were critical steps during sample preparation to avoid undesired dyeing of the the PLL coating. Despite this flawed staining it was still possible to detect the occurrence of partially encapsulated NPI protruding from the alginate capsules (Figure 4.7B). In summary, alginate capsule movement hindered analysis of larger sample volumes. Similarly, unspecific labeling of PLL with DAPI prohibited further image analysis. Still, LSCM resolved the materials of interest in the sample. Therefore, this imaging technique might be adequate for assessment of partial encapsulation, if differential labeling of NPI and alginate capsule boundaries can be achieved.

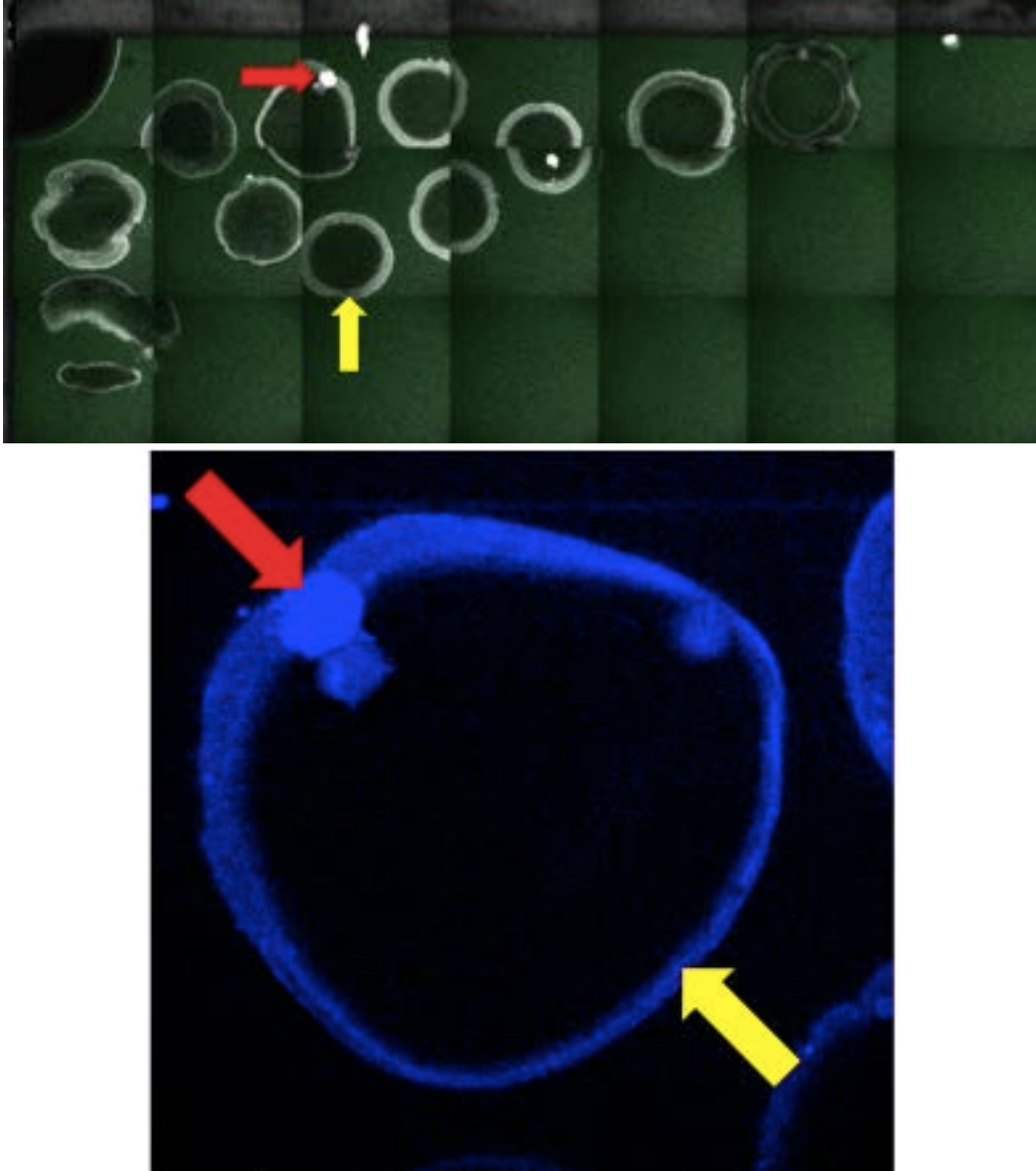


Figure 4.7. Imaging of alginate capsules with confocal microscopy.

Alginate capsules containing NPI were stained with DAPI, washed and then coated with PLL (yellow arrows) to exclude high molecular weight dextran during imaging. (A) Tile of micrographs stitched showing FITC-Dextran in green and DAPI in gray. The red arrow points to an ostensibly partially encapsulated NPI. (B) The capsule with the partially encapsulated NPI was re-scanned while maintaining the stage immobile. DAPI stain shown in blue.

4.4 Conclusions

4.4.1 Summary

The imaging techniques of confocal microscopy, X-ray computerized and optical projection tomography were explored to assess their capabilities for detecting partially encapsulated NPI in relatively large samples containing hundreds to thousands of capsules. The time required for sample preparation, image acquisition, and reconstruction (if applicable) were considered, as well as the quality of the resulting images in terms of the amenability to high-throughput image analysis. Imaging protocols avoiding on-demand generation of fluorescently labeled alginate were preferred because of their simplicity, potential reproducibility and ability to analyze samples retrospectively.

Tomographic techniques (OPT and CT) were of special interest because of their ability to reconstruct sample volume with little loss of spatial information, unlike imaging acquisition in a confocal microscope that uses Z-stepping and invariably “skips” part of the specimen. However, tomographic imaging had limited success in fulfilling the aforementioned imaging requirements. CT imaging relied on the contrast resulting from differential X-ray absorption of the materials in the specimen, but this contrast in the images was visible only when adding a colloidal dispersion of 30-nm iron oxide nanoparticles and scanning smaller samples, which should contain less alginate capsules in order to make analysis feasible. OPT imaging required and relied on challenging sample preparation, where the shape of the agarose blocks embedding the samples, and the spatial arrangement of the capsules inside of it, greatly affected the reconstruction process, and generated artifacts that could render analyses invalid.

Imaging via confocal microscopy was based on the exclusion of high molecular weight dextran-FITC conjugates while simultaneously labeling NPI with DAPI. Movement of the

alginate capsules occurred when imaging large areas of the sample resulted in poorly stitched mosaics, thus image acquisition was restricted to a limited number of alginate capsules in order to minimize movement of the capsules while the stage moved. Routine pinpoint imaging (*i.e.*, imaging a whole sample one capsule at a time) was avoided in order to maintain the ability to measure several samples per imaging session. Unfortunately, the fluorescent labeling protocol, which included a PLL coating step to exclude the other fluorescent dye, produced unspecific binding or entrapment of excess DAPI in the PLL layer. The latter resulted in images where the NPI and the boundaries of the alginate capsules had the same signal, which was undesirable for further image analysis. Yet, this was the sole method capable of producing images with relatively good resolution of the alginate capsules and the NPI, especially when imaging smaller numbers of alginate capsules on an idle motorized stage. Therefore, it seems that LSCM has more potential than OPT and CT for the development of imaging method for assessing partial encapsulation.

4.4.2 Recommendations and future work

OPT, as mentioned before, is heavily dependent on the surface quality of agarose blocks and the spatial arrangement of the specimen within it. Embedding between 1 to 10 alginate capsules per block (while ensuring they are roughly on the same plane) is a potential solution to tackle the artifacts arising due to orbital and axial misalignment. However, this approach would make the sample preparation extremely laborious because hundreds of agarose blocks would have to be prepared, imaged and analyzed in order to maintain statistical power.

CT is a more established technique than OPT, and the absence of artifacts in the images obtained during this study is encouraging to pursue further exploration. Yet, the contrast agents

used for CT imaging did not facilitate the distinction between the materials in the specimen, and different high atomic number probes ought to be tested. Osmification of the encapsulated NPI using osmium tetroxide seems plausible, especially considering the permeability of the probe that yields uniform X-ray absorption even in thick samples (Mizutani & Suzuki 2012).

Drawbacks of osmification are that a relatively laborious sample preparation, and especially lengthy (overnight) incubation times are required, and that the osmium compound is highly toxic. Alternatively, iodination through incubation with elemental iodine solutions (Mizutani & Suzuki 2012) is capable of generating similar visualizations of soft tissues by X-ray tomography without the concern of handling toxic chemicals. In any case, osmification or iodination of the encapsulated NPI would both require release of the excess probe from the alginate matrix after sample washing in order to establish a contrast between these materials. Additionally, a second contrast agent (*e.g.*, colloidal dispersion of iron oxide nanoparticles) could be added to the media in order to facilitate resolution of the boundaries of the alginate capsules.

Confocal microscopy produced low-quality images when scanning large areas due to the movement of the alginate capsules. This issue could be easily solved by increasing the viscosity of the media containing the alginate particles, or by re-suspending the sample in melted agarose and generating an agarose block within the chamber slide. Another issue during confocal microscopy imaging was the unexpected labeling of the PLL coating with DAPI, which might seem a fortunate mistake that enables simpler sample preparation and faster image acquisition in a single channel, however imaging with the PLL coating and the NPI outputting signals in the same channel might complicate analysis. Therefore, it would be better to exploit this phenomenon while ensuring image acquisition transpires in at least two channels by adding a red or green fluorescent dye to label the NPI. Alternatively, a fluorophore-PLL conjugate (*e.g.*, PLL

labeled with Alexa 546 (Strand *et al.* 2003)) could be used during the coating step to obtain images where the boundaries of the alginate capsules are resolved because of the fluorescent coating, while the NPI remain stained with DAPI. Such images with differential labeling in two channels would be more amenable to high-throughput image analysis. Overall, applying tomographic techniques for assessing partial encapsulation would require a major overhaul in the approaches used for sample preparation. Conversely, confocal microscopy imaging presented issues that seem more manageable, and the proposed improvements would be simpler to implement.

Clearly, detection of partially encapsulated NPI, or more generally, identification of defective alginate capsules, would not be sufficient to improve transplantation outcomes, and a separation step ought to be developed to remove such defective capsules. Affinity binding-based approaches have been used for the detection of partially encapsulated islets (De Vos *et al.* 1996), and the lectins employed for islet-specific binding could be employed in separation techniques by immobilization on a substrate (Monzo *et al.* 2007) designed to retain capsules with partially encapsulated NPI. Alternatively, all capsules could be deemed likely to present partially encapsulated NPI, in which case a blanket approach could be adopted and all capsules would be subjected to a coating step in order to minimize the occurrence of NPI protruding from their capsules. Still, a robust method for detection of defective capsules would be necessary in order to assess the effectiveness of either the separation and/or the coating processes. Using confocal microscopy, adopting the proposed improvements, and maintaining accordance with the imaging needs established earlier would contribute in devising such method for the detection of defective alginate capsules. Moreover, furthering the findings of this study could provide a platform for the

study of other phenomena relevant for the enhancement of islet transplantation as a therapeutic option (*e.g.*, relation between spatial distribution of NPI with survival *in vitro* and *in vivo*).

Chapter 5: Conclusions

5.1 Summary

This study focused on the feasibility of encapsulating NPI in 5% w/v alginate solutions through droplet generators designed for compatibility with the internal gelation mechanism. Furthermore, the overall objective of implementing such devices for encapsulation was to attain a narrow size distribution of alginate capsules while maintaining a relatively high-throughput (*i.e.*, hundreds to thousands of capsules per minute). For this purpose, two types of devices were fabricated, namely PDMS microfluidic chips and 3D-printed droplet generators. The microfluidic devices utilized inverted nozzles for alginate droplet generation and downstream addition of acidified oil for gelation, while 3D-printed droplet generators utilized acidified oil for droplet generation and subsequent gelation downstream. Furthermore, the devices also differed in their geometry; microfluidic devices were planar with rectangular channels whereas the 3D-printed droplet generators had concentric cylindrical channels with four different geometries. To achieve this concentric arrangement, a blunt needle was inserted and aligned in a 3D-printed structure with barbed connectors, which were amenable for easy and seamless connections with tubing. The alignment of the concentric arrangement was assessed through X-ray computerized tomography and the effects of misalignment were studied in performance tests consisting in generation of empty alginate beads. Finally, the effect of increasing the flow rate of the acidified oil was studied in 3D-printed droplet generators. The following conclusions could be made:

Table 5.1. Summary of dimensions of droplet generators and their operating conditions.

	Design	Channel dimensions in mm				Operating conditions		Particle size in μm	
		Oil inlets	Alginate inlets	Orifice	Barb hose	Oil flow rate	Alginate flow rate	D[4,3]	CV
Microfluidic (rectangular channels)	-	0.40x0.48x8.50 (W x H x L)	0.40x0.48x3.00 (W x H x L)	0.40	-	6 mL/min	2 mL/h	561	26.7%
3D-printed (cylindrical channels)	1	1.00x25.00 (D x L)	0.51x1.27 (D x L)	1.00	2.0 3.0 5.0	30 – 50 mL/min	200 $\mu\text{L}/\text{min}$	773 – 880	21.5 – 33.1%
	2	1.00x25.00 (D x L)	0.51x1.27 (D x L)	1.00	3.1 4.0 5.0			911 – 1,099	25.3 – 28.8%
	3	1.00x25.00 (D x L)	0.84x1.27 (D x L)	1.00	3.1 4.0 5.0			817 – 961	15.6 – 23.3%
	4	1.00x25.00 (D x L)	0.84x1.27 (D x L)	0.70	3.1 4.0 5.0			844 – 936	13.4 – 18.4%

1. Microfluidic devices had smaller channels and produced smaller alginate beads than 3D-printed droplet generators. The former had D[2,0] of $449 \pm 10 \mu\text{m}$, and D[4,3] of $561 \pm 46 \mu\text{m}$. While the smallest beads obtained with 3D-printed droplet generators had D[2,0] of $494 \pm 22 \mu\text{m}$, and D[4,3] of $773 \pm 29 \mu\text{m}$.
2. Both types of devices produced higher polydispersity than expected (CV > 10%).
Typically, microfluidic devices operating under the dripping regime produce monodisperse droplets (*i.e.*, $\text{CV} \leq 2 - 3\%$) (W. Lee *et al.* 2009). Even when operated with highly viscous alginate solutions ($\sim 3\%$ w/v), microfluidic devices have produced highly monodisperse alginate particles ($\text{CV} < 1\%$) (Berthier *et al.* 2010). Similarly, co-axial (Sakai *et al.* 2004) and axisymmetric (Morimoto *et al.* 2009) droplet generators have also been reported to produce narrowly sized distributions of alginate particles ($\text{CV} < 7.5\%$ & 5% , respectively). In this study, alginate droplet coalescence prior to alginate gelation was still observed despite the addition of surfactants, which also did not reduce polydispersity.
3. 3D-printed droplet generators had larger channels that allowed higher operating flow rates and higher throughput than microfluidic devices. On average, 3D printed devices produced over 200 – 300 alginate beads per minute. Conversely, microfluidic devices had a bead formation frequency of ~ 10 alginate beads per minute. Due to their lower throughput, encapsulation in microfluidic devices was slow and translated into a loss of MIN6 cell viability over time. On the other hand, encapsulation in 3D-printed droplet generators had no immediate effect in NPI viability.
4. Two types of alignment errors incurred during fabrication were observed in 3D-printed droplet generators but had no significant effect on performance in terms of polydispersity.
X-ray imaging revealed that needles were prone to end up angled relative to the center of

the 3D-printed structure. Also, a few devices had needles offset from the center of the 3D-printed structure. However, these misalignment angles and offsets were small ($< 2^\circ$ & $100\ \mu\text{m}$, respectively), hence having little to no impact in the polydispersity of empty alginate beads generated at 30, 40 & 50 mL/min.

5. Increasing the acidified oil flow rate from 30 mL/min to 40 mL/min significantly reduced the size of empty alginate beads and alginate capsules containing NPI. As expected, alginate beads and capsules were larger when produced at lower acidified oil flow rates in 3D-printed droplet generators. Devices with design 4 (*i.e.*, with $838\text{-}\mu\text{m}$ inner channels and $700\text{-}\mu\text{m}$ orifices) were chosen for encapsulation to minimize the risk of inner channel clogging. Although NPI affected alginate capsule size in terms of $D[4,3]$ (beads: $913 \pm 24\ \mu\text{m}$ vs. capsules: $1387 \pm 86\ \mu\text{m}$), alginate capsule size was restored to typical bead size by increasing the outer flow rate to 40 mL/min (beads: $893 \pm 58\ \mu\text{m}$ vs. capsules: $1089 \pm 79\ \mu\text{m}$).

Overall, these findings indicate that 3D-printed droplet generators were superior to microfluidic devices, especially because of their capability to operate at higher flow rates without incurring leaks hence enabling relatively high-throughput production of beads and NPI-containing capsules from highly viscous alginate solutions. However their design, fabrication and operation has plenty of areas of opportunity for improvement. When compared to emulsification-internal gelation, which has relatively well established measures to control alginate capsule size by modulation of the agitation speed and the alginate-to-oil ratio (Hoesli 2010), 3D-printed droplet generators have yet to attain better control over alginate capsule diameter by modulation of the outer flow rate. Moreover, it is clear that NPI encapsulation using

3D-printed droplet generators could benefit from implementation of successful measures to minimize or prevent droplet coalescence in order to potentially reduce polydispersity and ensure an NPI-to-alginate volume ratio suitable for transplantation.

5.2 Recommendations and future work

3D-printed droplet generators were operable at higher flow rates than microfluidic devices but were not impervious to leaks despite the use of barbed connectors and cable ties for connections with tubing. Moreover, some devices (*e.g.*, device 1-2) had leaks in the needle port that rendered them unusable. Coupled with the relative labor-intensiveness of the needle alignment process and the occurrence of slight alignment errors described above, these episodes foster the need for adoption of a fully automated fabrication process. Although such an improvement would prohibit using of blunt needles as the inner channels of the devices, the overall process could benefit from replacing blunt needles with 3D-printed inner channels whose dimensions could be modified on-demand (but considering the Objet 24 might not be able to print orifices smaller than 500 – 600 μm). Additionally, barbed connectors could be replaced with 3D-printed female Luer connectors potentially minimizing the occurrence of leaks.

The size distribution of the alginate capsules produced by either type of droplet generator was highly polydisperse, and occurrence of coalescence prior to gelation seemed to be responsible for these observations. However, X-ray imaging of 3D-printed droplet generators also revealed that all 3D-printed structures had rough surfaces (see figures in appendix B.1) that could have propitiated turbulent flow and the formation of eddies proximal to the alginate-oil interface. A potential solution is to increase the dimensions of the outer channels in 3D-printed droplet generators to ensure that, if present, turbulence transpires far from the alginate-oil

interface and does not interfere with droplet formation. Furthermore, wider outer channels would facilitate cleaning and adoption of a device fully fabricated by the 3D printer, especially if a coaxial flow geometry is implemented. A potential embodiment of the improved and fully 3D-printed droplet generators is shown in Figure 5.1.

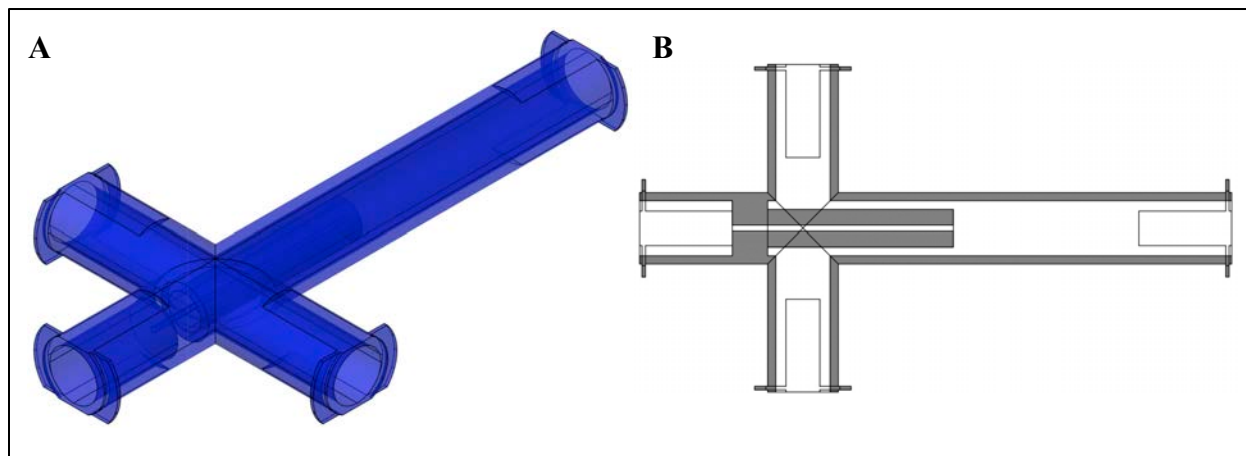


Figure 5.1. Design of a device to be fully fabricated with a 3D-printer.

(A) SW isometric view of X-ray rendering of a device with wider outer channel, 3D-printed inner channel, and female Luer connectors. (B) Cross-section of the same device. It would also be possible to design and fabricate 3D-printed droplet generators with male Luer locks for interconnection of two or more devices in series in order to generate core-shell and layered capsules.

In spite of the limited success of this study in attempting to adapt droplet generators for generation of 5% w/v alginate capsules via internal gelation; future studies could attempt to combine emulsification-internal gelation and encapsulation using droplet generators to tackle the problem of partial encapsulation that is inherent to both systems. A promising approach would be to generate batches of capsules through emulsification-internal gelation and then apply a second layer of alginate coating using a 3D-printed droplet generator.

Bibliography

- Akbari, S. & Pirbodaghi, T., 2013. Microfluidic encapsulation of cells in alginate particles via an improved internal gelation approach. *Microfluidics and Nanofluidics*, 16(4), pp.773–777.
- Baroud, C.N., Gallaire, F. & Dangla, R., 2010. Dynamics of microfluidic droplets. *Lab on a Chip*, 10(16), pp.2032–45.
- Van Belle, T. & Von Herrath, M., 2008. Immunosuppression in islet transplantation. *Journal of Clinical Investigation*, 118(5), pp.1625–1628.
- Berney, T. *et al.*, 2004. Immunosuppression for pancreatic islet transplantation. *Transplantation Proceedings*, 36(2), pp.362–366.
- Berthier, J. *et al.*, 2010. Highly viscous fluids in pressure actuated flow focusing devices. *Sensors and Actuators A*, 158(1), pp.140–148.
- Bonner-Weir, S. *et al.*, 2000. *In vitro* cultivation of human islets from expanded ductal tissue. *Proceedings of the National Academy of Sciences of the United States of America*, 97(14), pp.7999–8004.
- Canadian Diabetes Association, Types of Diabetes. Available at: <http://www.diabetes.ca/about-diabetes/what-is-diabetes> [Accessed February 9, 2015].
- Capretto, L. *et al.*, 2008. Effect of the gelation process on the production of alginate microbeads by microfluidic chip technology. *Lab on a Chip*, 8(4), pp.617–21.
- Choi, C.-H. *et al.*, 2007. Generation of monodisperse alginate microbeads and in situ encapsulation of cell in microfluidic device. *Biomedical Microdevices*, 9(6), pp.855–62.
- Christopher, G.F. & Anna, S.L., 2007. Microfluidic methods for generating continuous droplet streams. *Journal of Physics D: Applied Physics*, 40(19), pp.R319–R336.
- Conover, W.J. & Iman, R.L., 1981. Rank transformations as a bridge between parametric and nonparametric statistics. *American Statistician*, 35(3), pp.124–9.
- Elliott, R.B. *et al.*, 2005. Transplantation of micro- and macroencapsulated piglet islets into mice and monkeys. In *Transplantation Proceedings*. pp. 466–469.
- Emamaullee, J.A. *et al.*, 2006. Neonatal porcine islets exhibit natural resistance to hypoxia-induced apoptosis. *Transplantation*, 82(7), pp.945–52.

- Eriksson, A.U. *et al.*, 2013. Near infrared optical projection tomography for assessments of β -cell mass distribution in diabetes research. *Journal of Visualized Experiments*, 3001(January), p.e50238.
- Fawcett, R.F. & Salter, K.C., 1984. A monte carlo study of the f test and three tests based on ranks of treatment effects in randomized block designs. *Communications in Statistics: Simulation and Computation*, 13(2), pp.213–25.
- Findlater, L. *et al.*, 2009. Ephemeral Adaptation: The Use of Gradual Onset to Improve Menu Selection Performance. In *Proceedings of the ACM Conference on Human Factors in Computer Systems*. pp. 1655–1664.
- Garstecki, P., Stone, H. & Whitesides, G., 2005. Mechanism for Flow-Rate Controlled Breakup in Confined Geometries: A Route to Monodisperse Emulsions. *Physical Review Letters*, 94(16), p.164501.
- Hering, B.J. & Walawalkar, N., 2009. Pig-to-nonhuman primate islet xenotransplantation. *Transplant Immunology*, 21(2), pp.81–86.
- Higgins, J.J., Blair, R.C. & Tashtoush, S., 1990. The aligned rank transform procedure. In *Proceedings of the Conference on Applied Statistics in Agriculture*. pp. 185–195.
- Higgins, J.J. & Tashtoush, S., 1994. An aligned rank transform test for interaction. *Nonlinear World* 1, 2, pp.201–11.
- Hoesli, C., 2010. *Bioprocess development for cell-based treatment of diabetes*. University of British Columbia.
- Hoesli, C.A. *et al.*, 2011. Pancreatic cell immobilization in alginate beads produced by emulsion and internal gelation. *Biotechnology and Bioengineering*, 108(2), pp.424–34.
- Hoesli, C.A. *et al.*, 2012. Reversal of diabetes by β TC3 cells encapsulated in alginate beads generated by emulsion and internal gelation. *Journal of Biomedical Materials Research Part B: Applied Biomaterials*, 100(4), pp.1017–28.
- Kang, E. *et al.*, 2010. Novel PDMS cylindrical channels that generate coaxial flow, and application to fabrication of microfibers and particles. *Lab on a Chip*, 10(14), pp.1856–61.
- Kelly, W.D. *et al.*, 1967. Allograft transplantation of the pancreas and the duodenum along with the kidney in diabetic nephropathy. *Surgery*, 61(8), pp.827–37.
- Korbitt, G.S. *et al.*, 1996. Large scale isolation, growth, and function of porcine neonatal islet cells. *Journal of Clinical Investigation*, 97(9), pp.2119–29.

- Kroon, E.J. *et al.*, 2008. Pancreatic endoderm derived from human embryonic stem cells generates glucose-responsive insulin-secreting cells *in vivo*. *Nature Biotechnology*, 26(4), pp.443–452.
- De la Tour, D.D. *et al.*, 2001. Beta-cell differentiation from a human pancreatic cell line *in vitro* and *in vivo*. *Molecular Endocrinology (Baltimore, Md.)*, 15(3), pp.476–483.
- Lamb, M. *et al.*, 2011. Function and viability of human islets encapsulated in alginate sheets: *in vitro* and *in vivo* culture. *Transplantation Proceedings*, 43(9), pp.3265–6.
- Lamprecht, A., Schäfer, U.F. & Lehr, C.-M., 2000. Characterization of microcapsules by confocal laser scanning microscopy: structure, capsule wall composition and encapsulation rate. *European Journal of Pharmaceutics and Biopharmaceutics*, 49(1), pp.1–9.
- Lee, K.Y. *et al.*, 2000. Controlling Mechanical and Swelling Properties of Alginate Hydrogels Independently by Cross-Linker Type and Cross-Linking Density. *Macromolecules*, 33(11), pp.4291–4294.
- Lee, S.-H. *et al.*, 2009. Human beta-cell precursors mature into functional insulin-producing cells in an immunoisolation device: implications for diabetes cell therapies. *Transplantation*, 87(7), pp.983–991.
- Lee, W., Walker, L.M. & Anna, S.L., 2009. Role of geometry and fluid properties in droplet and thread formation processes in planar flow focusing. *Physics of Fluids*, 21(3), p.032103.
- Lv, G. *et al.*, 2009. Permeability changes of the cell-contained microcapsules visualized by confocal laser scanning microscope. *Journal of Biomedical Materials Research Part A*, 90(3), pp.773–83.
- Ma, M. *et al.*, 2013. Core-shell hydrogel microcapsules for improved islets encapsulation. *Advanced Healthcare Materials*, 2(5), pp.667–72.
- Mansell, K. & Arnason, T., 2015. Endocrine and Metabolic Disorders: Diabetes Mellitus. In J. Gray, ed. *e-Therapeutics [Internet]*. Ottawa, ON: Canadian Pharmacist Association.
- Marigliano, M. *et al.*, 2011. Pig-to-nonhuman primates pancreatic islet xenotransplantation: An overview. *Current Diabetes Reports*, 11(5), pp.402–412.
- Mathers, C.D. & Loncar, D., 2006. Projections of global mortality and burden of disease from 2002 to 2030. *PLoS Medicine*, 3(11), pp.2011–2030.
- Mcdonald, J.C. *et al.*, 2000. Fabrication of microfluidic systems in poly (dimethylsiloxane). *Electrophoresis*, 21(1), pp.27–40.

- Melchels, F.P.W., Feijen, J. & Grijpma, D.W., 2010. A review on stereolithography and its applications in biomedical engineering. *Biomaterials*, 31(24), pp.6121–6130.
- Miyazaki, J. *et al.*, 1990. Establishment of a pancreatic beta cell line that retains glucose-inducible insulin secretion: special reference to expression of glucose transporter isoforms. *Endocrinology*, 127(1), pp.126–32.
- Mizutani, R. & Suzuki, Y., 2012. X-ray microtomography in biology. *Micron*, 43(2-3), pp.104–115.
- Monzo, A., Bonn, G.K. & Guttman, A., 2007. Lectin-immobilization strategies for affinity purification and separation of glycoconjugates. *Trends in Analytical Chemistry*, 26(5), pp.423–432.
- Morimoto, Y., Tan, W.-H. & Takeuchi, S., 2009. Three-dimensional axisymmetric flow-focusing device using stereolithography. *Biomedical Microdevices*, 11(2), pp.369–377.
- Morris, E.R. *et al.*, 1981. Concentration and shear rate dependence of viscosity in random coil polysaccharide solutions. *Carbohydrate Polymers*, 1, pp.5–21.
- Owusu-Apenten, R.K., 2005. Principles of Food Rheology. In *Introduction to Food Chemistry*. Boca Raton, FL: CRC Press, pp. 132–138.
- Pagliuca, F.W. *et al.*, 2014. Generation of Functional Human Pancreatic beta Cells *In Vitro*. *Cell*, 159(2), pp.428–439.
- Piper, M., Seidenfeld, J. & Aronson, N., 2004. *Islet Transplantation in Patients with Type 1 Diabetes Mellitus*, Rockville, MD.
- Pisania, A., 2007. *Development of Quantitative Methods for Quality Assessment of Islets of Langerhans*. Massachusetts Institute of Technology.
- Poncelet, D. *et al.*, 1995. Production of alginate beads by emulsification/internal gelation. II. Physicochemistry. *Applied Microbiology and Biotechnology*, 43, pp.644–650.
- Rezania, A. *et al.*, 2011. Production of Functional Glucagon-Secreting [alpha]-Cells From Human Embryonic Stem Cells. *Diabetes*, 60(1), pp.239–47.
- Rezania, A. *et al.*, 2014. Reversal of diabetes with insulin-producing cells derived *in vitro* from human pluripotent stem cells. *Nature Biotechnology*, 32(11), pp.1121–33.
- Robertson, R.P., 2004. Islet transplantation as a treatment for diabetes - a work in progress. *New England Journal of Medicine*, 350(7), pp.694–705.

- Russell, S.J. *et al.*, 2014. Outpatient Glycemic Control with a Bionic Pancreas in Type 1 Diabetes. *New England Journal of Medicine*, 371, pp.313–325.
- Ryan, E.A. *et al.*, 2005. Five-year follow-up after clinical islet transplantation. *Diabetes*, 54(7), pp.2060–2069.
- Sakai, S. *et al.*, 2004. Preparation of mammalian cell-enclosing subsieve-sized capsules (<100 μm) in a coflowing stream. *Biotechnology and Bioengineering*, 86(2), pp.168–73.
- Salter, K.C. & Fawcett, R.F., 1985. A robust and powerful rank test of treatment effects in balanced incomplete block designs. *Communications in Statistics: Simulation and Computation*, 14(4), pp.807–28.
- Salter, K.C. & Fawcett, R.F., 1993. The ART test of interaction: a robust and powerful rank test of interaction in factorial models. *Communications in Statistics: Simulation and Computation*, 22(1), pp.137–53.
- Schulz, T.C. *et al.*, 2012. A scalable system for production of functional pancreatic progenitors from human embryonic stem cells. *PloS One*, 7(5), p.e37004.
- Seemann, R. *et al.*, 2012. Droplet based microfluidics. *Reports on Progress in Physics*, 75(1).
- Shapiro, A.M.J. *et al.*, 2000. Islet Transplantation in Seven Patients with Type I Diabetes Mellitus Using a Glucocorticoid-free Immunosuppressive Regimen. *New England Journal of Medicine*, 343(4), pp.230–238.
- Sharpe, J., 2003. Optical projection tomography as a new tool for studying embryo anatomy. *Journal of Anatomy*, 202(2), pp.175–81.
- Sharpe, J. *et al.*, 2002. Optical projection tomography as a tool for 3D microscopy and gene expression studies. *Science*, 296(5567), pp.541–5.
- Skoog, S.A., Goering, P.L. & Narayan, R.J., 2014. Stereolithography in tissue engineering. *Journal of Materials Science: Materials in Medicine*, 25(3), pp.845–856.
- Skyler, J.S., 2004. DCCT: the study that forever changed the nature of treatment of type 1 diabetes. *British Journal of Diabetes & Vascular Disease*, 4(1), pp.29–32.
- Sogayar, M.C. *et al.*, 2005. Diabetes mellitus: new therapeutic approaches to treat an old disease. *Revista de Ciências Farmacêuticas Básica e Aplicada*, 26(1), pp.1–8.
- Sörenby, A.K. *et al.*, 2008. Preimplantation of an immunoprotective device can lower the curative dose of islets to that of free islet transplantation: studies in a rodent model. *Transplantation*, 86(2), pp.364–366.

- Souza, Y.E.D.M. de *et al.*, 2011. Islet Transplantation in Rodents. Do encapsulated islets really work? *Arquivos de Gastroenterologia*, 48(2), pp.146–152.
- Statistics Canada, 2013. Diabetes, 2013. *Health Fact Sheets (82-625-X)*. Available at: <http://www.statcan.gc.ca/pub/82-625-x/2014001/article/14016-eng.htm> [Accessed February 9, 2015].
- Storrs, R.W. *et al.*, 2001. Preclinical development of the Islet Sheet. *Annals of the New York Academy of Sciences*, 944, pp.252–66.
- Strand, B.L. *et al.*, 2003. Visualization of alginate-poly-L-lysine-alginate microcapsules by confocal laser scanning microscopy. *Biotechnology and bioengineering*, 82(4), pp.386–94.
- Sutherland, D.E. *et al.*, 2001. Lessons learned from more than 1,000 pancreas transplants at a single institution. *Annals of Surgery*, 233(4), pp.463–501.
- Sutherland, D.E. *et al.*, 1987. Pancreas transplant protocols at the University of Minnesota: recipient and donor selection, operative and postoperative management, and outcome. *Clinical Transplants*, pp.109–26.
- Sweet, I.R. *et al.*, 2008. Treatment of diabetic rats with encapsulated islets. *Journal of Cellular and Molecular Medicine*, 12(6B), pp.2644–2650.
- Takeuchi, S. *et al.*, 2005. An Axisymmetric Flow-Focusing Microfluidic Device. *Advanced Materials*, 17(8), pp.1067–1072.
- Tan, W.-H. & Takeuchi, S., 2007. Monodisperse Alginate Hydrogel Microbeads for Cell Encapsulation. *Advanced Materials*, 19(18), pp.2696–2701.
- Tan, Y.-C., Cristini, V. & Lee, A.P., 2006. Monodispersed microfluidic droplet generation by shear focusing microfluidic device. *Sensors and Actuators B*, 114(1), pp.350–356.
- Tendulkar, S. *et al.*, 2012. A three-dimensional microfluidic approach to scaling up microencapsulation of cells. *Biomedical Microdevices*, 14(3), pp.461–9.
- Umbanhowar, P.B., Prasad, V. & Weitz, D. a., 2000. Monodisperse emulsion generation via drop break off in a coflowing stream. *Langmuir*, 16(4), pp.347–351.
- Vaithilingam, V. & Tuch, B.E., 2011. Islet transplantation and encapsulation: an update on recent developments. *Review of Diabetic Studies*, 8(1), pp.51–67.
- De Vos, P. *et al.*, 1996. Association Between Capsule Diameter, Adequacy of Encapsulation, and Survival of Microencapsulated Rat Islet Allografts. *Transplantation*, 62(October), pp.893–899.

- Walls, J.R. *et al.*, 2005. Correction of artefacts in optical projection tomography. *Physics in Medicine and Biology*, 50(19), pp.4645–65.
- Ward, T. *et al.*, 2005. Microfluidic flow focusing: drop size and scaling in pressure versus flow-rate-driven pumping. *Electrophoresis*, 26(19), pp.3716–24.
- Wiedemeier, S. *et al.*, 2011. Encapsulation of Langerhans' islets: Microtechnological developments for transplantation. *Engineering in Life Sciences*, 11(2), pp.165–173.
- Wobbrock, J.O. *et al.*, 2011. The Aligned Rank Transform for Nonparametric Factorial Analyses Using Only ANOVA Procedures. In *Proceedings of the ACM Conference on Human Factors in Computer Systems*. Vancouver, BC, Canada: ACM Press, pp. 143–146.
- World Health Organization, 2014. *Global status report on noncommunicable diseases 2014*, Geneva, World Health Organization.
- Yang, Z. *et al.*, 2002. Survival of pancreatic islet xenografts in NOD mice with the theracyte device. *Transplantation Proceedings*, 34(8), pp.3349–3350.
- Zhou, C., Yue, P. & Feng, J.J., 2006. Formation of simple and compound drops in microfluidic devices. *Physics of Fluids*, 18(9), p.092105.

Appendices

Appendix A - Supplementary methods

A.1 ImageJ script of macro for needle alignment image analysis

This macro was used on the images of the x-ray scanned devices to generate a table containing the coordinates of the centers of mass of the needle and the concentric ensemble. Programmer comments appear in italics and are preceded by two forward slashes (*//*).

```
//Transform RGB image into 8-bit image
run("8-bit");
run("Set Measurements...", "area center stack redirect=None decimal=9");
//Transform 8-bit images in the Z-stack to binary images. Turn pixels with intensity values //greater than 60 to black pixels
setAutoThreshold("Default");
//run("Threshold...");
setAutoThreshold("Default dark stack");
setThreshold(60, 255);
//Run "Analyze Particles" plug-in. Record masks corresponding to size of the needle in region of //interest manager
run("Analyze Particles...", "size=0.2-1.6 circularity=0.6-1 exclude clear include add stack");
// Turn pixels with intensity values between 40 and 60 to black pixels
//run("Threshold...");
setThreshold(40, 60);
//Run "Analyze Particles" plug-in. Record masks corresponding to size of the cylinder //ensemble in the region of interest manager.
run("Analyze Particles...", "size=18-20 circularity=0.599-1.00 exclude include add stack");
//Measure the X and Y coordinates of the center of mass of all masks in the region of interest //manager. Output center of mass coordinates, slice number and mask area.
roiManager("Measure");
```

In some cases, the pixel granularity and/or starburst artifacts complicated the distinction between the concentric ensemble and the background, and the macro did not record any regions of interest. For these stacks, the following supplementary macro was used:

```
//Transform RGB image into 8-bit image
run("8-bit");
run("Set Measurements...", "area center stack redirect=None decimal=9");
//Transform 8-bit images in the Z-stack to binary images. Turn pixels with intensity values //greater than 60 to black pixels
setAutoThreshold("Default");
//run("Threshold...");
setAutoThreshold("Default dark stack");
setThreshold(60, 255);
```

```
//Run "Analyze Particles" plug-in. Record masks corresponding to size of the needle in the //region of interest manager.  
run("Analyze Particles...", "size=0.2-1.6 circularity=0.6-1 exclude clear include add stack");  
//Transform 8-bit images in the Z-stack to binary images. Turn pixels with intensity values //between 40 and 60 to black pixels  
//run("Threshold...");  
setThreshold(40, 60);  
//Isolate masks of cylinder ensembles from the edges.  
run("Convert to Mask")  
run("Close-", "stack");  
//run("Erode", "stack");  
//run("Erode", "stack");  
//Run "Analyze Particles" plug-in. Record masks corresponding to size of the cylinder //ensemble in the region of interest manager.  
run("Analyze Particles...", "size=18-20 circularity=0.599-1.00 exclude include add stack");  
//Measure the X and Y coordinates of the center of mass of all masks in the region of interest //manager. Output center of mass coordinates, slice number and mask area.  
roiManager("Measure");
```

A.2 Excel VBA script of macro for needle alignment analysis

This macro was used for collating the result tables from the ImageJ macros using the slice number and mask area as the sorting criteria. Only cross-sections containing both masks were considered for analysis. Programmer comments appear in italics and are preceded by a single apostrophe (‘).

```
Sub Needle_Alignment_Analysis()
    Application.ScreenUpdating = False
    'Print headers
    Range("G1").Value = "Needle"
    Range("J1").Value = "Device"
    Range("M1").Value = "Delta"
    Range("O1").Value = "Absolute"
    Range("Q1").Value = "Difference in CoM"
    Range("G2,J2").Value = "Slice"
    Range("H2,K2,M2,O2").Value = "CoM - X"
    Range("I2,L2,N2,P2").Value = "CoM - Y"
    'In column E (slice number), find the last cell containing a value
    lastrow = Range("E" & Rows.Count).End(xlUp).Row
    'Sort the data in ascending slice number
    Columns("A:E").Select
    ActiveSheet.Sort.SortFields.Clear
    ActiveSheet.Sort.SortFields.Add Key:=Range( _
        "E2", Cells(lastrow, 5)), SortOn:=xlSortOnValues, Order:=xlAscending, DataOption:= _
        xlSortNormal
    With ActiveSheet.Sort
        .SetRange Range("A1", Cells(lastrow, 5))
        .header = xlYes
        .MatchCase = False
        .Orientation = xlTopToBottom
        .SortMethod = xlPinYin
        .Apply
    End With
    'For every entry, check the area of the mask. Copy the slice number and the coordinates of the center of mass if the
    'area is less than 18, and the current slice number is the same as the slice number in the row below; or if the area
    'is greater than 18, and the current slice number is the same as the slice number in the row above.
    For i = 1 To lastrow
        A = Cells(1 + i, 2).Value
        s = Cells(1 + i, 5).Value
        nextS = Cells(2 + i, 5).Value
        prevS = Cells(i, 5).Value
        If A < 18 And s = nextS Then
            Range("G" & Rows.Count).End(xlUp).Offset(1) = Cells(1 + i, 5).Value
            Range("H" & Rows.Count).End(xlUp).Offset(1) = Cells(1 + i, 3).Value
            Range("I" & Rows.Count).End(xlUp).Offset(1) = Cells(1 + i, 4).Value
        Else
            If s = prevS Then
                Range("J" & Rows.Count).End(xlUp).Offset(1) = Cells(1 + i, 5).Value
            End If
        End If
    Next i
End Sub
```

```

    Range("K" & Rows.Count).End(xlUp).Offset(1) = Cells(1 + i, 3).Value
    Range("L" & Rows.Count).End(xlUp).Offset(1) = Cells(1 + i, 4).Value
End If
End If
Next i
In column G (copied values of slices that contain both objects), find the last cell containing a value
lastrow2 = Range("G" & Rows.Count).End(xlUp).Row
For every slice that contains both objects, calculate the difference between center of mass coordinates of the
objects, and the concentricity error between centers of mass using the absolute values of the differences.
Range("m3").formula = "=k3-h3"
Range("n3").formula = "=l3-i3"
Range("o3").formula = "=abs(m3)"
Range("p3").formula = "=abs(n3)"
Range("q3").formula = "=SQRT(O3^2+P3^2)"
Range("m3:q3").AutoFill Destination:=Range("m3", Cells(lastrow2, 17))
Application.ScreenUpdating = True
End Sub

```

A.3 Script of ImageJ macro for particle size distribution image analysis

This macro was used on the images of alginate particles in a dish to generate a table containing the projected areas of the alginate particles. Programmer comments appear in italics and are preceded by “//” symbol.

```
//Transform RGB image into 8-bit image  
run("8-bit");  
//Transform 8-bit image to binary image. Turn pixels with intensity values less than 120  
//to black pixels  
setAutoThreshold("Default");  
//run("Threshold...");  
setThreshold(0, 120);  
run("Convert to Mask");  
//Separate adjacent masks  
run("Watershed");  
run("Fill Holes");  
run("Watershed");  
//Record the area, perimeter, circularity and feret's diameter of every mask  
run("Set Measurements...", "area perimeter shape feret's redirect=None decimal=3");  
//Run "Analyze Particles" plug-in  
run("Analyze Particles...", "size=30000-Infinity circularity=0.70-1.00 show=Outlines display exclude include  
in_situ");  
//Plot the distribution of areas of the binary masks  
run("Distribution...", "parameter=Area automatic");
```

A.4 R script of statistical analysis for effects of outer flow rate and design geometry on alginate bead size and polydispersity

This program was used for statistical analysis of the particle size distributions generated in eleven devices with four different geometries at three different flow rates. The statistical analysis consisted of orthogonal Friedman tests, and mixed ANOVA on data transformed using the simple rank transform by columns or the aligned rank transform. Post-hoc analyses were conducted when appropriate using pairwise comparisons using Tukey's honest significance difference test. Programmer comments appear in italics and are preceded by a pound (#) sign. Descriptive statistics of the distributions were calculated as described in section 2.6 and summarized in a separate spreadsheet that was exported as a standard comma separated file (.csv). The file was loaded into R, but in the following script, the file path was replaced with the actual data.

To avoid bias due to complete case analysis, Friedman tests required generation of two sets of 27 data frames with complete cases, which were generated on Excel, and exported to R as comma separated files. From the original file described in the preceding paragraph, the data set corresponding to the first factor (*i.e.*, outer flow rate) was generated by removing one entry from designs 2 – 4 to achieve a balanced design (*i.e.*, same number of replicates in each cell), then the process was repeated for all possible combinations. For design geometry, the second data set was generated from the first data set by calculating the median of replicates in each cell. This step was necessary because Friedman tests between groups require unreplicated data.

```
# Load data
alldata<-read.table(header=T,sep=" ",text="subject,design,flow,freq,d20,iq20,d43,iq43,
1,1,30,236,493,362,878,133,
1,1,40,421,445,305,729,58,
1,1,50,343,472,370,801,265,
2,1,30,313,468,373,881,147,
```

```

2,1,40,269,536,230,984,231,
2,1,50,341,515,201,744,139,
3,2,30,121,765,277,1142,432,
3,2,40,128,600,250,951,400,
3,2,50,160,685,241,1129,468,
4,2,30,203,578,351,1056,438,
4,2,40,290,517,205,871,418,
4,2,50,311,477,282,827,374,
5,2,30,321,476,284,851,181,
5,2,40,409,438,274,789,112,
5,2,50,263,575,170,736,38,
6,3,30,161,615,274,950,114,
6,3,40,474,413,229,821,167,
6,3,50,214,592,270,888,80,
7,3,30,225,545,243,972,261,
7,3,40,222,623,346,829,50,
7,3,50,288,606,180,745,66,
8,3,30,312,481,380,963,309,
8,3,40,231,584,288,849,131,
8,3,50,229,571,254,840,235,
9,4,30,143,693,247,963,125,
9,4,40,178,647,314,1006,374,
9,4,50,92,727,212,881,235,
10,4,30,128,808,209,909,46,
10,4,40,174,748,202,855,98,
10,4,50,204,727,142,807,86,
11,4,30,188,683,262,882,40,
11,4,40,295,599,293,817,84,
11,4,50,387,566,225,737,78"
)

```

```

# Load Aligned rank Transform (ART) library
# Requires "lme4" and "car" libraries, which are used for analysis
library(ARTool);library(pbkrtest)

```

```

# FRIEDMAN TESTS

```

```

# Set working directory

```

```

setwd("~/Flow Data")

```

```

# Generate file names

```

```

files<-lapply(1:27,function(x){paste0("data",x,".csv")})

```

```

# Load files & confirm data is attached

```

```

load.file<-function(filename){d<-read.csv(filename,stringsAsFactors=FALSE)

```

```

  d

```

```

}

```

```

data<-lapply(files,load.file)

```

```

names(data)<-files

```

```

head(data$data1.csv)

```

```

# Run Friedman tests for flow

```

```

write.table(sapply(data,function(x) friedman.test(freq~flow|id,x)),file="1ffreq.csv",sep=",")

```

```

write.table(sapply(data,function(x) friedman.test(d20~flow|id,x)),file="1fd20.csv",sep=",")

```

```

write.table(sapply(data,function(x) friedman.test(d43~flow|id,x)),file="1fd43.csv",sep=",")

```

```

write.table(sapply(data,function(x) friedman.test(iq20~flow|id,x)),file="1fiq20.csv",sep=",")

```

```

write.table(sapply(data,function(x) friedman.test(iq43~flow|id,x)),file="1fiq43.csv",sep=",")

```

```

# Change working directory and load files with unreplicated data

```

```

setwd("~/Design Data")

```

```

data<-lapply(files,load.file)
names(data)<-files
# Run Friedman tests for design
write.table(sapply(data,function(x) friedman.test(freq~design|flow,x)),file="2ffreq.csv",sep=",")
write.table(sapply(data,function(x) friedman.test(d20~design|flow,x)),file="2fd20.csv",sep=",")
write.table(sapply(data,function(x) friedman.test(d43~design|flow,x)),file="2fd43.csv",sep=",")
write.table(sapply(data,function(x) friedman.test(iq20~design|flow,x)),file="2fiq20.csv",sep=",")
write.table(sapply(data,function(x) friedman.test(iq43~design|flow,x)),file="2fiq43.csv",sep=",")

# SIMPLE RANK TRANSFORM BY COLUMNS
# Apply simple rank transform to the data and create a data frame
# d43 stands for D[4,3]
# iq43 stands for the interquartile range of the volume-weighted distribution
# d20 stands for D[2,0]
# iq20 stands for the interquartile range of the number-weighted distribution
# freq stands for the number of alginate beads collected per minute
subject<-as.factor(alldata$subject)
design<-as.factor(alldata$design)
flow<-as.factor(alldata$flow)
riq43<-rank(alldata$d43)
rd20<-rank(alldata$d20)
rd43<-rank(alldata$d43)
riq20<-rank(alldata$iq20)
rfreq<-rank(alldata$freq)
rt.data<-data.frame(subject,design,flow,rt.freq)
# 2-way ANOVA with repeated measures in flow (a.k.a., 2-way split-plot-factorial ANOVA)
# between factor = design
# within factor = flow
# random effect = subject (i.e., each device)
# dependent variable = simple rank transform of d43
# assume possible interactions and report type II residuals
rt_d43<-lmer(rd43~design+design:flow+flow+(1|subject),rt.data)
Anova(rt_d43,type=2,test.statistic="F")

# 2-way ANOVA with repeated measures in flow (a.k.a., 2-way split-plot-factorial ANOVA)
# between factor = design
# within factor = flow
# random effect = subject (i.e., each device)
# dependent variable = simple rank transform of d20
# assume possible interactions and report type II residuals
rt_d20<-lmer(rd20~design+design:flow+flow+(1|subject),rt.data)
Anova(rt_d20,type=2,test.statistic="F")

# 2-way ANOVA with repeated measures in flow (a.k.a., 2-way split-plot-factorial ANOVA)
# between factor = design
# within factor = flow
# random effect = subject (i.e., each device)
# dependent variable = simple rank transform of iq43
# assume possible interactions and report type II residuals
rt_iq43<-lmer(riq43~design+design:flow+flow+(1|subject),rt.data)
Anova(rt_iq43,type=2,test.statistic="F")

# 2-way ANOVA with repeated measures in flow (a.k.a., 2-way split-plot-factorial ANOVA)

```

```

# between factor = design
# within factor = flow
# random effect = subject (i.e., each device)
# dependent variable = simple rank transform of iq20
# assume possible interactions and report type II residuals
rt_iq20<-lmer(riq20~design+design:flow+flow+(1|subject),rt.data)
Anova(rt_iq20,type=2,test.statistic="F")

# 2-way ANOVA with repeated measures in flow (a.k.a., 2-way split-plot-factorial ANOVA)
# between factor = design
# within factor = flow
# random effect = subject (i.e., each device)
# dependent variable = simple rank transform of freq
# assume possible interactions and report type II residuals
rt_freq<-lmer(rfreq~design+design:flow+flow+(1|subject),rt.data)
Anova(rt_freq,type=2,test.statistic="F")

# ALIGNED RANK TRANSFORM
# Create data frame for the ART
d43<-alldata$d43
d20<-alldata$d20
iq43<-alldata$iq43
iq20<-alldata$iq20
freq<-alldata$freq
art.data<-data.frame(subject,design,flow,d43,d20,iq43,iq20,freq)
# Apply ART to the data assuming a linear mixed model with interaction:
# Main effect 1 - design (Factor between groups)
# Main effect 2 - flow (Factor within groups)
# Random effect - subject (i.e., each device)
art_d43<-art(d43~design*flow+(1|subject),art.data)
art_d20<-art(d20~design*flow+(1|subject),art.data)
art_iq43<-art(iq43~design*flow+(1|subject),art.data)
art_iq20<-art(iq20~design*flow+(1|subject),art.data)
art_freq<-art(freq~design*flow+(1|subject),art.data)
# For every dependent variable there are 3 aligned responses
# A corresponding ANOVA is applied on each aligned response,
# and from the resulting ANOVA tables only the relevant effect is extracted
# In this case, type II residuals should be calculated because of unequal cell size
# NOTE: if transformation is appropriate, aligned responses should give F close to 0
anova(art_d43,response="aligned",type=2)
anova(art_d20,response="aligned",type=2)
anova(art_iq43,response="aligned",type=2)
anova(art_iq20,response="aligned",type=2)
anova(art_freq,response="aligned",type=2)
# 2-way ANOVA with repeated measures in flow (a.k.a., 2-way split-plot-factorial ANOVA)
# between factor = design
# within factor = flow
# random effect = subject (i.e., each device)
# dependent variable = aligned rank transform of d43
anova(art_d43,response="art",type=2,test="F")
# 2-way ANOVA with repeated measures in flow (a.k.a., 2-way split-plot-factorial ANOVA)
# between factor = design
# within factor = flow
# random effect = subject (i.e., each device)

```

```

# dependent variable = aligned rank transform of d20
anova(art_d20,response="art",type=2,test="F")
# 2-way ANOVA with repeated measures in flow (a.k.a., 2-way split-plot-factorial ANOVA)
# between factor = design
# within factor = flow
# random effect = subject (i.e., each device)
# dependent variable = aligned rank transform of iq43
anova(art_iq43,response="art",type=2,test="F")
# 2-way ANOVA with repeated measures in flow (a.k.a., 2-way split-plot-factorial ANOVA)
# between factor = design
# within factor = flow
# random effect = subject (i.e., each device)
# dependent variable = aligned rank transform of iq20
anova(art_iq20,response="art",type=2,test="F")
# 2-way ANOVA with repeated measures in flow (a.k.a., 2-way split-plot-factorial ANOVA)
# between factor = design
# within factor = flow
# random effect = subject (i.e., each device)
# dependent variable = aligned rank transform of freq
anova(art_freq,response="art",type=2,test="F")
# Load library for pairwise comparisons
library(lsmeans)
# Run pairwise comparisons only on statistical significant effects and variables
# In this case, only 'flow' was significant for d43 and iq20
lsmeans(artlm(art_d43,"flow"),pairwise~flow)
lsmeans(artlm(art_iq20,"flow"),pairwise~flow)
# Optional: Run pairwise comparisons on all factors for all variables? If so, remove pound signs two lines below;
# however, be aware of the inappropriateness of such analysis, the loss of statistical power and that Scheffé's test
# might be more applicable for running all possible contrasts.
#lsmeans(artlm(art_d20,"flow"),pairwise~flow)
#lsmeans(artlm(art_iq43,"flow"),pairwise~flow)
#lsmeans(artlm(art_d43,"design"),pairwise~design)
#lsmeans(artlm(art_d20,"design"),pairwise~design)
#lsmeans(artlm(art_iq43,"design"),pairwise~design)
#lsmeans(artlm(art_iq20,"design"),pairwise~design)

```

Appendix B - Supplementary figures

B.1 CT scans for needle alignment measurements

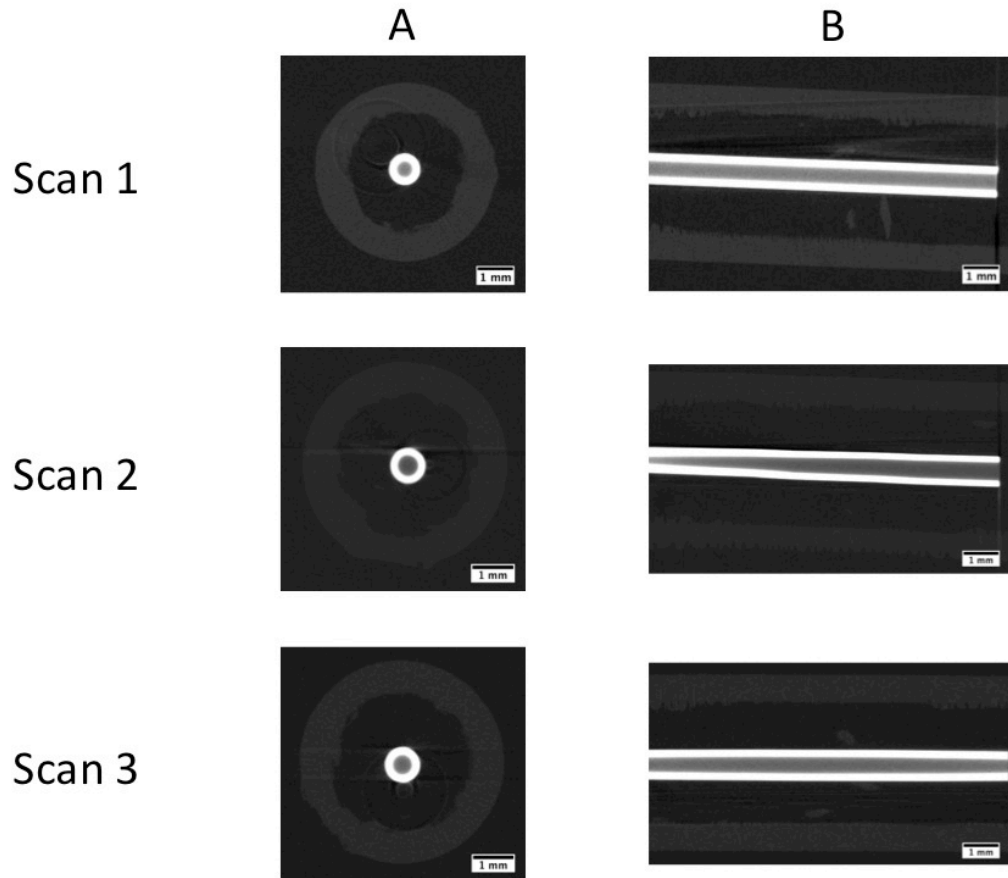


Figure B.1 Replicate CT scans of device 1-1.

(A) Representative cross-sectional views of concentric cylinder configuration in device 1-1. (B) Orthogonal view of reconstructed volumes.

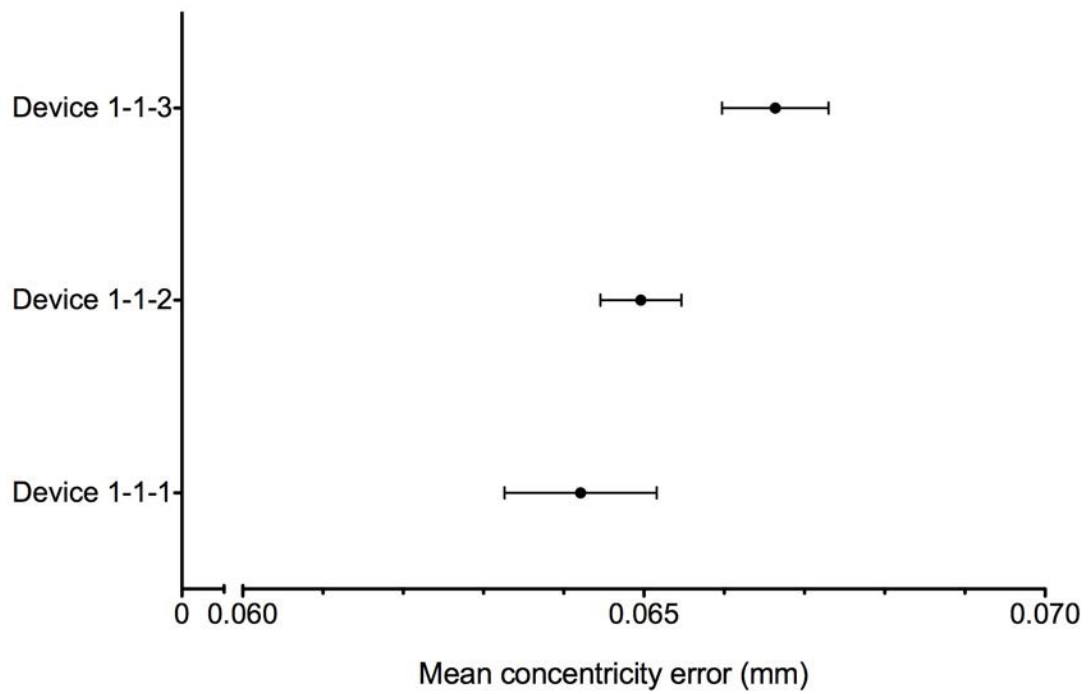


Figure B.2. Precision of concentricity error measurements in triplicate CT scans of device 1-1.

Arithmetic means of concentricity error in analyzed reconstructions. Error bars correspond to 95% confidence intervals. Numbering after “Device” corresponds to design, replicate and scan numbers respectively.

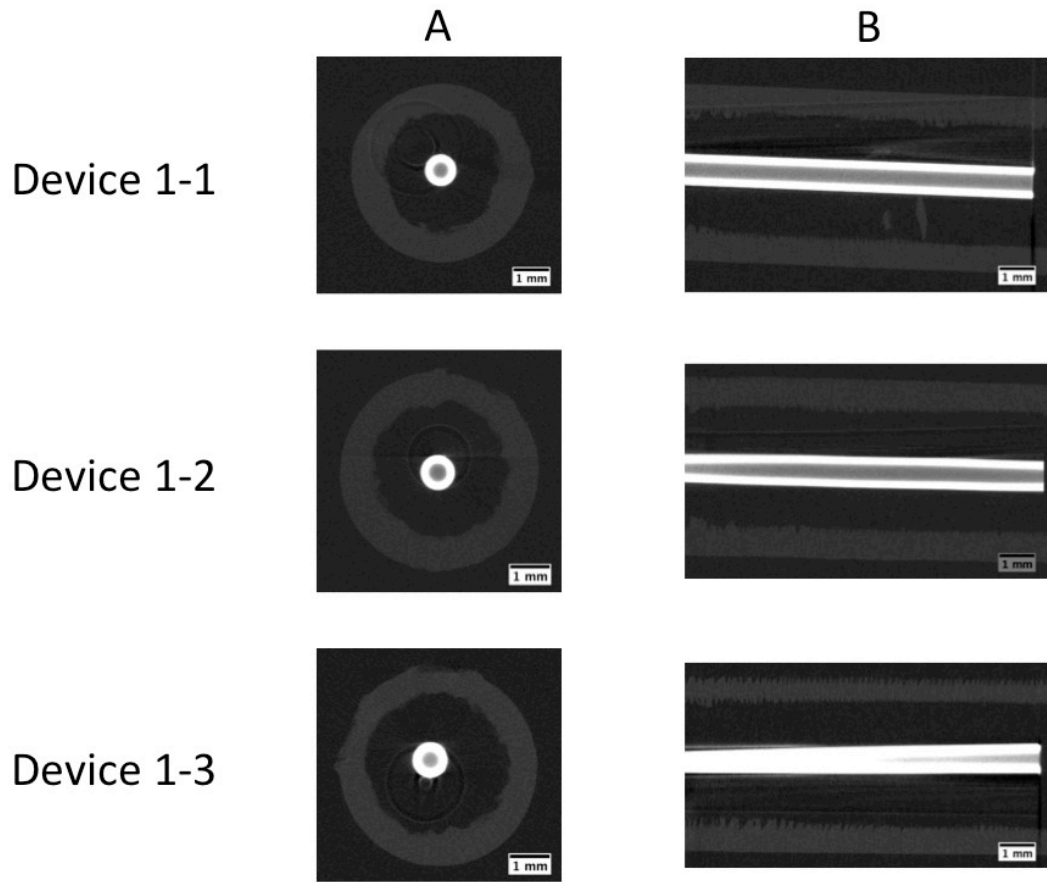


Figure B.3. CT scans of design 1.

(A) Representative cross-sectional views of concentric cylinder configuration in devices with design 1. (B) Orthogonal view of reconstructed volumes.

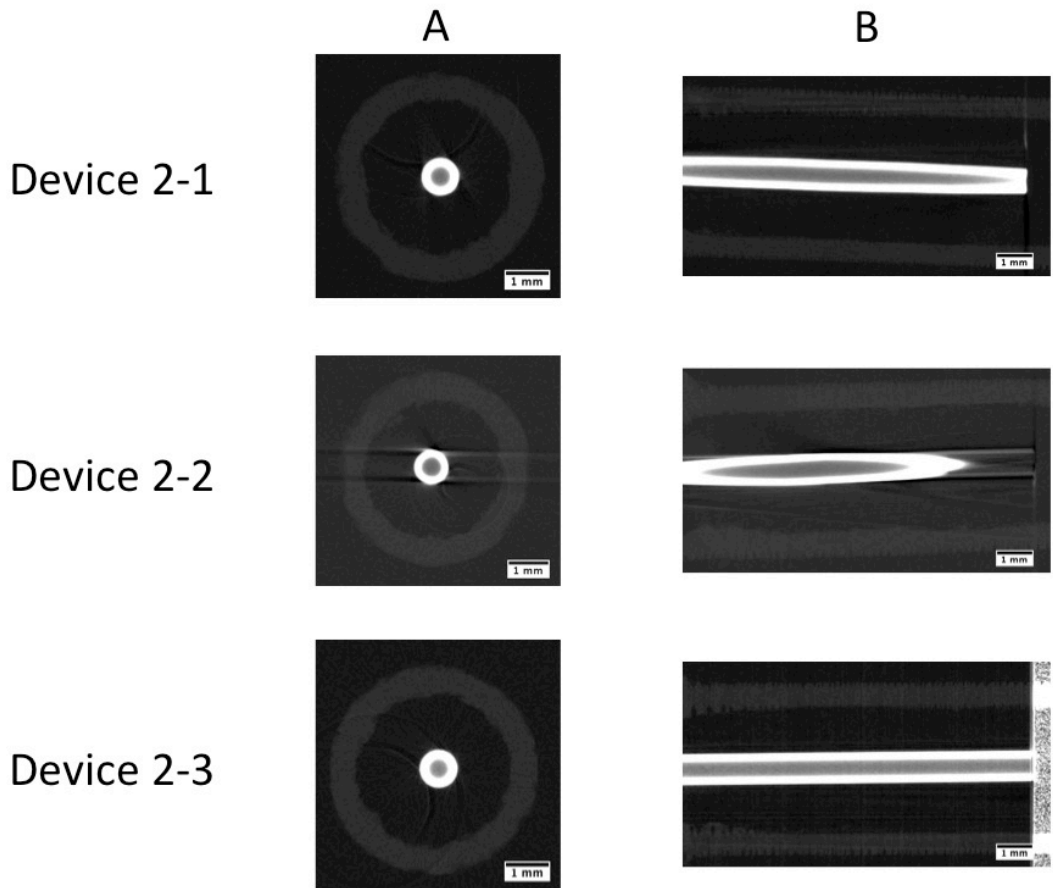


Figure B.4. CT scans of design 2.

(A) Representative cross-sectional views of concentric cylinder configuration in devices with design 2. (B) Orthogonal view of reconstructed volumes.

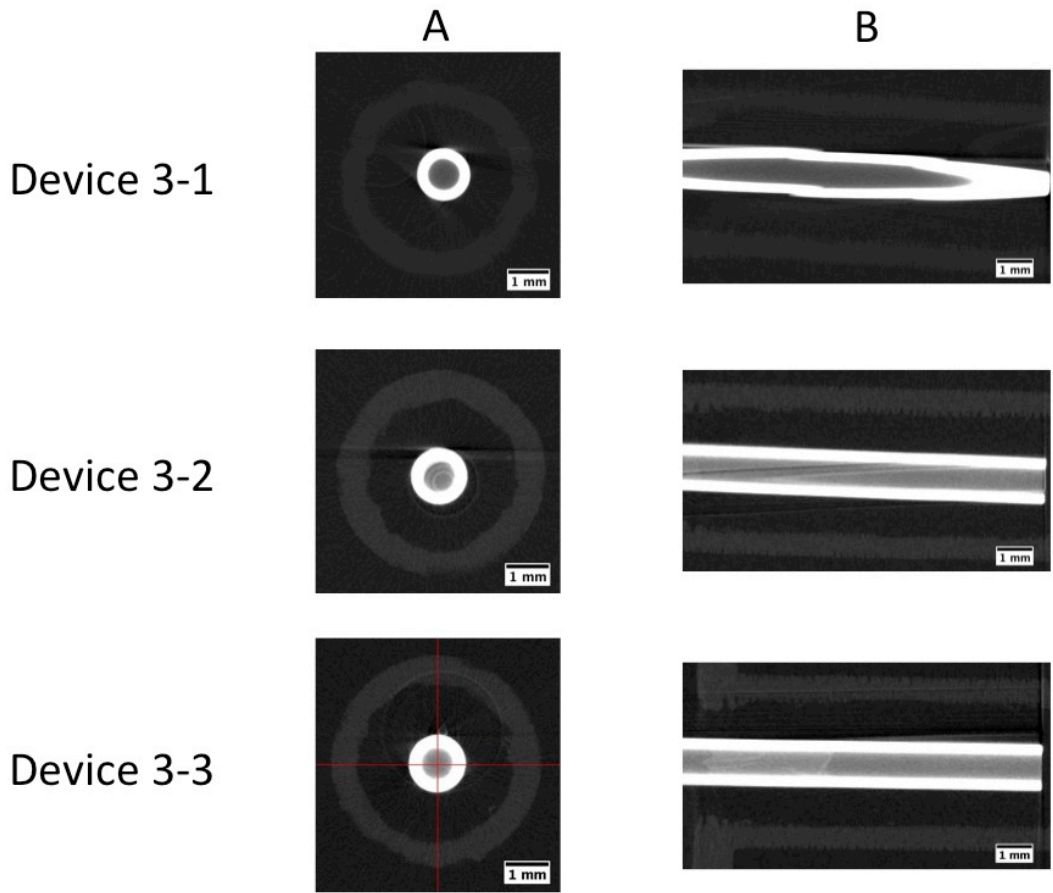


Figure B.5. CT scans of device 3.

(A) Representative cross-sectional views of concentric cylinder configuration in devices with design 3. (B) Orthogonal views of reconstructed volumes.

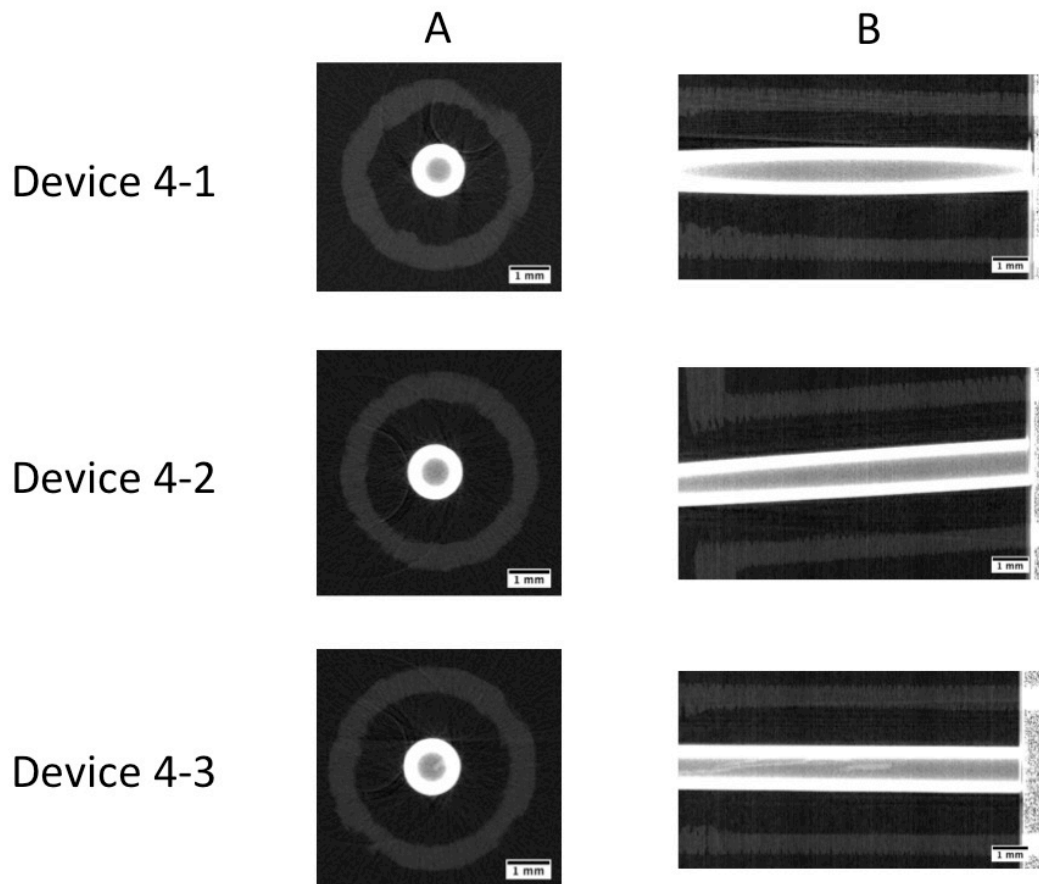


Figure B.6. CT scans of device 4.

(A) Representative cross-sectional views of concentric cylinder configuration in devices with design 4. (B) Orthogonal view of reconstructed volumes.

B.2 Histograms from particle size analysis in 3D printed devices

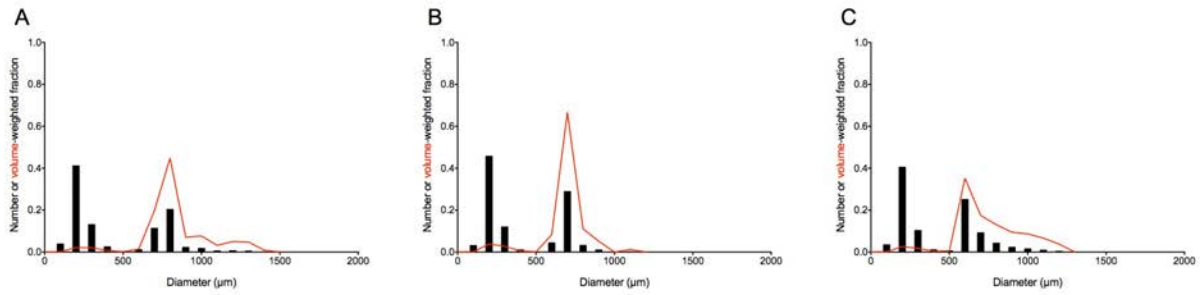


Figure B.7. Particle size distributions obtained with device 1-1.

Histograms of the number-weighted (black bars on left Y-axis) and volume-weighted alginate bead size distributions (red line on the right Y-axis) at outer flow rates of (A) 30 mL/min, (B) 40 mL/min and (C) 50 mL/min.

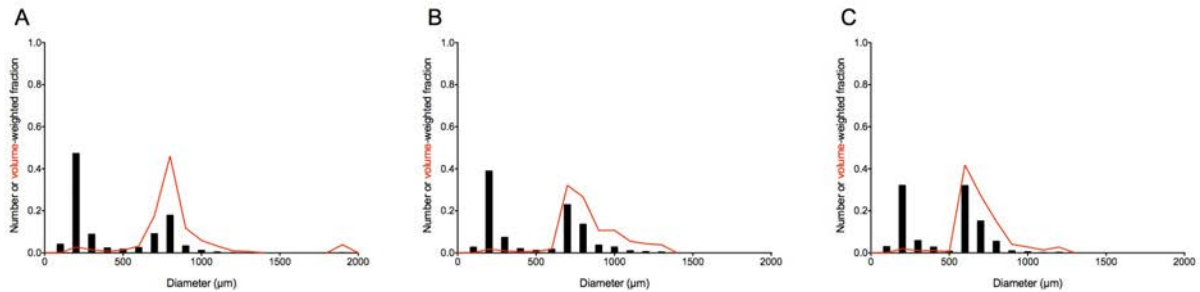


Figure B.8. Particle size distributions obtained with device 1-3.

Histograms of the number-weighted (black bars on left Y-axis) and volume-weighted alginate bead size distributions (red line on the right Y-axis) at outer flow rates of (A) 30 mL/min, (B) 40 mL/min and (C) 50 mL/min.

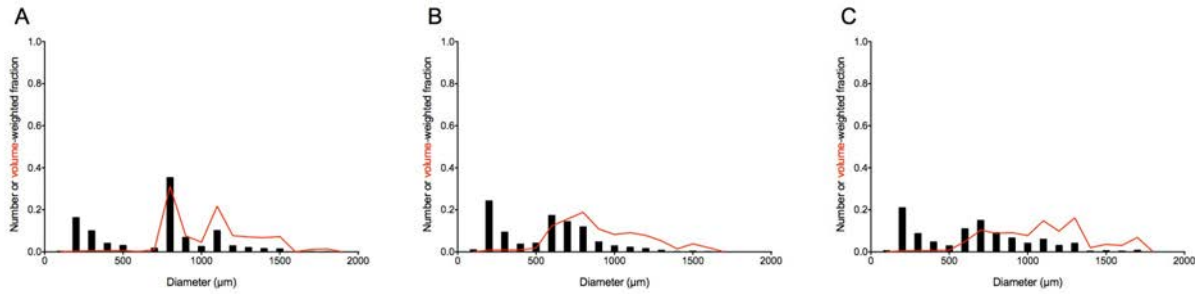


Figure B.9. Particle size distributions obtained with device 2-1.

Histograms of the number-weighted (black bars on left Y-axis) and volume-weighted alginate bead size distributions (red line on the right Y-axis) at outer flow rates of (A) 30 mL/min, (B) 40 mL/min and (C) 50 mL/min.

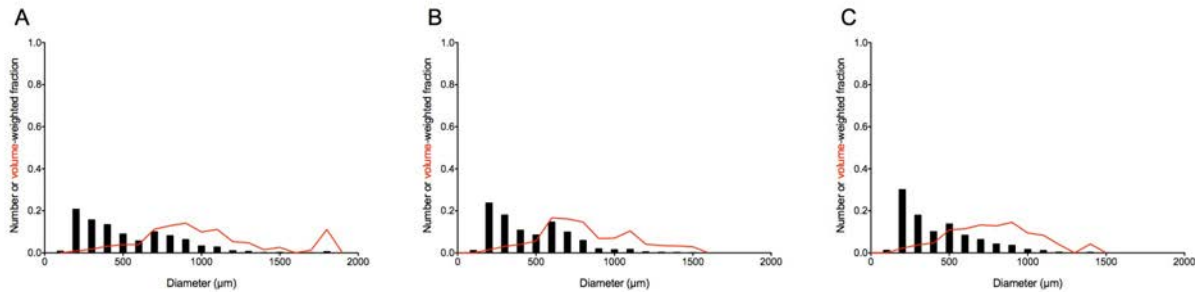


Figure B.10. Particle size distributions obtained with device 2-2.

Histograms of the number-weighted (black bars on left Y-axis) and volume-weighted alginate bead size distributions (red line on the right Y-axis) at outer flow rates of (A) 30 mL/min, (B) 40 mL/min and (C) 50 mL/min.

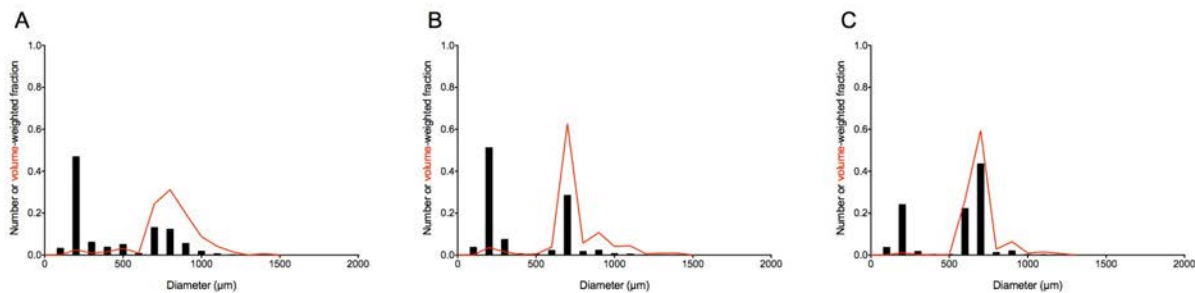


Figure B.11. Particle size distributions obtained with device 2-3.

Histograms of the number-weighted (black bars on left Y-axis) and volume-weighted alginate bead size distributions (red line on the right Y-axis) at outer flow rates of (A) 30 mL/min, (B) 40 mL/min and (C) 50 mL/min.

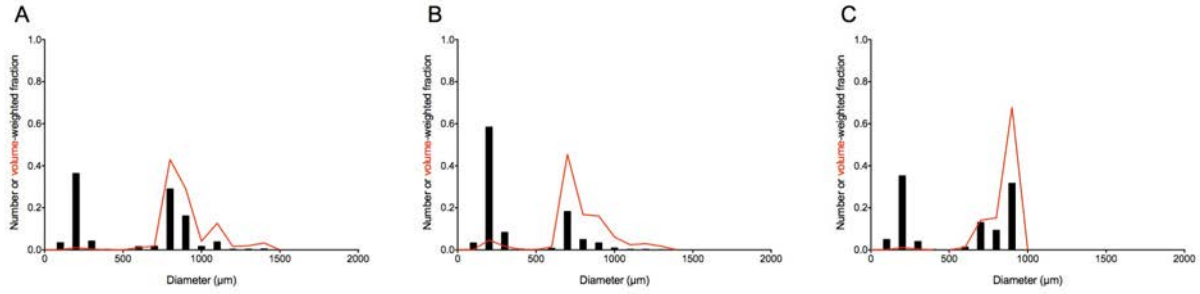


Figure B.12. Particle size distributions obtained with device 3-1.

Histograms of the number-weighted (black bars on left Y-axis) and volume-weighted alginate bead size distributions (red line on the right Y-axis) at outer flow rates of (A) 30 mL/min, (B) 40 mL/min and (C) 50 mL/min.

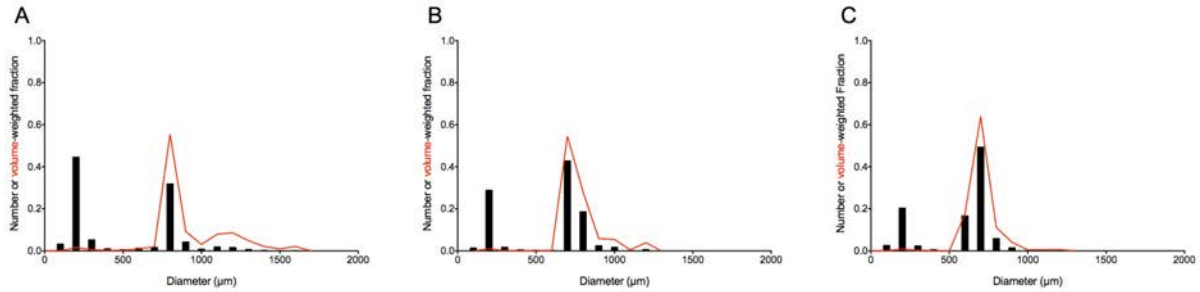


Figure B.13. Particle size distributions obtained with device 3-2.

Histograms of the number-weighted (black bars on left Y-axis) and volume-weighted alginate bead size distributions (red line on the right Y-axis) at outer flow rates of (A) 30 mL/min, (B) 40 mL/min and (C) 50 mL/min.

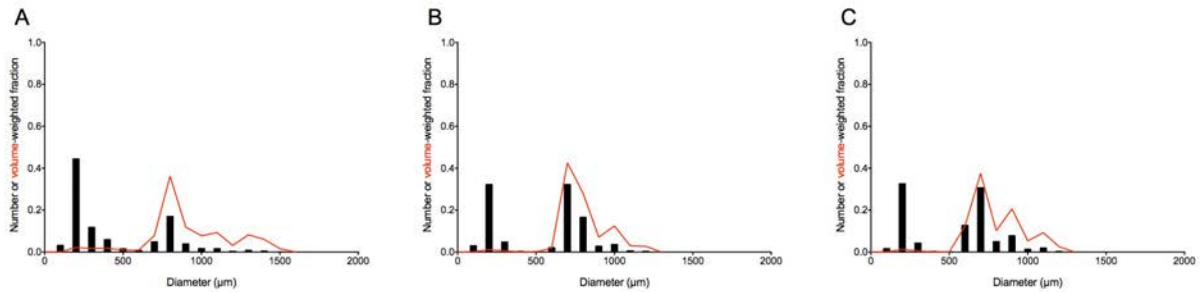


Figure B.14. Particle size distributions obtained with device 3-3.

Histograms of the number-weighted (black bars on left Y-axis) and volume-weighted alginate bead size distributions (red line on the right Y-axis) at outer flow rates of (A) 30 mL/min, (B) 40 mL/min and (C) 50 mL/min.

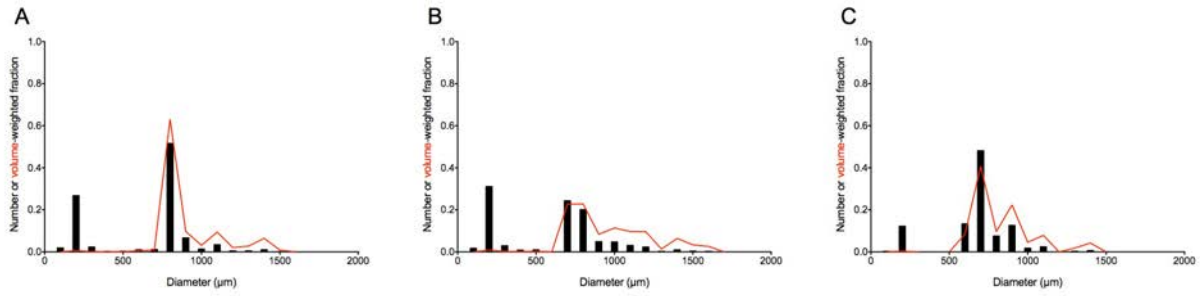


Figure B.15. Particle size distributions obtained with device 4-1.

Histograms of the number-weighted (black bars on left Y-axis) and volume-weighted alginate bead size distributions (red line on the right Y-axis) at outer flow rates of (A) 30 mL/min, (B) 40 mL/min and (C) 50 mL/min.

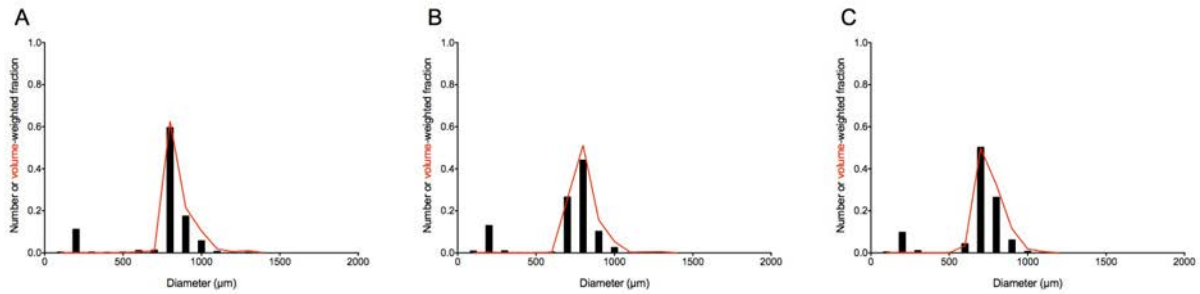


Figure B.16. Particle size distributions obtained with device 4-2.

Histograms of the number-weighted (black bars on left Y-axis) and volume-weighted alginate bead size distributions (red line on the right Y-axis) at outer flow rates of (A) 30 mL/min, (B) 40 mL/min and (C) 50 mL/min.

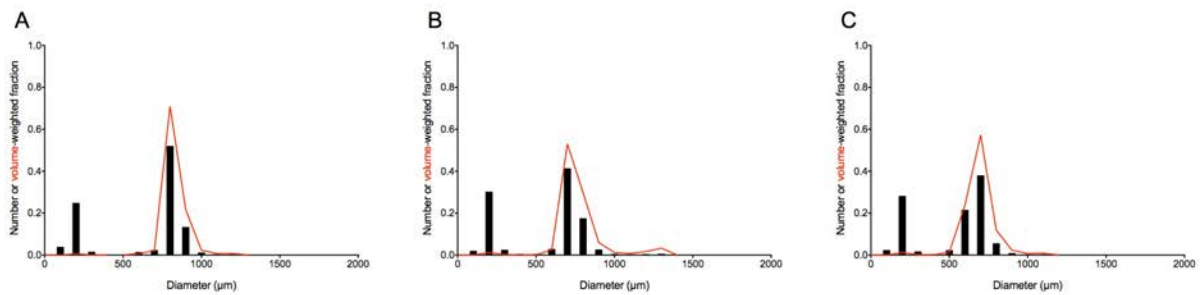


Figure B.17. Particle size distributions obtained with device 4-3.

Histograms of the number-weighted (black bars on left Y-axis) and volume-weighted alginate bead size distributions (red line on the right Y-axis) at outer flow rates of (A) 30 mL/min, (B) 40 mL/min and (C) 50 mL/min.

B.3 Scatterplots of needle alignment vs. polydispersity

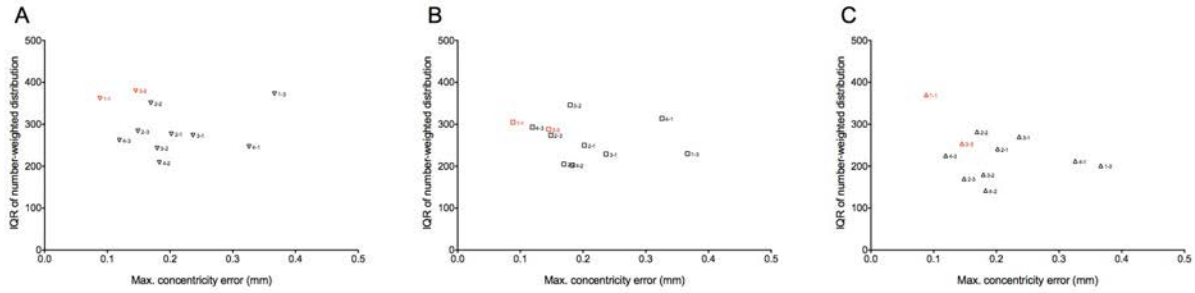


Figure B.18. Interquartile range of alginate bead size number-weighted distribution and maximum concentricity error at each flow rate.

At outer flow rate of 30 mL/min (A), r_S was -0.236 (95% CI: -0.742 to 0.44, two-tailed p-value = 0.485). At 40 mL/min (B), r_S was -0.291 (95% CI: -0.767 to 0.392, two-tailed p-value = 0.386). At 50 mL/min (C), r_S was -0.318 (95% CI: -0.779 to 0.366, two-tailed p-value = 0.341).

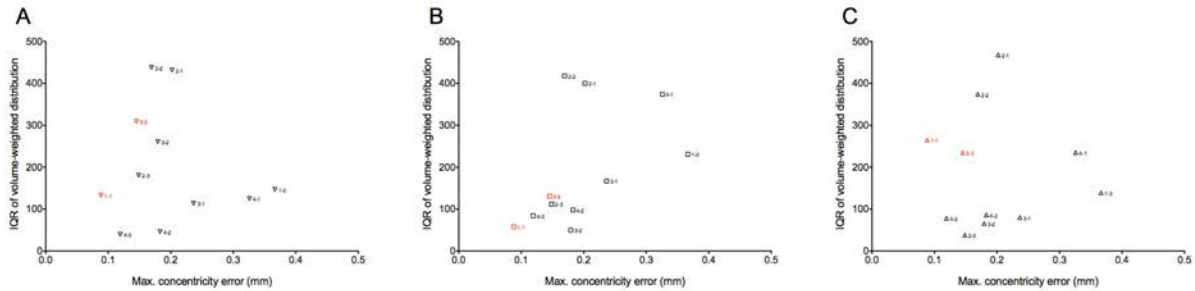


Figure B.19. Interquartile range of alginate bead size volume-weighted distribution and maximum concentricity error at each flow rate.

At outer flow rate of 30 mL/min (A), r_S was -0.036 (95% CI: -0.635 to 0.59, two-tailed p-value = 0.924). At 40 mL/min (B), r_S was 0.545 (95% CI: -0.101 to 0.868, two-tailed p-value = 0.088). At 50 mL/min (C), r_S was 0.068 (95% CI: -0.568 to 0.654, two-tailed p-value = 0.838).

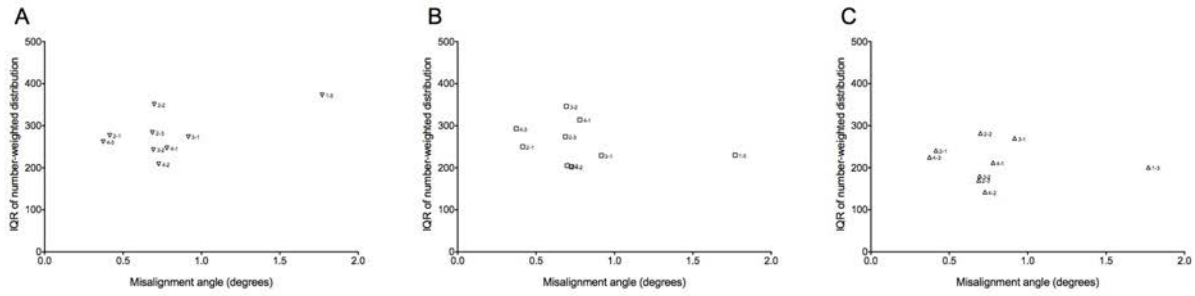


Figure B.20. Interquartile range of alginate bead size number-weighted distribution and misalignment angle at each flow rate.

At outer flow rate of 30 mL/min (A), r_s was 0.133 (two-tailed p-value = 0.743). At 40 mL/min (B), r_s was -0.367 (two-tailed p-value = 0.336). At 50 mL/min (C), r_s was -0.017 (two-tailed p-value = 0.981).

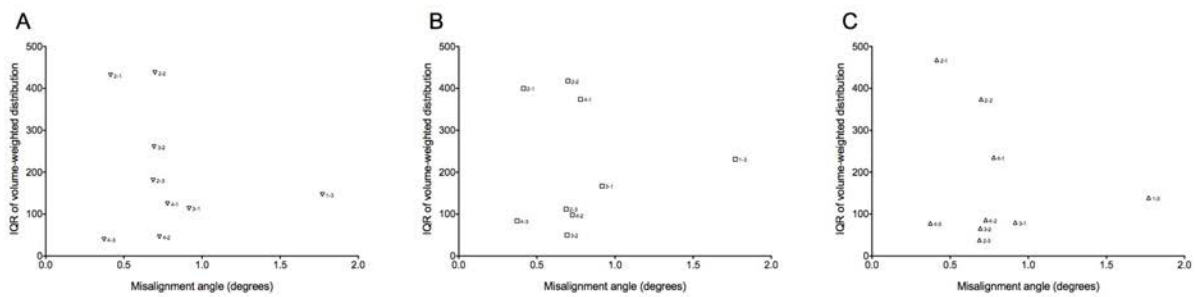


Figure B.21. Interquartile range of alginate bead size volume-weighted distribution and misalignment angle at each flow rate.

At outer flow rate of 30 mL/min (A), r_s was -0.133 (two-tailed p-value = 0.743). At 40 mL/min (B), r_s was 0.25 (two-tailed p-value = 0.521). At 50 mL/min (C), r_s was 0.2 (two-tailed p-value = 0.613).

B.4 Micrographs of NPI

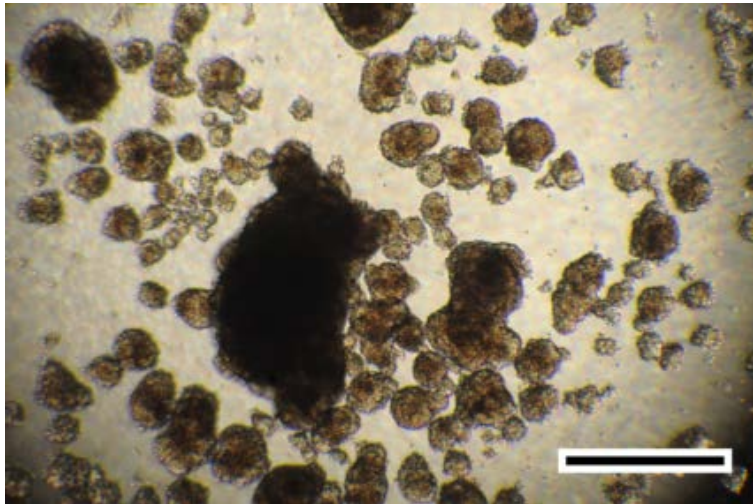


Figure B.22. NPI before manual disaggregation.

Scale bar = 500 μm .

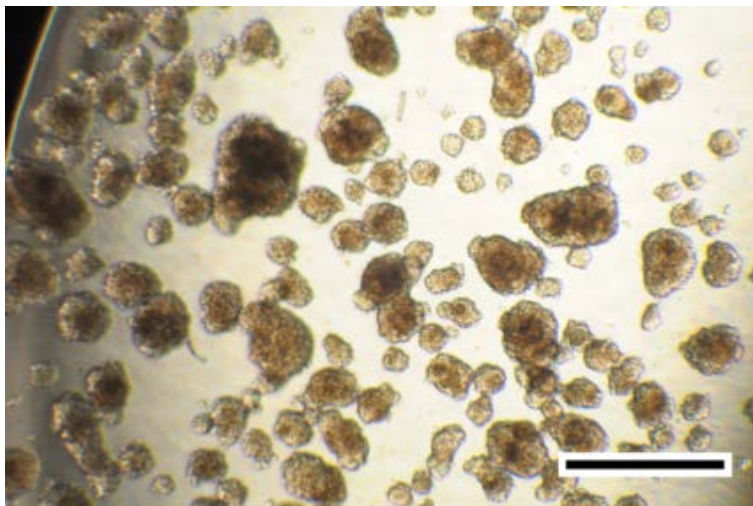


Figure B.23. NPI after manual disaggregation.

Scale bar = 500 μm .

B.5 Micrographs of alginate particles

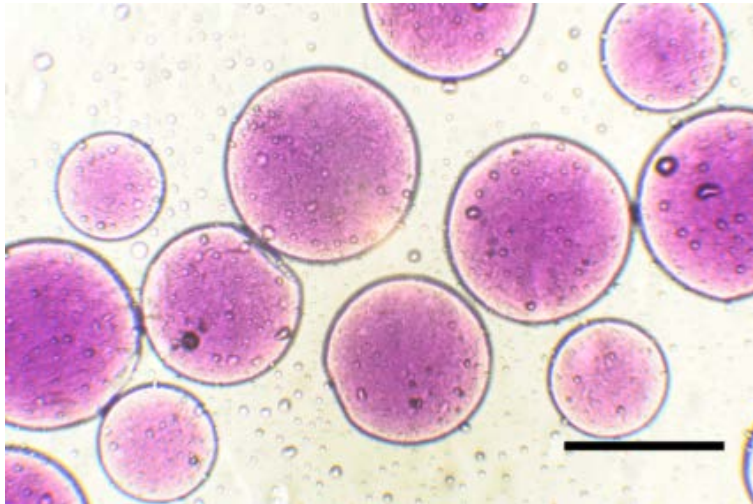


Figure B.24. Empty alginate beads.

Produced without surfactants at outer flow rate of 30 mL/min. Scale bar = 500 μm

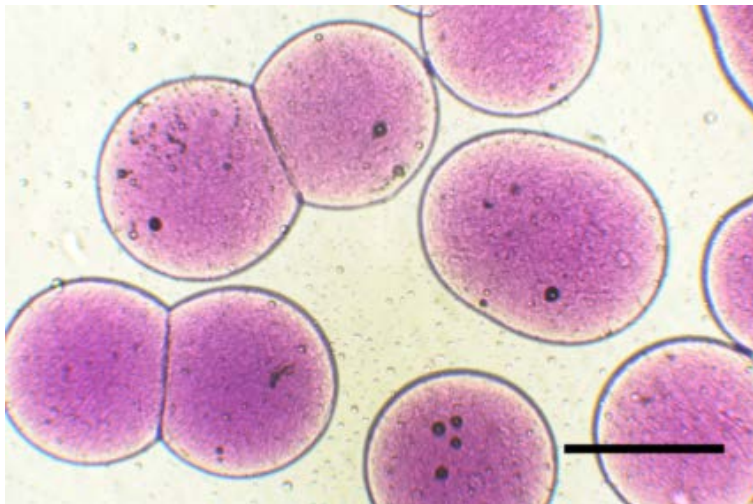


Figure B.25. Tween 20 alginate beads

Empty alginate beads produced with 1% w/v Tween 20 added to the oil phase at outer flow rate of 30 mL/min. Scale bar = 500 μm .

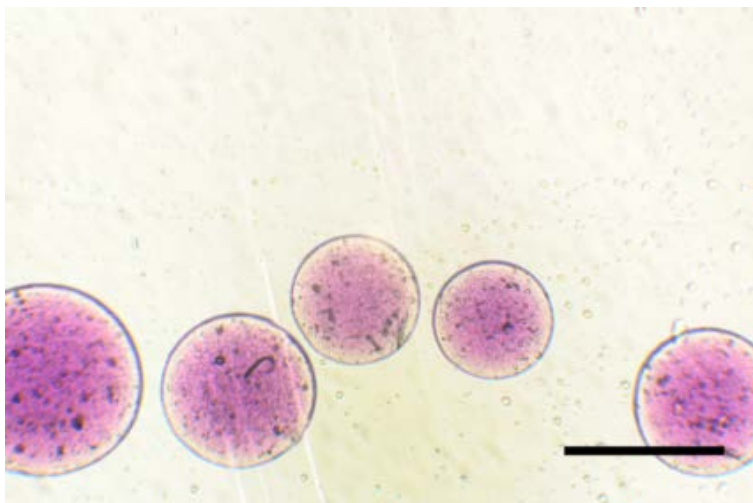


Figure B.26. Span 80 alginate beads.

Empty alginate beads produced with 1% w/v Span 80 added to the oil phase at outer flow rate of 30 mL/min. Scale bar = 500 μm .



Figure B.27. Alginate capsules containing NPI produced at outer flow rate of 30 mL/min.

Scale bar = 500 μm .



Figure B.28. Alginate beads containing NPI produced at outer flow rate of 40 mL/min.

Scale bar = 500 μm .

B.6 Size distribution of alginate capsules generated through emulsification-internal gelation

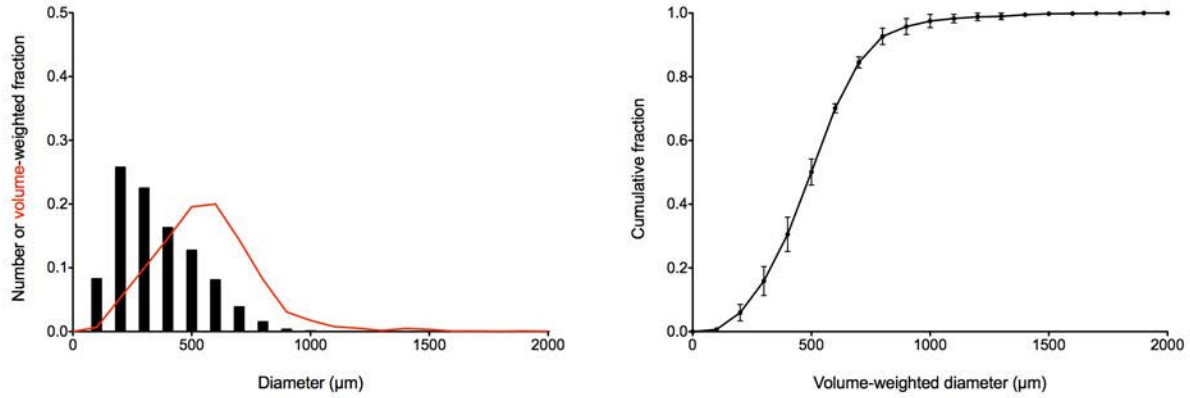


Figure B.29. Alginate capsules containing NPI produced via emulsification-internal gelation.

(A) Histogram of pooled number-weighted and volume-weighted alginate capsule size distributions. (B) Cumulative volume-weighted alginate capsule size distributions. $D[2,0]$ was $401 \pm 43 \mu\text{m}$, $D[4,3]$ was $611 \pm 7 \mu\text{m}$, and the coefficient of variation of the volume-weighted distribution was $34.7 \pm 11.5\%$.

B.7 Additional CT scans with magnetic particles as contrast agents.



Figure B.30. Side projections of scans using iron oxide particles as contrast agents.

Examples of contrast agents that precipitated, *i.e.*, an unstable dispersion (left), and that did not precipitate, *i.e.*, a colloidal dispersion (right) while imaging.

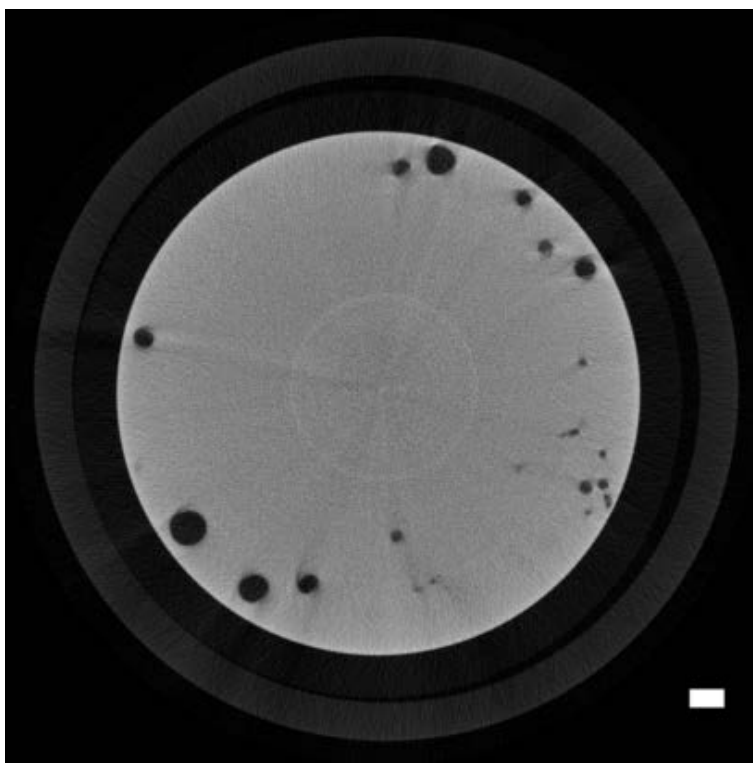


Figure B.31. CT scan using colloidal dispersions of iron oxide nanoparticles as contrast agent.

Alginate capsules containing NPI were re-suspended in buffer containing $\sim 0.25\%$ w/v 30 nm iron nanoparticles, transferred to a 1.5-cm tube, and scanned using a 74-mm sample holder at $10\ \mu\text{m}/\text{voxel}$ resolution. CT parameters: 45 keV peak voltage, 200 μA current, 600 ms integration time, 500 projections.

Appendix C - Supplementary tables

C.1 Summary of results for orthogonal Friedman tests

All tables report mean, median and range of the Friedman Chi-squared and corresponding p-values obtained after running Friedman tests across 27 complete case data sets.

Table C.1 Friedman ranked sum tests for D[2,0].

	Chi-squared	Degrees of freedom	p-value
Design	8.304	3	0.041
	8.200 (7.000 – 9.000)		0.042 (0.029 – 0.072)
Flow	3.167	2	0.281
	3.000 (0.750 – 9.000)		0.223 (0.011 – 0.687)

Table C.2. Friedman ranked sum tests for D[4,3].

	Chi-squared	Degrees of freedom	p-value
Design	4.837	3	0.224
	5.800 (1.000 – 7.000)		0.122 (0.072 – 0.801)
Flow	9.250	2	0.012
	9.000 (7.750 – 12.250)		0.011 (0.002 – 0.021)

Table C.3. Friedman ranked sum tests for IQR_{2,0}.

	Chi-squared	Degrees of freedom	p-value
Design	5.326	3	0.206
	5.000 (1.800 – 8.200)		0.172 (0.042 – 0.615)
Flow	6.111	2	0.054
	6.250 (4.000 – 7.750)		0.044 (0.021 – 0.135)

Table C.4. Friedman ranked sum tests for IQR_{4,3}.

	Chi-squared	Degrees of freedom	p-value
Design	6.200	3	0.108
	5.800		0.122
	(5.400 – 8.200)		(0.042 – 0.145)
Flow	0.667	2	0.748
	0.250		0.882
	(0.250 – 1.750)		(0.417 – 0.882)

Table C.5. Friedman ranked sum tests for frequency.

	Chi-squared	Degrees of freedom	p-value
Design	6.452	3	0.121
	6.600		0.086
	(2.600 – 9.000)		(0.029 – 0.457)
Flow	3.167	2	0.281
	3.000		0.223
	(0.750 – 9.000)		(0.011 – 0.687)

C.2 Summary of ANOVA results for simple ranked transform data

All tables report p-values for Type II Wald F tests with Kenward-Roger degrees of freedom.

Table C.6. Analysis of deviance for rank transformed D[2,0].

	F value	Degrees of freedom	Residual degrees of freedom	p-value
Design	3.742	3	7	0.068
Flow	0.587	2	14	0.569
Interaction	0.397	6	14	0.868

Table C.7. Analysis of deviance for rank transformed D[4,3].

	F value	Degrees of freedom	Residual degrees of freedom	p-value
Design	0.2574	3	7	0.854
Flow	10.999	2	14	0.001
Interaction	0.551	6	14	0.761

Table C.8. Analysis of deviance for rank transformed IQR_{2,0}.

	F value	Degrees of freedom	Residual degrees of freedom	p-value
Design	1.110	3	7	0.407
Flow	4.339	2	14	0.034
Interaction	0.800	6	14	0.586

Table C.9. Analysis of deviance for rank transformed IQR_{4,3}.

	F value	Degrees of freedom	Residual degrees of freedom	p-value
Design	0.257	3	7	0.854
Flow	10.999	2	14	0.001
Interaction	0.551	6	14	0.761

Table C.10. Analysis of deviance for rank transformed frequency.

	F value	Degrees of freedom	Residual degrees of freedom	p-value
Design	1.438	3	7	0.311
Flow	1.786	2	14	0.204
Interaction	0.186	6	14	0.976

C.3 Summary of ANOVA and post hoc results for ART data

The following tables report p-values for Type II Wald F tests with Kenward-Roger degrees of freedom.

Table C.11. Analysis of deviance for aligned rank transformed D[2,0].

	F value	Degrees of freedom	Residual degrees of freedom	p-value
Design	4.052	3	7	0.058
Flow	0.942	2	14	0.413
Interaction	0.467	6	14	0.822

Table C.12. Analysis of deviance for aligned rank transformed D[4,3].

	F value	Degrees of freedom	Residual degrees of freedom	p-value
Design	0.317	3	7	0.813
Flow	9.553	2	14	0.002
Interaction	0.552	6	14	0.761

Table C.13. Analysis of deviance for aligned rank transformed IQR_{2,0}.

	F value	Degrees of freedom	Residual degrees of freedom	p-value
Design	1.654	3	7	0.262
Flow	3.832	2	14	0.047
Interaction	0.922	6	14	0.508

Table C.14. Analysis of deviance for aligned rank transformed IQR_{4,3}.

	F value	Degrees of freedom	Residual degrees of freedom	p-value
Design	1.051	3	7	0.428
Flow	0.079	2	14	0.925
Interaction	1.652	6	14	0.205

Table C.15. Analysis of deviance for aligned rank transformed frequency.

	F value	Degrees of freedom	Residual degrees of freedom	p-value
Design	1.215	3	7	0.373
Flow	1.698	2	14	0.219
Interaction	0.058	6	14	0.999

The following tables report averaged results over the levels of design from Tukey range tests for a family of 3 means using a confidence level of 0.95.

Table C.16. Contrasts resulting from Tukey’s honest significance difference test on ART D[4,3].

Contrast	Estimate	Standard error	Degrees of freedom	t ratio	p-value
30 – 40	8.833	2.975	14	2.968	0.026
30 – 50	12.542	2.975	14	4.214	0.002
40 – 50	3.708	2.975	14	1.246	0.447

Table C.17. Contrasts resulting from Tukey’s honest significance difference test on ART IQR_{2,0}.

Contrast	Estimate	Standard error	Degrees of freedom	t ratio	p-value
30 – 40	5.042	4.216	14	1.196	0.475
30 – 50	11.250	4.216	14	2.668	0.046
40 – 50	6.208	4.216	14	1.473	0.333

The following table reports averaged results over the levels of flow from Tukey range test for a family of 4 means using a confidence level of 0.95.

Table C.18. Contrasts resulting from Tukey’s honest significance difference test on ART D[2,0].

Contrast	Estimate	Standard error	Degrees of freedom	t ratio	p-value
1 – 2	-8.222	5.892	7	-1.395	0.539
1 – 3	-7.556	5.892	7	-1.282	0.601
1 – 4	-19.667	5.892	7	-3.338	0.048
2 – 3	0.667	5.892	7	0.126	0.999
2 – 4	-11.444	5.892	7	-2.171	0.221
3 – 4	-12.111	5.892	7	-2.298	0.188